

https://dspace.org/

Heteroatom carbon spheres incorporated with Titania for photocatalytic degradation of organic pollutants

Mhlana, Yongezile

2021

https://hdl.handle.net/10539/33165

Downloaded from a DSpace repository. https://dspace.org/

Heteroatom Carbon Spheres incorporated with Titania for photocatalytic degradation of organic pollutants

By

Yongezile Mhlana

Student number: 670607

A dissertation submitted to the Faculty of Science, University of the Witwatersrand, Johannesburg, in fulfilment for the degree of Master of Science in Chemistry.

Supervisor: Dr Zikhona N. Tetana

Co-Supervisor: Dr Cebisa E. Linganiso

Co-Supervisor: Dr John Moma

University of the Witwatersrand, Johannesburg. April 2021

DECLARATION

I declare that this Dissertation is my own, unaided work. It is being submitted for the Degree of Master of Science at the University of the Witwatersrand, Johannesburg. It has not been submitted before for any degree or examination at any other University. Yongezile Mhlana on this 23 day of April 2021



WITS
UNIVERSITY



(Signature of candidate)

On this 23rd day of April 2021

DEDICATION

This dissertation is dedicated to my family, especially my grandmother, Nomazentu Mhlana. Thank you, Mama, for all the encouragements, prayers, and words of wisdom throughout this journey. To the Creator of the universe who is my Lord and savior Jesus Christ, who kept on providing for me, giving me strength, and always reminded me that His plans are always to prosper me not to harm me. Finally, to my late mother, Nomlindo Mhlana.

"Many are the plans in a person's heart, but it is the Lord's purpose that prevails." Proverbs 19:21

ACKNOWLEDGEMENT

This dissertation began as a big, messy thing that required more than my understanding to comprehend it, as a result I would like to express my gratitude to the following people who helped to shape it out to something better:

- I would like to express my gratitude to my supervisor Dr. Zikhona Tetana for the guidance, patience, and support throughout this project.
- I would like to thank my co-supervisors Dr. Cebisa Linganiso, and Dr. John Moma for their valued contribution in this project. Your guidance and support did not go unnoticed.
- To Victor Mashindi. thank you for your support from the beginning of this journey. I am thankful for your constant motivation and the holistic assistance you offered in this work.
- A special thank you to Dr. Rudolph Erasmus for his assistance with laser Raman spectroscopy measurements, and Petra Dinham for assisting me with SEM images. I would also like to thank the CSIR NMSA for XPS analysis.
- I would like to thank MMU unit for their assistance in using the instruments.
- CATMAT group for constructive comments and discussions that were so fruitful. The moments that were shared during this time were instrumental and will never be forgotten.
- To Alice Magubane, Pumza Mente and William Mokone for showing me around the lab and for always availing yourselves to be of assistance. It has been an incredible journey.
- The DST-NRF Centre of Excellence in Strong Materials (CoE-SM) for funding.
- To all my friends, for putting up with me during the master's process especially during the writing process. You all were so supportive and understanding.

- I would like to thank my uncle Nkosiphendule Mhlana, my father Sipho Magatyana and my younger brother Mzamo Mhlana and all my siblings. Thank you for your words of encouragement and support throughout this journey.
- Last but not least to my pillar of strength, my Lord and Savior Jesus Christ. Thank you for making me believe in my dream even when the journey was unbearable, in those moments you provided me with strength and encouraged me to always lean on you. Your sufficient grace was always with me.

ABSTRACT

Continuous efforts to produce catalysts that are environmentally friendly, low-cost, and less toxic have been investigated for the treatment of organic pollutants in wastewater. In this research, an onion raw material that is environmentally friendly, abundant and is a green carbon precursor was used to synthesize carbon material. The onion material consists of heteroatoms such as nitrogen, sulfur, oxygen, hydrogen, and carbon elements. Here, we demonstrated an onion material synthesized by the hydrothermal process followed by the CVD method to produce nitrogen, sulfur co-doped carbon spheres (NSCS). The resultant product was subjected to various synthesis temperatures (850, 900, and 950 ℃), in order to understand the effect of synthesis temperature on the NSCS material. Natural-based carbon precursors require activating agents, in this study potassium hydroxide (KOH) and zinc chloride ($ZnCl_2$) were used as activating agents to produce spherical carbon products. The NSCS material was later denoted as NSCS without activation, NSCS2 (NSCS2 KOH; NSCS2 $ZnCl_2$), and NSCS3 (NSCS3 KOH; NSCS3 $ZnCl_2$) depending on the mass ratio of activating agent used.

The presence of heteroatoms in the synthesized NSCS material was confirmed by the CHNS elemental analysis. FTIR and XPS analysis confirmed the presence of covalent bonding between carbon and nitrogen and sulfur. Formation of covalent bonding such as C=C, C-S, and C=N was observed. The morphology, size, and structural features of the carbon spheres were studied using TEM, SEM, and laser Raman spectroscopy. The PXRD of the produced NSCS was found to be graphitic with a low graphitization degree.

TiO_2 nanoparticles were produced by the sol-gel method followed by the CVD method annealed at 450 ℃ with a crystallite size of 12 nm observed from PXRD. The resultant TiO_2 showed a high surface area of 51.2 m^2/g. The catalyst (TiO_2_NSCS) was obtained following the same procedure as that of the formation of TiO_2 nanoparticles. Successful incorporation of the NSCS to TiO_2 was confirmed by XPS with different configurations of the material being observed. The results obtained from BET showed a high surface area of NSCS material and in turn when they were used as support material for TiO_2, a high surface area of the composite was observed. The catalyst was tested by photodegradation of Rhodamine B dye, to evaluate its activity and stability. High-pressure liquid chromatography coupled with mass spectroscopy (HPLC-MS) technique was used

to confirm the degradation of the RhB dye compound. Additionally, the breakdown of the complex RhB dye structure was reported. It was observed that a lower molecular mass was plausible when the composite was used as an alternative to using TiO_2 alone.

PRESENTATIONS

“Heteroatom Carbon Spheres incorporated with Titania for photocatalytic degradation of organic pollutants” (**Poster presentation)**, Faculty of Science. Wits Cross-Faculty Postgraduate Symposium (September 2019).

“Heteroatom Carbon Spheres incorporated with Titania for photocatalytic degradation of organic pollutants” (**Poster presentation)**, Catalysis society of South Africa (CATSA) annual conference (Capetown), November 2019.

“Heteroatom Carbon Spheres incorporated with Titania for photocatalytic degradation of organic pollutants” (**Poster presentation)**, Faculty of Science. Wits Cross-Faculty Postgraduate Symposium (October 2020).

TABLE OF CONTENTS

DECLARATION……i

DEDICATION……ii

ACKNOWLEDGEMENT……iii

ABSTRACT……v-vi

PRESENTATIONS……vii

TABLE OF CONTENTS……viii-xii

LIST OF FIGURES……xii-xv

LIST OF TABLES……xv

LIST OF ABBREVIATIONS……xv-xvi

LIST OF CHEMICAL FORMULAS……xvii

CHAPTER 1: INTRODUCTION ……1

1. 1 Background ……1

1.2 Problem statement ……2

1.3 Project motivation ……2

1.4 Aims……3

1.5 Objectives of the study ……3

1.6 Dissertation outline……4

1.7 References ……6

CHAPTER 2: LITERATURE REVIEW……8

2.1 Background……8

2.2 Classification of dyes……10

2.3 Rhodamine B……11

2.4 Photocatalysis……12

2.4.1 Titanium dioxide……13

2.4.1.1 Polymorphs of TiO_2……15

2.4.1.2 Synthesis of TiO_2 particles……16

2.4.1.2.1 The chemical precipitation method……17

2.4.1.2.2 The chemical vapor deposition (CVD) method……17
2.4.1.2.3 The hydrothermal method……17
2.4.1.2.4 The sol-gel method……18
2.4.2 Drawbacks of TiO_2 as a catalyst……18
2.4.3 Strategies to improve photocatalytic performance of TiO_2……19
2.4.3.1 Doping of TiO_2……19
2.4.3.2 Morphological control of TiO_2……21
2.4.3.3 Metal oxides with TiO_2……21
2.4.3.4 Supported TiO_2 with carbon allotropes to enhance photocatalytic activity……22
2.5 Effect of operational parameters on degradation efficiency……24
2.5.1 Catalyst loading……24
2.5.2 Dye concentration……25
2.5.3 The pH of the solution……25
2.6 Carbon nanomaterials……26
2.6.1 Carbon spheres……27
2.6.1.1 Synthesis of carbon spheres……27
2.6.1.2 Strategies for improving chemical and physical properties of carbon spheres……29
2.6.1.2.1 Heteroatom dopant for CSs……29
2.6.1.2.2 Functionalisation of CSs……32
2.7 Green methods for production of intrinsically doped Carbon Spheres……33
2.7.1 Activating agents……35
2.8 References……36
CHAPTER 3: CHARACTERIZATION TECHNIQUES……49
3.1 Introduction……49
3.1.1 Transmission electron microscopy (TEM)……49
3.1.2 Scanning electron microscopy (SEM)……49
3.1.3 Elemental analysis (CHNS)……50
3.1.4 Powder X-ray diffraction (PXRD)……50
3.1.5 Laser Raman spectroscopy……51

3.1.6 Fourier transmission infrared (FTIR) spectroscopy……51

3.1.7 X-ray photoelectron spectroscopy (XPS)……51

3.1.8 Thermogravimetric analysis (TGA)……52

3.1.9 Brunauer Emmet and Teller (BET)……52

3.1.10 UV-Vis spectroscopy……52

3.2 Photocatalytic degradation……53

3.2.1 High performance liquid chromatography (HPLC)……54

3.2.2 Mass spectrometry (MS)……54

3.3 References……56

CHAPTER 4: EFFECTS OF ACTIVATING AGENT AND ANNEALING TEMPERATURE ON THE PREPARATION OF THE NITROGEN AND SULFUR CO-DOPED CARBON SPHERES (NSCS) USING AN ONION ……58

4.1 Introduction……58

4.2 Experimental……61

4.2.1 Effect of activating agents on the growth of NSCS……61

4.3.1 Effect of the annealing temperature and functionalization on the properties of the NSCS……62

4.3 Results and discussion……64

4.3.1 Effect of activating agents on the growth of the NSCS……64

4.3.1.1 TEM analysis of the NSCS……64

4.3.1.2 CHNS elemental analysis of the NSCS……66

4.3.1.3 PXRD analysis……67

4.3.1.4 BET analysis……68

4.3.1.5 FTIR analysis……69

4.3.1.6 Laser Raman spectroscopy……70

4.3.2 Effect of the annealing temperature and functionalization on the properties of the NSCS……71

4.3.2.1 TEM analysis of the annealed NSCS……71

4.3.2.2 SEM analysis of the annealed NSCS……73

4.3.2.3 PXRD analysis of the annealed NSCS……74

4.3.2.4 Laser Raman spectroscopy analysis of the annealed NSCS……75

4.3.2.5 BET analysis of the annealed NSCS……77
4.3.2.6 FTIR analysis of the annealed NSCS……77
4.3.2.7 XPS analysis of the annealed NSCS……79
4.3.2.8 TGA analysis of the annealed NSCS……82
4.4 Conclusion……83
4.5 References……85
CHAPTER 5: SYNTHESIS AND CHARACTERIZATION OF TIO_2 NANOPARTICLES AND TIO_2 INCORPORATED WITH NSCS PREPARED BY THE SOL-GEL METHOD FOR PHOTODEGRADATION OF RHODAMINE B……88
5.1 Introduction……88
5.2 Experimental……89
5.2.1 Sol-gel method for preparation of TiO_2, and TiO_2-NSCS catalysts……89
5.2.2 Photodegradation measurements……90
5.3 Results and discussion……91
5.3.1 Materials characterization……91
5.3.1.1 PXRD analysis……91
5.3.1.2 TEM analysis of TiO_2, and TiO_2_NSCS ……92
5.3.1.3 SEM analysis of TiO_2, and TiO_2_NSCS ……94
5.3.1.4 FTIR spectroscopy……95
5.3.1.5 BET analysis……96
5.3.1.6 Laser Raman spectroscopy analysis……98
5.3.1.7 XPS elemental analysis……99
5.3.1.8 TGA analysis……100
5.3.2 Photodegradation studies……101
5.3.2.1 Optical studies: UV-visible Spectroscopy ……105
5.3.2.2 Optimization of photocatalytic conditions……108
5.3.2.2 Catalyst loading effect……108
5.3.2.2 Effect of dye concentration……109
5.3.2.2 Effect of pH……110
5.3.2.2 High performance liquid chromatography-Mass spectroscopy (HPLC-MS)……112

5.5 Conclusion……118
5.6 References……119
CHAPTER 6: CONCLUSSIONS AND RECOMMENDATIONS……122
6.1 CONCLUSSIONS……122
6.2 RECOMMENDATIONS……123

LIST OF FIGURES

Figure 2.1: Flow diagram of a) coloured fabric, b) discharge of coloured wastewater to the water streams c) clear water after few hours of coloured wastewater [6]……...9

Figure 2.2: Line drawing representation of the molecular structure Rhodamine B [14]……12

Figure. 2.3: Proposed mechanism for photocatalytic reaction, with schematic diagram showing electron hole pairing during heterogeneous photocatalysis [27]…….....15

Figure 2.4: Representations of the unit cells of: (a) Anatase (b) Rutile (c) Brookite [33-35]….16

Figure 2.5: Illustration of carbon material support- TiO_2 photocatalysis mechanism [77]…….24

Figure 2.6: TEM images of a) carbon spheres prepared by Kaolin at 200 sccm flow rate and b) treated by HF (48%) solution [88]……28

Figure 2.7: Incorporation of nitrogen onto the carbon sphere matrix [113]……30

Figure 2.8: Functionalization of nitrogen, sulfur co-doped carbon spheres [90]…..……..32

Figure 2.9: Illustration of oatmeal with its nutrients [113]……...……...34

Figure 3.1: Schematic representation of the Newport Illuminator Solar Simulator Oriel Instruments WX00048 [1]…….....53

Figure 4.1: Illustration of elements found within the onion material [4]…….61

Figure 4.2: Schematic diagram showing synthesis of NSCS nanoparticles using onion material [4]……...62

Figure 4.3: Experimental set-up of functionalization of NSCSs nanoparticles using HNO_3 and H_2SO_4…….....63

Figure 4.4: TEM images of (a) NSCS without activation, (b) NSCS2 with KOH, (c) NSCS2 with $ZnCl_2$, (d) NSCS3 with KOH, and (e) NSCS3 with $ZnCl_2$ @ 850 ℃ ...……65

Figure 4.5: PXRD patterns of NSCS material showing the effect of an activation agent…….67

Figure 4.6: FTIR spectra of NSCS without activation, NSCS2 with KOH, and NSCS2 with $ZnCl_2$…….....69

Figure 4.7: Laser Raman spectra of NSCS without activation, NSCS2 with KOH, and NSCS2 with $ZnCl_2$……..70

Figure 4.8: TEM images of the as-prepared: (a) NSCS2 @850 ℃, (b) NSCS2 @900 ℃ and (c) NSCS2 @950 ℃ with corresponding histograms……...72

Figure 4.9: SEM images of the as-prepared: (a) 1:2 $ZnCl_2$ @850 ℃, (b) 1:2 $ZnCl_2$ @900 ℃ and (c) 1:2 $ZnCl_2$ @950 ℃……73

Figure 4.10: PXRD patterns of NSCS at different synthesis temperatures……74

Figure 4.11: Laser Raman spectra of NSCS2 $ZnCl_2$ annealed at different temperatures…..……..76

Figure 4.12: FTIR spectra of as synthesized NSCS2 at a) 850 b) 900 and c) 950 ℃. ……..78

Figure 4.13: XPS spectra of as-synthesized NSCS, NSCS2 at 850, 900, and 950 ℃……79

Figure 4.14: High resolution XPS spectra of (a) C 1s, (b) O 1s, (c) N 1s, and (d) S 2p of NSCS…82

Figure 4.15: (a) TGA and (b) DTG thermograms of NSCS annealed at 850, 900, and 950 ℃….83

Figure 5.1: Experimental procedure of preparation of TiO_2 nanoparticles and the composite…90

Figure 5.2: PXRD patterns of the synthesized TiO_2 and the NSCS_TiO_2 composites……92

Figure 5.3: TEM micrograph of: (a) TiO_2, (b) NSCS_ TiO_2 @ 850 and (c) NSCS_ TiO_2 @ 900 ℃ composites…….93

Figure 5.4: SEM of the synthesized (a) TiO_2, (b) NSCS_ TiO_2 @ 850, and (c) NSCS_ TiO_2 @ 900 ℃ composites……..94

Figure 5.5: FTIR spectra of (a) TiO_2, (b) NSCS2_TiO_2 @ 850 ℃, and NSCS3_TiO_2 @ 900 ℃ ...……....95

Figure 5.6: Interpretation of the FTIR spectra of the carbon material [24]……..96

Figure 5.7: N_2 adsorption-desorption at 77 K of (a) TiO_2, (b) NSCS2_TiO_2 @850, and (c) NSCS3_TiO_2 @900 ℃……...97

Figure 5.8: Raman spectra of TiO_2 and NSCS_TiO_2 composites…….98

Figure 5.9: XPS of NSCS_TiO_2 composites at different temperatures and that of Ti 2p…….100

Figure 5.10: TGA of NSCS_TiO_2 composites at different temperatures……..……..101

Figure 5.11: Photodegradation of NSCS synthesized at 850 ℃ in both acidic and basic media...102

Figure 5.12: Variation of dye RhB concentrations as constant catalyst loading.....103

Figure 5.13: RhB degradation using NSCS_TiO_2 photocatalyst prepared by sol-gel method in 15 minutes intervals…….....104

Figure 5.14: UV-visible of TiO_2 and NSCS3_TiO_2 @ 900 ℃……105

Figure 5.15: Comparison of the photocatalytic activities of NSCS_TiO_2 and bare TiO_2 degradation of RhB……..……107

Figure 5.16: Plot of $\ln(C_0/C_T)$ versus irradiation time of NSCS_TiO_2 with bare TiO_2……..108

Figure 5.17: The effect of mass loading of the photocatalyst at 10 ppm dye concentration……109

Figure 5.18: The effect of initial RhB concentration at constant pH 7 and catalyst loading of 10 mg…….…...110

Figure 5.19: Effect of pH on the reaction mixture of degradation of RhB in 15 minutes interval…….112

Figure 5.20: a) HPLC-MS of (a and c) NSCS_TiO_2 and bare TiO_2 before exposure to visible light and (b and d) NSCS_TiO_2 and bare TiO_2 after exposure to visible light for degradation of RhB……..115

Figure 5.21: Mechanism of the photocatalytic mineralization of RhB [29]……...116

Figure 5.22: Mechanism of the photocatalytic mineralization of RhB [12]……117

LIST OF TABLES

Table 2.1 Parameters of TiO_2 polymorphs [33-35]……..16

Table 4.1: CHNS elemental analysis comparison of NSCS without activation and NSCS activated with $ZnCl_2$ at different mass ratios……..……...66

Table 4.2: BET results of NSCS at different activation ratios……...68

Table 4.3: Laser Raman D and G, I_D/I_G ratio and A_D/A_G of NSCS……...71

Table 4.4: Laser Raman D and G, I_D/I_G ratio and A_D/A_G of NSCS……...76

Table 4.5: Comparison of the NSCS annealed at different temperatures…….77

Table 4.6: XPS elemental analysis of NSCS material synthesized at various materials……...79

Table 5.1: Average crystallite size of TiO_2 and NSCS_TiO_2 composites…….92

Table 5.2: BET surface area of TiO_2 and NSCS_TiO_2 composites……...97

Table 5.3: XPS elemental analysis and quantification of NSCS_TiO_2……..…...99

Table 5.4 Percentage conversion of the NSCSs_TiO_2 composites…….…….104

LIST OF ABBREVIATIONS

AOPs – Advanced Oxidation Processes

a.u. – Arbitrary Units

BET - Brunauer-Emmett-Teller

CB – Conduction band

CSs – Carbon spheres

CNTs – Carbon nanotubes

CVD – Chemical vapor deposition

e- - Electron

E_g – Band gap energy

eq – Equation

eV – electron volt

FTIR – Fourier transform infrared spectroscopy

h+ - hole

HPLC – High performance liquid chromatography

hv – Energy of light

min – minutes

MS – Mass Spectrometry

m/z – Mass-to-charge ratio

N-CSs – Nitrogen-doped carbon spheres

nm – Nanometer

NSCS – Nitrogen, Sulfur doped Carbon Spheres

NSCS2 – 1NSCS: $2ZnCl_2$

NSCS3 – 1NSCS: $3ZnCl_2$

$OH^{\cdot}$ – Hydroxyl radicals

OH^- - Hydroxyl anions

$O_2^{\cdot -}$ - Superoxide radical anions

ppm – Parts per million

PXRD – Powder X-ray diffraction

RhB – Rhodamine B

SEM – Scanning electron microscopy

TEM – Transmission electron microscopy

TGA- Thermogravimetric analysis

UV-VIS – Ultraviolet Visible Spectroscopy

VB – Valence band

WHO – World Health Organization

hGO – Reduced graphene oxide

LIST OF CHEMICAL FORMULAS

B - Boron

CO_2 – Carbon dioxide

HNO_3 – nitric acid

H_2O – water

H_2 – hydrogen gas

H_2SO_4 – sulfuric acid

N_2 – Nitrogen gas

N - Nitrogen

O – Oxygen

P - Phosphorus

S – Sulfur

SiO_2 – Silica

TiO_2 – Titanium dioxide

ZnO – Zinc Oxide

CHAPTER 1: INTRODUCTION

1.1 Brief background

Industrialization keeps growing year after year and as much as this is advantageous in terms of the economy; the environmental pollution, on the other hand, continues to increase rapidly. For instance, the textile industry which mainly specializes in the production of fabrics of various colors has largely grown due to the high demand for these fabrics as the population increases [1]. The main pressing issue is the disposal and treatment of the wastewater after the production of the fabrics. Biological, physical, and chemical techniques have been used, however, due to the complexity of the resultant secondary sludge these techniques are currently used. The presence of the secondary sludge may be hazardous to the environment, also, it has been reported to be expensive to treat [1,2].

Activated carbon adsorption, chemical oxidation, and sonolysis are some of the techniques that are environmentally friendly, economically viable, and sustainable and have been investigated for environmental applications [1,2]. Advanced oxidation processes (AOPs) techniques more specifically heterogeneous photocatalysis, which introduced the use of solar energy technology with semiconductor catalysts for the treatment of wastewater pollution has received much interest [1]. Semiconductor photocatalysts such as zinc oxide (ZnO), silica (SiO_2) and titanium dioxide (TiO_2, known as titania), etc. have been employed for application in the photocatalytic degradation of dyes [2]. Due to its non-toxicity, relatively inexpensiveness, and high chemical stability, TiO_2 is the preferred catalyst for application in heterogeneous photocatalysis [2,3]. Despite the above-mentioned advantages, TiO_2 has shortcomings such as a wide bandgap (3.2 eV for anatase phase), photoresponsive under the UV region that constitutes 5% of the solar spectrum, and fast electron-hole pair recombination [4]. As a result, ongoing research on different ways to improve the photoresponse of TiO_2 under solar simulator remains in development. Modifications using metals and non-metals have been studied [5]. However, due to toxicity and difficulty to remove metals, much focus has been on non-metal dopants such as carbon allotropes, nitrogen, and sulfur [5,6].

Carbon spheres (CSs) are a family of the fullerene group that was discovered later than most types of carbon morphologies [7]. Carbon spheres possess unique chemical and physical properties [8].

As a result, much interest in heterogeneous photocatalysis has been on carbons (CNTs and CSs) for use as support for TiO_2 [7, 8]. However, lately, it has been found that doping of carbon spheres alters other properties that are of interest in photocatalytic application. Depending on the position occupied by an element in the periodic table, different applications can be improved when carbon spheres are doped with different heteroatoms. Doping carbon spheres with nitrogen for example has been bountifully investigated [7-10]. This is due to doped CSs properties such as high electrical conductivity and catalytic activity of the carbon materials that are altered when nitrogen has been used as a dopant [9]. This elevated interests in other heteroatoms such as sulfur, boron, and phosphorus as these consist of different properties [10].

1.2 Problem statement

Out of the hundred percent available natural water on earth, only 3% of the freshwater can be used for drinking [11]. This raises problems when organic and inorganic chemicals from various industries then contaminate the limited available water. The problem results due to the difficulty in removing these pollutants during wastewater treatment [11]. The World Health Organization (WHO) in the health risks in aquifer recharge using reclaimed water report published in 2003, reported that due to the increase in industrialization, the world is running low on fresh water, and this will soon result in water scarcity [12]. The essence of water scarcity has led to different studies focusing on different ways of purifying water for different use such as industrial cooling, concrete mixing, and irrigation in agriculture [13]. The global quantity of wastewater with organic and inorganic pollutants produced by chemical industries is continuously increasing worldwide and the consequences are alarming [14]. These pollutants take time to degrade in water streams, resulting in the elevation of water contamination [14]. Most dye industries have difficulties in cleaning their water contamination before disposal, which led to much interest in investigating methods for wastewater treatments from dye contamination [14].

1.3 Project motivation

Depending on the material and methods used, different types of carbon spheres can be attained with different application possibilities such as fuel cells, adsorption, lithium-ion batteries, and photocatalysis. For instance, the pyrolysis method is mostly used for the production of carbon spheres, where carbon material is exposed to high temperatures and pressure conditions relative to

time, with glucose and acetylene as some of the carbon sources. This includes the use of hydrothermal process and later the chemical vapor deposition (CVD) furnace producing desired carbon spheres [15]. The resultant carbon spheres are good support for catalysts such as TiO_2 [16]. By supporting TiO_2 on nitrogen and sulfur co-doped carbon spheres (NSCS), enhancement of response under visible region is probable.

Thus, in this project, onion which widely available and a renewal source was used as a precursor for carbon, sulfur, and nitrogen. The material was synthesized by the hydrothermal process followed by CVD at various temperatures to produce nitrogen and sulfur co-doped carbon spheres. The NSCS was activated by potassium hydroxide (KOH) and zinc chloride ($ZnCl_2$) to produce tuned carbon spheres. The resultant product was used as a support material for TiO_2, producing a catalyst that was applied in the photodegradation of Rhodamine B along with the bare TiO_2 under simulated solar light conditions [6]. Rhodamine B dye as a model organic pollutant was used to taint clean water for application of as-prepared TiO_2 supported on NSCS and the bare TiO_2. Different qualitative techniques were further used to elaborate on the observed mechanism of the catalyst with the Rhodamine B dye when exposed to light.

1.4 Project Aim

This project aimed to synthesize heteroatom doped carbon spheres using a natural carbon precursor (onion vegetable) and incorporate them into TiO_2 nanoparticles obtained in the anatase phase for application in photocatalytic studies.

1.5 Objectives

- Use natural precursor (onions) as a carbon precursor to obtaining heteroatom doped carbon spheres (NSCS). Natural precursors used in literature are used concurrently with various activating agents. This work focuses on potassium hydroxide (KOH) and zinc chloride ($ZnCl_2$) as the activating agents which were used in various ratios to study their effect on the carbon spheres.
- Synthesize carbon material using chemical vapor deposition (CVD) method under nitrogen gas. Consequently, characterizing the physical, chemical, and electronic properties of NSCS using various techniques.

- Study the effects of surface functionalizing of the prepared NSCS under acidic concentrated solution.
- Synthesize TiO_2 using the sol-gel method to obtain anatase phase nanoparticles.
- Incorporating the prepared TiO_2 nanoparticles into NSCS using the sol-gel method.
- Photocatalytic degradation of Rhodamine B organic pollutant using the as-prepared catalysts.

1.6 Dissertation outline

Chapter 1: Gives a brief introduction about the research topic, problem statement, motivation, aim and objectives of the study.

Chapter 2: Provide a literature review of some of the areas of this research. Textile industries as main contributors to dye wastewater, different types of dyes and their complexities are discussed. TiO_2 catalyst having different polymorphs, its shortcomings, and modification methods previously employed. Since heteroatom doped carbon spheres have been used as support for TiO_2; synthesis methods, different heteroatoms, and their properties are included. The photodegradation process is also reviewed.

Chapter 3: Discuss the characterization techniques on NSCS, TiO_2 nanoparticles, and TiO_2 _NSCS composite.

Chapter 4: Reports on the synthesis of NSCS using onion material and subsequent functionalization of NSCS for use as TiO_2 support.

Chapter 5: In this chapter synthesis of TiO_2 using the sol-gel method, TiO_2 incorporated with as-prepared NSCSs using the sol-gel method is reported with various characterization techniques discussed. Photodegradation of rhodamine B using a catalyst consisting of TiO_2 supported on NSCS is explained and the characterization techniques are used. The effect of parameters such as pH, catalyst loading, and dye concentration was investigated.

Chapter 6: This chapter provides conclusions and recommendations of this research for future studies.

1.7 References

1. Zhu S. & Wang D. Photocatalysis: Basic Principles, Diverse Forms of Implementations and Emerging Scientific Opportunities. Adv. Energy Mater. (2017); 7, 1700841.
2. Serp P. & Figueiredo J.L. Carbon materials for catalysis: Carbon materials in photocatalysis (Chapter 13). Wiley; 1st Ed. (2009); 481-498.
3. Chen X., Liu L., Yu P.Y., & Mao S.S. Increasing Solar Absorption for Photocatalysis with Black Hydrogenated Titanium Dioxide Nanocrystals. Science (2011); 331 (6018), 746-750.
4. Khalid N.R., Majid A., Tahir M.B., Niaz N.A. & Khalid S. Carbonaceous-TiO_2 nanomaterials for photocatalytic degradation of pollutants: A review. Ceram Int. (2017); 43 (17):14552-14571.
5. Mishra A., Mehta A. & Basu S. Clay supported TiO_2 nanoparticles for photocatalytic degradation of environmental pollutants: A review. J Environ Chem Eng. (2018); 6(5):6088-6107.
6. Dvoranová D., Brezová V., Mazúr M. & Malati M.A. Investigations of metal-doped titanium dioxide photocatalysts. Appl Catal B Environ. (2002); 37(2):91-105.
7. Deshmukh A.A., Mhlanga S.D. & Coville N.J. Carbon spheres. Mater Sci Eng R Reports. (2010); 70(1-2):1-28.
8. Faisal A.D. & Aljubouri A.A. Synthesis and Production of Carbon Nanospheres Using Noncatalytic CVD Method. Int J Adv Mater Res. (2016); 2(5):86-91.
9. Paraknowitsch J.P. & Thomas A. Doping carbons beyond nitrogen: An overview of advanced heteroatom doped carbons with boron, sulphur, and phosphorus for energy applications. Energy Environ Sci. (2013); 6(10):2839-2855.
10. Sun Y., Wu J., Tian J., Jin C. & Yang R., Sulfur-doped carbon spheres as efficient metal-free electrocatalysts for the oxygen reduction reaction. Electrochem Acta. (2015); 178:806-812.

11. The World Health Organisation (WHO), ed. State of the Art Report Health Risks in Aquifer Recharge Using Reclaimed Water, (2003).

12. The World Health Organisation (WHO), ed. Reducing Risks, Promoting Healthy Life. Geneva, World Health Organization, (2002).

13. Metcalf and Eddy. Wastewater engineering: Treatment and Reuse (4th ed.). New York: McGraw-Hill, Inc. (2003).

14. UNEP (2002). Stockholm Convention on Persistent Organic Pollutants. United Nations Environment Programme (2002).

15. Li S., Li F., Wang J., Tian L., Zhang H. & Zhang S. Preparation of hierarchically porous graphitic carbon spheres and their applications in supercapacitors and dye adsorption. Nanomaterials (2018); 8, 625-639.

16. Sun S.M. Studies on Photo-Catalysis Degradation of Rhodamine B Using Titanium Dioxide - Carbon Composite Materials. Adv Mater Res. (2012); 485:161-164.

CHAPTER 2: LITERATURE REVIEW

2.1 Background

Most sources of dyes originate from textile, paper, and pulp, pharmaceutical, tannery, craft, and bleaching industries [1]. These industries play a huge role in the residuals of dyes in the environment. However, textile industries have been found to play a huge role in the contamination detected in the natural water resources [1-2]. Textile industries are fabric-based industries that use different chemical-coded colors to produce fabrics [3]. Due to the complexity of the processes employed during the production of fabrics, large volumes of water are used, which is problematic since the contaminated water resulting from the production is not properly treated before it being discharged into the natural water streams [3]. The complexity of the dye structures results in difficulty in their treatment resulting in considerable interest to remove them in natural water streams. Dyes have high thermal and photostability, prolonged half-life, which results in them being difficult to degrade in water even after extended periods [2,4]. For example, the half-life of a reactive blue 19 dye has been reported to be about 46 years at 25 ℃ [4]. This means that it will take 46 years before the components of reactive blue dye fully degrade in the water streams. Subsequently, dyes are carcinogenic in humans and aquatic life, leading to fatality [4,5]. For instance, a concentration level of as low as 0.8 ng/L of Bisphenol-A (BPA) dye present in water can be carcinogenic to humans and result in death in aquatic life [5]. The data acquired on levels of concentrations of different dyes resulting due to effluents discharge have shown that values ranging from 10 mg/L to 700 mg/L have been detected [3-5].

The problem with contaminated water is that it cannot be easily detected physically, the color of the dye-contaminated water is the same as that of uncontaminated water [5]. Even at low concentrations, the presence of dyes in the water bodies affects the transparency and quality of water [5,6]. The moment the wastewater reaches the water streams the dye pollutants settle down where they cannot be easily seen. **Figure 2.1** below illustrates pictures showing (a) colored fabric, (b) discharge of colored wastewater to the water streams, and (c) clear water after a few hours of colored wastewater [6]. According to Pirkarami et al. [7], approximately 5000 tons of dye wastewater from textile industries are discharged into the environment each year. This raised concerns as various kinds of toxic substances are produced by industrial wastewater e.g. cyanide,

oil, fat, and different types of metals which are difficult to treat [7]. Water pollution is a major problem as it leads to the death of the aqua ecosystem due to the chemicals that are present in dye wastewater [5-7]. To avoid the extinction of aqua-ecosystem and increased prices of drinkable water, new approaches for water treatment that are efficient and relatively cheap have been investigated.

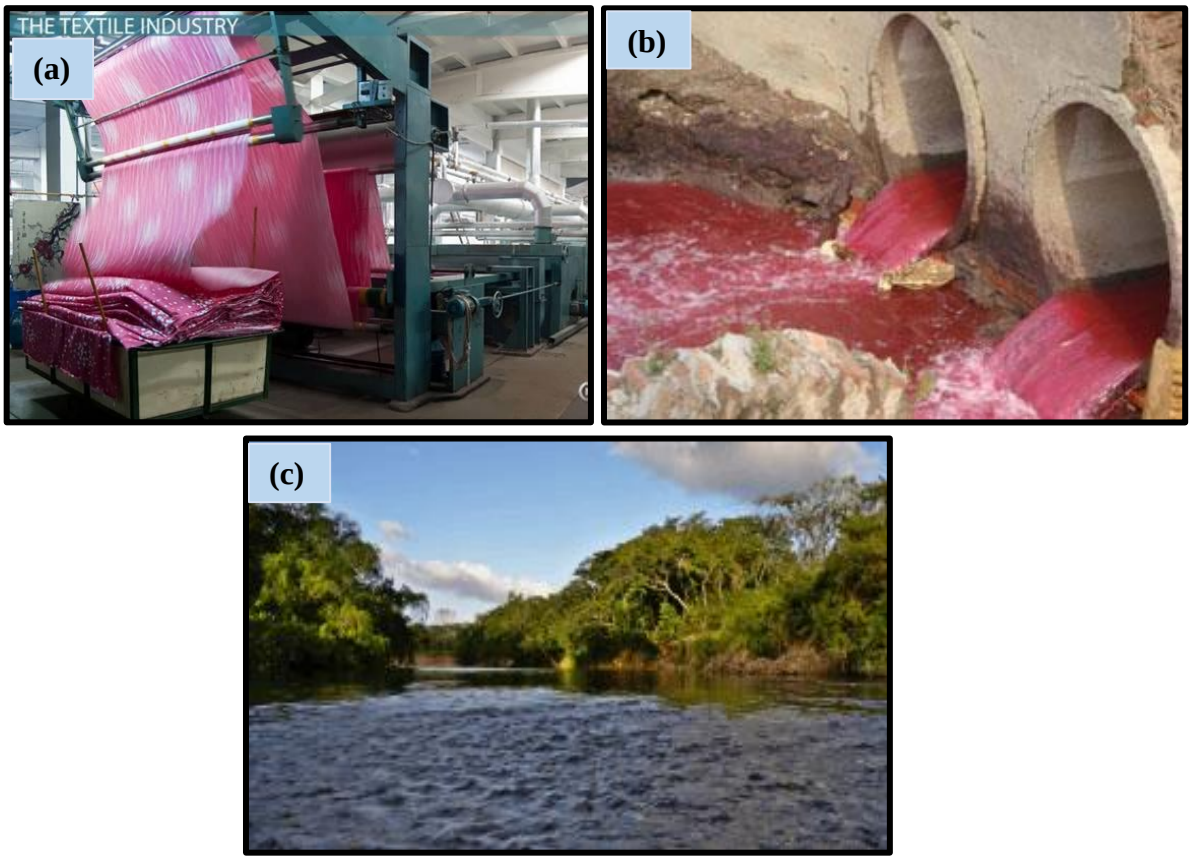

Figure 2.1: Flow diagram of (a) colored fabric, (b) discharge of colored wastewater to the water streams, and (c) clear water after a few hours of colored wastewater [6].

Various kinds of techniques for remediation of dye wastewater have been investigated including; sedimentation, adsorption, chemicoagulation, and biological methods [7]. The difficulties that have been encountered with the use of the above approaches have resulted to further investigations to overcome such difficulties. In biological methods, for example, complex dyes are difficult to degrade and require much time and thus additional energy is consumed [7,8]. Chemicoagulation has also been found to be disadvantageous as it produces colloids and results in increased water pollution. To overcome these drawbacks, new methods have been designed such as ozonation,

photo Fenton processes, and photocatalysis [9,10]. However, ozonation and photo Fenton processes have been reported to be costly and commercially difficult to use [9]. Photocatalytic degradation has been widely investigated as it uses a short retention time, easy to operate and no chemical additives are employed [6,9,10]. It requires ambient conditions to produce excellent results and effects in almost complete mineralization with a shorter retention time as compared to chemicoagulation and biological methods [9,10]. Moreover, activated carbons have been used for pre-treatment and post-treatment for dyes and they were found to remove large quantities of dye concentration as a result of the high surface area they possess [11].

2.2 Classification of dyes

Dyes can be obtained naturally or synthetically; before the mid-nineteenth century, industries that used dyes obtained them naturally [12]. However, currently, dyes that are used in industries are synthetic, which are used for color fabrication in different materials [12]. As a result of their capacity, they have been widely employed by industries [1]. Dyes can be classified as reactive, acidic, azoic, basic sulfur, etc. depending on their application in industries [10]. Acidic dyes are water-soluble anionics that contain sulfonic acid groups an example is Yellow 36 [10]. Acid dyes are applied to different fibres such as silk, wool, and nylon to mention a few. Basic dyes on the other hand have been used on dyeable variants of nylon and polyester. Azoic dyes contain azo group (N=N) attached to aromatic rings [11]. The production of azoic dyes involves mixing of two halves of dyes to produce bright red shades. Most classes of dyes are lacking at producing red shades. The sulfur dyes provide color shades with excellent resistance to washing. However, they use sodium sulfide as a reducing agent which may result in poor resistance to sunlight [10].

Dyes can be either organic or inorganic depending on their structural properties when obtained from the environment [10]. Nevertheless, organic dyes are more prominent and difficult to remove from the environment. Organic dyes can be identified from their aromatic structures and their impact on the environment differs depending on the number of aromatic rings present in the compound [10]. Accordingly, dyes are colored organic pollutants that are mostly released from textile and printing industries into water bodies.

In textile industries where dyes are used to provide color in fabrics, dyes are categorized into electron donors and electron acceptors based on their structural features. For instance, aromatic

groups in the dye compound are classified as electron acceptors (chromogene – chromophore structure) while the other groups such as amines are classified as electron donors (auxochrome groups) [8]. Moreover, dyes that can be found in various colors have been deemed to be environmentally problematic, as they are said to be difficult to degrade using different techniques [10,12]. Dyes that have high chemical stability are most preferred in the textile industries, such as Rhodamine B (RhB) as a result they are being produced in different contents and concentrations [1, 8, 10].

2.3 Rhodamine B

Rhodamine B (RhB) as a synthetic dye is mostly used in cosmetics and textile industries due to its properties such as good stability and solubility in water [13]. RhB has a light absorption peak of 554 nm, and a xanthene group with a cationic charge [13]. As an organic molecule that can be degraded by light, it can be broken down into smaller particles with less harmful molecular structures being produced under the solar radiation technique [14]. Additionally, Rhodamine B dye is fluorescent, categorized as an organic chloride salt shown in its molecular structure in **Figure 2.2 [**14**]**. It is amphoteric and has a rigid structure that makes it more interesting in the textile industry [8]. Conversely, RhB has a molecular weight of $C_{28}H_{30}N_2O_3$, meaning it has aromatic structures of which when disposed to water streams without prior treatment takes time to degrade especially by natural sunlight [15]. The toxicity of RhB has some notable effects on aquatic life and humans [13]. In humans, an intake of contaminated water has been reported to result in skin and eye irritation, respiratory problems, allergic reactions, etc. [13,16,17]. Even though the technology is developing, toxic effluents of RhB are still being detected in wastewater treatment plants [16].

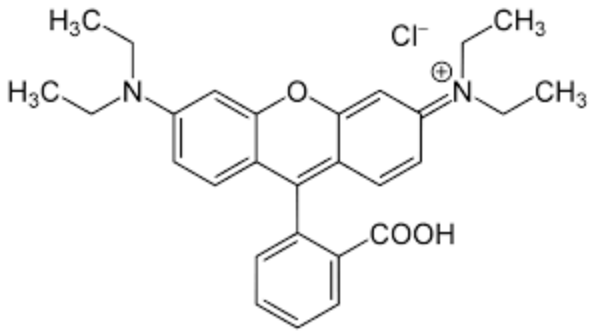

Figure 2.2. Line drawing representation of the molecular structure, Rhodamine B [14].

Degradation of RhB compound has been said to undergo complete mineralization when treated effectively. Moreover, the degradation follows multiple steps with a series of intermediates [18]. The breakdown process undergoes the chromophore cleavage, ring-opening, N-de-ethylation, etc., intermediates under high performance liquid chromatography-mass spectrometer (HPLC-MS) [8,19]. The textile industry employs Physico-chemical combined with an activated sludge process to treat wastewater production after the use of RhB dye [11,17]. The notable problem encountered is the production of a multifaceted sludge consisting of high dye content and other molecules, therefore, requiring post-treatment before disposal [20]. RhB in photodegradation of organic pollutants has seen a huge interest due to its structural complexity seeking to understand its mechanism and reaction pathway. In nanotechnology, photocatalysis has developed into using different catalysts described in the subsequent sections.

2.4 Photocatalysis

Concomitant with pollution minimization efforts, a number of emerging material recovery technologies have been proposed [21-23]. This is because dyes are extremely recalcitrant as they have different chromophoric groups. Different decolorization techniques have been studied for the minimization of colored wastewater such as activated carbon adsorption, chemical oxidation, sonolysis, and photocatalysis [21]. Studies have revealed that using activated carbon adsorption as a method to remove colored wastewater especially for the removal of basic dyes. Most complex dyes consist of the azo bond, chemical oxidation technique was found to be useful in breakage of azo-bond cleavage in different types of dyes [21]. Sonolysis has also been applied as a

decolorization technique, but it was found that it uses sonification method to obtain decolorization. Sonification does not entirely result in complete decolorization as a result it may lead to expensive post-treatment of wastewater [21]. However, these techniques have limitations with thermodynamics, kinetics, sludge regeneration, release of aromatic amines etc. as a result they are still being developed [23]. Photocatalysis on the other hand has been found to be effective for wastewater treatment with very low concentrations of organic dyes at different ranges of pH being employed [7].

Photocatalysis as part of advanced oxidation processes (AOPs) has been extensively researched for the treatment of dye wastewater [7,21-23]. It is an essential process for the treatment of dye wastewater by way of utilizing sunlight-based techniques with no production of sludge after treatment [21]. AOPs have been applied for the degradation of toxic pollutants and in some cases for the pre-treatment to convert recalcitrant pollutants into biodegradable compounds that can later be treated by biological method [22]. Heterogeneous photocatalysis involves mechanisms occurring on the surface of semiconductors such as TiO_2, ZnO, CeO_2, ZrO_2, ZnS, and CdS [7]. Moreover, photocatalysis is advantageous, as the treated wastewater does not result in secondary disposal of toxic wastewater but results in non-toxic waste (carbon dioxide (CO_2), and inorganic salts) that are less environmentally unfriendly. It is well known that nanotechnology-based methods yield desirable results for controllable environmental pollution [21]. As a result, photocatalysis has been studied with the focus on the use of TiO_2 as a catalyst for photodegradation for wastewater purification [11,21,22]. This is as a result of its unique properties such as high crystallinity, different crystalline phases, crystallite size, large accessible surface area, pore structure, pore size, adsorption capacity [23], strong oxidizing power, high chemical stability, and is relatively inexpensive [11].

2.4.1 Titanium dioxide

As a white pigment, titanium dioxide (TiO_2) is usually used in food coloring, paints, personal care products, and as UV absorbers in sunscreens [24-26]. However, the above usages do not result in TiO_2 being fervently researched. The ability to exhibit favorable semiconducting properties has been of interest in different applications including electrochemistry and wastewater treatment [25,26]. TiO_2 in the anatase phase has an indirect bandgap of 3.2 eV with an absorbance of 387.5

nm, while rutile has a direct bandgap of 3.0 eV and an absorbance of 400 nm in the UV region of the solar spectrum [25]. The preference of TiO_2 in the anatase phase is mostly based on the indirect bandgap of anatase compared to the direct bandgap of rutile [25,27]. An indirect bandgap results in photoexcitation of electrons and holes that lead to increased photogeneration lifetime mostly found in the anatase phase. Whereas photoexcitation of electrons and holes that directly result in the formation of electron-hole pair is known as direct bandgap found in rutile and brookite phase [26]. **Figure 2.3** elaborates the mechanism that occurs when bare TiO_2 is used in photocatalysis under a solar simulator [27-29]. As the light of energy greater or equal to that of the bandgap of TiO_2 is irradiated on the catalyst, electrons that are in the valence band (VB) are excited to the conduction band (CB) leaving behind holes in the valence band (**Figure 2.3**). The hole and electron can quickly combine resulting in an electron-hole pair [27]. This electron-hole pair hinders the photocatalytic performance of TiO_2 under the visible region of the solar spectrum [25-29]. During photodegradation, a solution that consists of water (H_2O), pollutants (dyes), and light for irradiation is detrimental. The first equation shown below describes a process where TiO_2 has been exposed to light and the electron-hole pair recombination does not occur (eq. 2.1). In which case the holes in the solution interact with H_2O to form hydroxyl ($^{\cdot}OH$) radicals, which are important for the oxidation process (eq. 2.2). In the valence band where the holes are located, an interaction between holes and pollutant occurs resulting in the pollutant molecules being positively charged (eq. 2.3). The positively charged pollutant interacts with OH radicals breaking down the molecules into carbon dioxide (CO_2) and H_2O (eq.2.4) [27].

$$TiO_2 + h\upsilon \longrightarrow h_{vb}^{+} + e_{cb}^{-} \qquad \text{(eq. 2.1)}$$

$$H_2O + h_{vb}^{+} \longrightarrow {}^{\cdot}OH + H^{+} \qquad \text{(eq. 2.2)}$$

$$h_{vb}^{+} + Pollutant_{(dye)} \longrightarrow Pollutant^{+} \qquad \text{(eq. 2.3)}$$

$$OH + Pollutant_{(sol)} \longrightarrow CO_2 + H_2O \qquad \text{(eq. 2.4)}$$

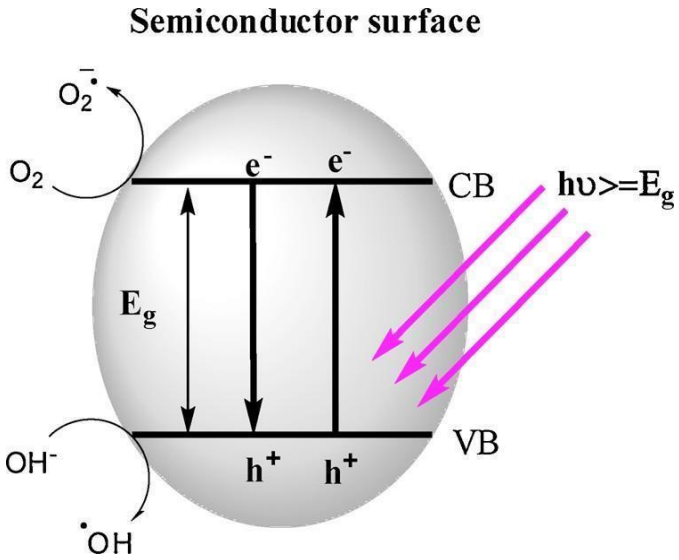

Figure. 2.3. Proposed mechanism for photocatalytic reaction, with a schematic diagram showing electron-hole pairing during heterogeneous photocatalysis [27].

2.4.1.1 Polymorphs of TiO_2

Photocatalytic activity of TiO_2 depends on the crystal phase, surface area, exposed crystals, uncoordinated surface sites, and defects in the lattice structure [30]. TiO_2 exists in three polymorphic phases namely; anatase, rutile, and brookite [31,32]. The crystalline structures of the three polymorphs of TiO_2 are shown in **Figure 2.4**, while their structural parameters are shown in **Table 2.1** [33-35]. The anatase and rutile phases have been reported to be highly active in photocatalytic degradation and thus have been the phases of interest for the past decades [25-32]. Anatase phase, however, has been found to be more active owing to its unique structural properties which include i) better generation of electron-hole pairs, ii) higher amount of hydroxyl groups in the surface which improve chemisorption properties, and iii) lower recombination rate than the rutile phase [23,25].

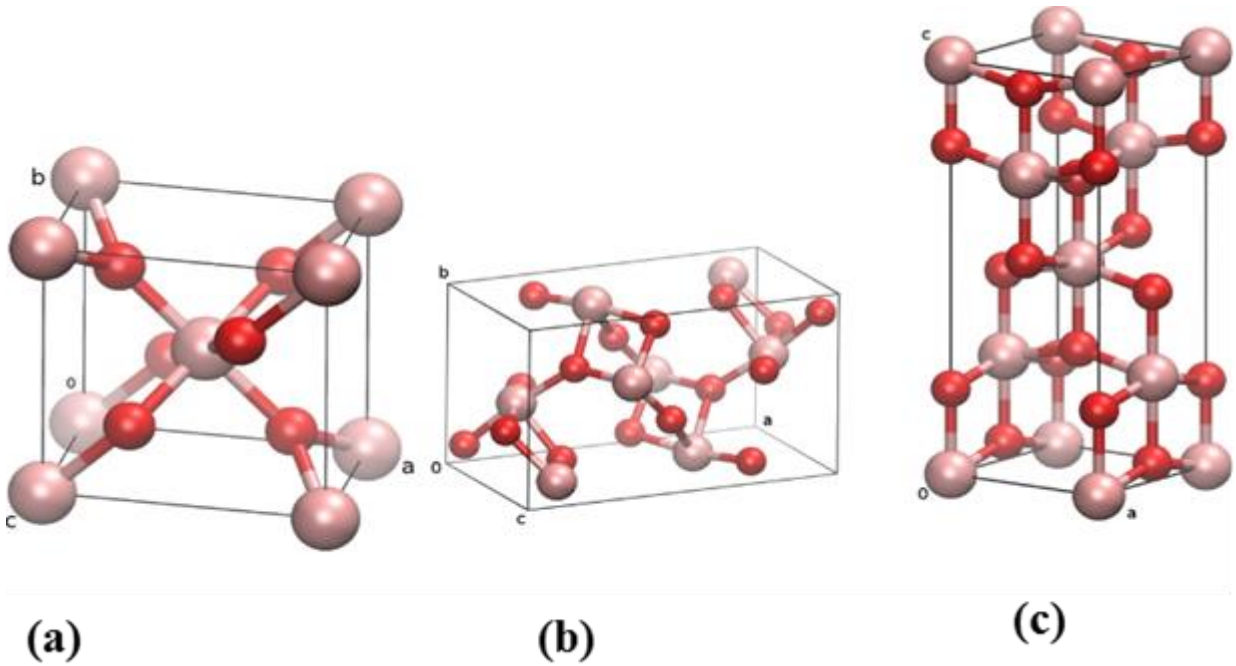

Figure 2.4: Representations of the unit cells of (a) Rutile (b) Brookite) and (c) Anatase polymorphs of TiO_2 [33-35].

Table 2.1 Parameters of TiO_2 polymorphs [33-35].

	Anatase	**Rutile**	**Brookite**
Crystal structure	Tetragonal	Tetragonal	Orthorhombic
Unit cell a (Å)	3.7845	4.5937	5.4558
b (Å)	3.7845	4.5937	9.1819
c (Å)	9.5143	2.9587	5.1429
E_G (eV)	3.2	3.0	3.3

2.4.1.2 Synthesis of TiO_2 particles

Different methods have been investigated for the synthesis of TiO_2 including chemical vapor deposition (CVD), chemical precipitation, hydrothermal, impregnation, mechanical, and alkoxide

sol-gel method [36]. Physico-chemical properties of the metal oxide such as particle size, morphology, and phase formation to produce nanoparticles have been reported to be important [27,37]. Consequently, synthesis methods that produce the desired types of these properties are preferred. However, some of these methods produce highly agglomerated TiO_2 nanoparticles [37-39].

The chemical precipitation method is one of the attractive powder synthesis methods to produce nanoparticles with high specific surface area and improved crystallinity [38]. During the synthesis, a homogeneous mixture of metal oxide and an alkaline chemical (NaOH, NH_4OH, and CH_4N_2O) is formed under altered conditions [36]. The precipitated metal ions are usually precipitated as metal hydroxide, which is later calcined under air. The physical properties of the chemical process that can be altered include synthesis temperature, pH of the solution and solvent, and reactant concentration [40]. However, due to the high agglomeration of TiO_2 nanoparticles, this method has been less investigated especially in photocatalysis application [36,38].

2.4.1.2.2 The chemical vapor deposition (CVD) method

The chemical vapor deposition (CVD) method was developed to grow high-quality crystal nanoparticles of TiO_2. There are two different methods of using CVD: horizontal and vertical systems. In both these systems, the reactants are subjected to high temperatures and gas flow to produce TiO_2 nanoparticles [38,40]. This can be done by controlling parameters such as the crystal structure, nanoparticles thickness, surface morphology, etc. However, due to high temperatures subjected to the material, the anatase phase TiO_2 can be easily converted to rutile phase TiO_2 [39]. This suggests that it is difficult to use the CVD method for the production of just TiO_2 in the anatase phase.

2.4.1.2.3 The hydrothermal method

The hydrothermal method has been reported as a method that produces TiO_2 nanoparticles that are polydispersed and can be used in various applications [40]. The method is operated at low temperatures and high pressures using a stainless-steel autoclave reactor [40]. TiO_2 is mixed with water as a solvent and heated until the optimal time is reached. TiO_2 nanoparticles can be obtained in an anatase or rutile phase depending on the temperature used. Some researchers have concurred

on the anatase to rutile transformation occurring at temperatures greater than 450 ℃ [29,40]. The hydrothermal synthesis method thus is advantageous as the formation of both rutile and anatase phases can be prevented as only low temperatures are used. After the synthesis, the resultant product is dried at low temperatures to avoid agglomeration of the particles and a white powder is obtained [41]. The procedure is economically feasible as it consumes a moderately low amount of energy.

2.4.1.2.4 The sol-gel method

The sol-gel method is suitable for producing metal oxide materials with small particle sizes and high specific surface area [41,42]. Previous studies found that the average particle size that can be obtained from the sol-gel method was approximately 7 nm which was also found to be crystalline [42]. The first step involves metal alkoxide such as titanium (IV) n-butoxide ($Ti(OBu)_4$), titanium (IV) isopropoxide (TTIP), and titanium tetrachloride ($TiCl_4$) being converted to TiO_2 nanoparticles [42]. Usually, for the synthesis of anatase and rutile phases of TiO_2, these precursors are preferred to obtain nanoparticles. $Ti(OBu)_4$ is usually the precursor of choice as the morphology and the particle size can be controlled [42]. In the second step, acidic solvents (nitric acid (HNO_3) and hydrochloric acid (HCl)) are added to the suspension. The acids are added to enhance the formation of the integrated network of nanoparticles (the gel). Homogeneity of the suspension can be obtained by stirring for longer periods under room temperature, as TiO_2 is thermodynamically stable at room temperature [38]. Once the homogeneous solution has been obtained, the liquid phase is removed, and the gel is annealed to enhance the mechanical properties of the metal oxide [38].

2.4.2 Drawbacks of TiO_2 as a catalyst

The chemical interaction of pure TiO_2 with organic pollutants is very slow in the presence of simulated light compared to electron-hole pair recombination. This process limits the use of TiO_2 (both anatase and rutile phase) during the photocatalytic degradation of organic pollutants. As much as extensive investigation on the rutile and anatase phase has been done to overcome these drawbacks in photocatalysis, honing the properties of TiO_2 in the anatase phase has seen more interest [38-43]. The wide bandgap of anatase phase TiO_2 of 3.2 eV limits the extent to which the

catalyst can be used [44]. TiO_2 in its pure state absorbs at 387 nm wavelength constituting only 5% of the solar spectrum (UV region) [44]. This further limits the use of TiO_2 as an environmentally sustainable catalyst. For the TiO_2 in the anatase phase to be more efficient, its absorption wavelength has to be shifted from the UV region to the visible region. To mitigate these limitations of TiO_2, owed to the developing nanotechnology industry, different methods of modification have been reported. Velasco et al. [46] in their study used the sol-gel method to produce carbon spheres/TiO_2 composite followed by annealing at 450 ℃ to obtain anatase phase TiO_2. Their results emphasized the importance of retaining the morphology of TiO_2 in the presence of carbon spheres. However, when the catalyst was used for the degradation of the phenol compounds, the synthesized composite did not completely degrade the pollutant [45-47]. Zhang et al. [48] also used the sol-gel method to synthesize N, S co-doped TiO_2 particles, which resulted in improved surface area when compared to that of pure TiO_2.

2.4.3 Strategies to improve photocatalytic performance of TiO_2

Fabrication of the preparation of TiO_2 has been enormously researched to enhance photocatalytic activity under the visible region of the solar spectrum. Numerous strategies to improve the photocatalytic behavior of TiO_2 have been used to tune the TiO_2 properties [26,45]. Doping of TiO_2 is done either chemically where foreign elements are introduced into the TiO_2 structure or morphologically where the physical properties of TiO_2 are enhanced [46-49]. Metal oxides have been used for incorporation in the crystal lattice of TiO_2. Supports such as metals and non-metals have been investigated due to their pertinent properties [26,29].

2.4.3.1 Doping of TiO_2

Doping of TiO_2 is aimed at improving the optical absorption under the visible region of the solar spectrum. To improve the photoresponse of TiO_2, impurity doping is recommended to extend the spectral response of TiO_2 to the visible region [46]. Cationic doping which focuses on metals as dopants have been found to enhance the activity of TiO_2. However, metals can be chemically reactive when the resulting catalysts are used in photocatalysis [49,50]. Most studies for this type of modification report synthesis of these catalysts using the oxides of the metals, such as K_2O, ZrO_2, etc. to reduce their chemical reactivity [26,49,50]. Elements from groups I and II have also

been used for TiO_2 doping and have shown to increase the quantum efficiency of TiO_2 decreasing electron-hole recombination.

Transition metals have been extensively studied. Metals such as Fe, V, Co, etc. due to their properties that bring forth enhancement in the fabrication of the modified TiO_2 [49-51]. Iron doped TiO_2 was prepared by the hydrothermal method using titanium (IV) tetra tert-butoxide and ferric chloride ($FeCl_3$) as iron precursor. The results showed that the amount of iron ions present in the TiO_2 composite plays an important role in improving the activity of TiO_2 in photocatalysis [50]. In another study, vanadium doped TiO_2 was prepared by the sol-gel method was found to results in red-shift in the UV-vis spectra which in turn showed higher activity in photodegradation of dyes under visible light [49]. The challenge faced with metal doping of TiO_2 is that they block the active sites implying a decrease in photocatalytic activity of TiO_2 [51]. Also, transition metal doping was found to lead to less stable TiO_2 in photocatalytic degradation applications [49].

Anionic doping has recently been found to be of interest as its incorporation into TiO_2 results in a decrease in the bandgap and improved photoresponse characteristics of TiO_2 [26,49-51]. Anionic doping is where elements such as nitrogen, carbon, sulfur, boron, and phosphorus are used as dopants for TiO_2 nanoparticles which can be used in various applications [29,52,53]. Modification of TiO_2 with anions has been found to result in narrow band gap which allows for visible light absorption, impurity energy levels resulting in illumination with visible light allowing for excitation of electrons in the impurity energy level, and oxygen vacancies. Oxygen deficient sites are significant as they block reoxidation [49]. Their dissimilarity in properties is of interest to enhance TiO_2 photocatalytic activity [49-53]. The nitrogen element has been extensively studied as a dopant for TiO_2 [52-57]. As aforementioned, a good catalyst must have a good surface area. Previous studies revealed that doping with nitrogen improves the surface area of TiO_2 [52,53]. This is because nitrogen element has lone pairs of electrons, which when incorporated into the metal oxide, improves bond interaction, and reduces sintering of nanoparticles at high temperatures [52-56]. Sintering is undesired for TiO_2 nanoparticles that will be used for photocatalytic application as this results in a low number of active sites that are exposed for organic degradation [54]. To enhance TiO_2 properties, co-doping of anionic was found to work best because anionic elements have different properties [26,29,49,51]. Additionally, doping with carbon was found to be complex

and their role under UV light is still unclear, however, strong interfacial electronic effects and high specific surface area brought forth by carbon were found to be of importance [23,58].

2.4.3.2 Morphology control of TiO_2

Synthesizing TiO_2 with various methods yield morphological modifications of TiO_2 altering its properties [26,54]. This does not compromise the crystallinity of TiO_2; however, it tailors its morphology. Synthesis designs such as one-dimensional TiO_2 structures that have gone through tailored morphology include TiO_2 in nanotubes, nanoneedles, nanobelts, and nanorods structure, just to mention a few [54]. Various investigation presented tailored morphologies, controlled porosities, and low electron-hole recombination at the grain boundaries of tailored TiO_2 [54]. Morphology control of TiO_2 yields in the tuning of monodispersed TiO_2 nanoparticles that are produced during the synthesis process. Furthermore, TiO_2 form heterojunctions with the other materials improving the visible light absorption. Monodispersed TiO_2 nanoparticles are typically considered favorable in photocatalysis application as they have increased surface area and reduced agglomeration [26,52]. This helps with alteration of charge migration and red shifting in the absorption spectrum [56].

2.4.3.3 Metal oxides with TiO_2

TiO_2 is a semiconductor that has been extensively studied to improve its optical properties. Some of the modification ways that have been researched in the last decades include metal oxides doped with TiO_2 for photodegradation of organic molecules [26]. Metal oxides such as tungsten, nickel, and copper to mention a few, have been found interesting because they result in improved charge separation especially when used in their metal oxide state [26]. Moreover, these metal oxides; tungsten (WO_3), nickel (NiO), and copper (Cu_2O) have comparable crystal radii to that of TiO_2. The reported crystal radii are 0.074, 0.064, 0.083 and 0.087 nm for Ti^{4+}, W^{6+}, Ni^{2+}, and Cu^{2+}, respectively [54]. In addition, the incorporation of metal ions into the crystal lattice of TiO_2 in the anatase phase does not alter the lattice structure of TiO_2 [26]. The incorporation of metal oxides is promising in the formation of acceptor levels which are lower in energy relative to the conduction level of TiO_2. For instance, during the synthesis of tungsten (W^{6+}), it is reduced to W^{5+} species

which acts as a reduction site [26,51]. On the other hand, copper (Cu_2O) allows for electrons to pass to TiO_2 leaving behind holes. This implies that the n-type TiO_2 and p-type Cu_2O heterojunction formation improves the charge separation of the composite [26]. This prevents the fast electron-hole pair recombination during photodegradation. The production of metal oxides with TiO_2 hold significant potential to be developed for further utilization in various applications when optimization of the physicochemical properties is improved.

2.4.3.4 Supported TiO_2 with carbon allotropes to enhance photocatalytic activity

Carbon chemistry is of interest because of its abundance and that it can be tailored to many allotropes with different physical and chemical properties [58]. Understanding the physical and chemical properties of carbon material broadens its scope with different applications [17,46]. Carbon nanotubes (CNTs) for example were found to be of interest due to their one dimension (1D) structural properties [59-62]. Their use as supports for TiO_2 has been widely investigated [58-62]. In a study conducted by Natarajan et al. [63], CNTs with different structures resulted in the suppression of fast electron-hole pair recombination [63-65]. Shaban et al. [66] investigated the degradation of methylene blue using TiO_2 nanoribbons (NRs) modified with CNTs. High degradation efficiency under visible light was observed, concluding that the limitations of TiO_2 were enhanced [66]. Synthesis preparation of TiO_2 with carbonaceous material is important as tuning by controlling composition is achieved. For instance, carbon nanotubes can act as electron sinks or enhance band energy of TiO_2 increasing photocatalytic activity, depending on the synthesis method employed [39].

Other allotropes of carbon such as activated carbon and graphene have also been used to modify TiO_2 [67,69]. Graphene has a two-dimensional (2D) structure with properties such as high electron mobility and high surface area which play a role in the photocatalytic behavior of the modified TiO_2 [67]. TiO_2/graphene composite follows charge transfer mechanism reaction in photodegradation of various dyes [67,70]. Novoselov et al. [70] recorded that graphene has a low Fermi level as compared to TiO_2, allowing electrons during photocatalysis to accumulate on the surface of graphene reducing fast recombination of electron-hole pairs. Similarly, the high performance of TiO_2/graphene composite was prepared and found to work best in increasing the photocatalytic activity of TiO_2 under the solar spectrum [70]. The drawback with this composite

is its reusability, methods to recover the catalyst after photodegradation comes with some difficulties [69-71].

Carbon doped TiO_2 absorbs at wavelengths of up to 535 nm which allows for utilization in the visible region of the solar spectrum [72-75]. Titania hollow spheres (THS) incorporated on carbon were found to have an increase in degradation efficiency when methyl orange (MO) was degraded [76]. However, grinding of carbon-doped THS yielded a reduced degradation efficiency, from this it was deduced that morphology of TiO_2 composite is important in photocatalytic degradation of dyes [76]. Ideally, the bandgap of anatase TiO_2 is reduced as carbon material is introduced into the matrix of TiO_2, however, this trend is not always probable in carbon materials [75]. As much as carbon spheres are easy to control for catalyst-support, TiO_2 nanoparticles tend to agglomerate resulting in poor interfacial contact with the spherical-shaped supports [69]. Carbon spheres (CSs) synthesis is simple and straightforward [55-58]. Their surfaces can be modified by doping with different elements; these include heteroatoms such as nitrogen, sulfur, boron, and phosphorus, which possess different properties and thus improving the properties of CSs as supports [53, 75].

Figure 2.5 illustrates the mechanism that takes place when carbonaceous material support TiO_2 is used under UV and visible region [77]. Titania has unoccupied 3d states into which the extra charge from carbon during incorporation in the TiO_2 matrix can be accommodated [46,59]. During the heterogeneous photocatalytic processes, the reaction takes place on the surface of the semiconductor photoactive material upon light illumination [77]. The heterogeneous process happens in-situ as shown in the figure, where electrons and holes are generated as the photon energy is greater than or equal to the semiconductor falls on the composite surface. The generated electrons and holes initiate the generation of free active radicals on the composite surface, which in turn oxidizes harmful organic pollutants to non-toxic inorganic salts, CO_2, and H_2O [76,77].

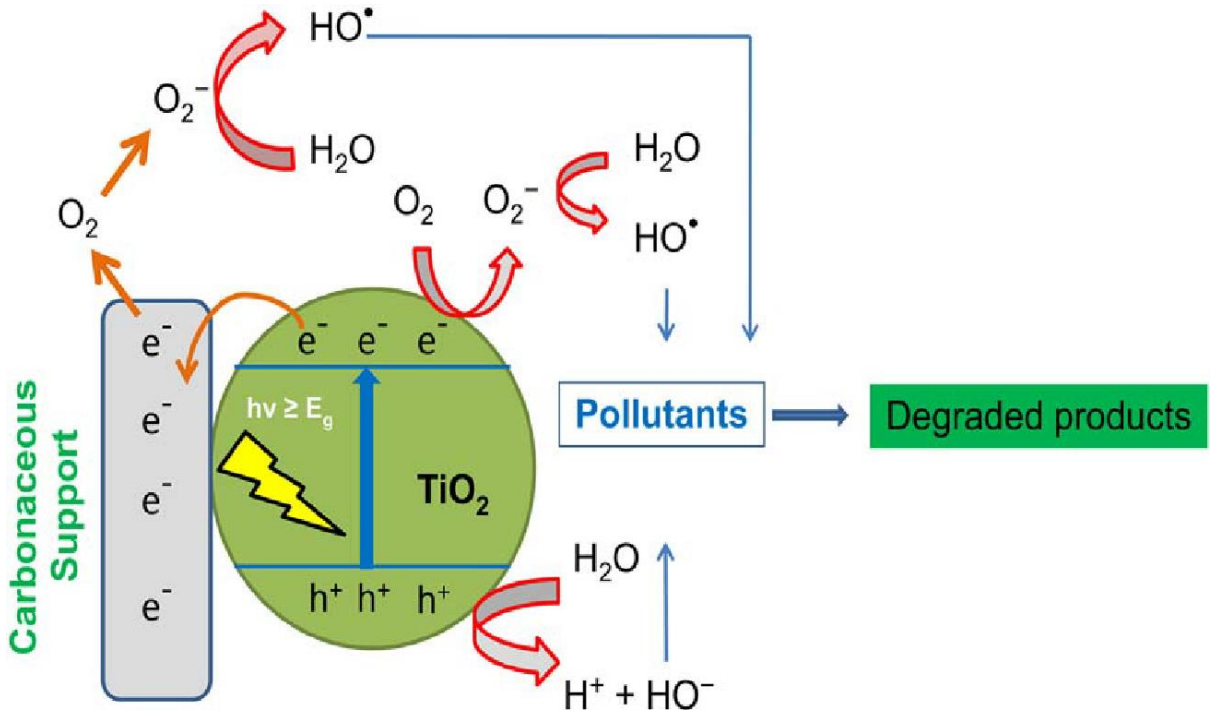

Figure 2.5: Illustration of carbon material support TiO_2 photocatalysis mechanism [77].

2.5 Effect of operational parameters on degradation efficiency

During the degradation of organic pollutants by catalysts, operational parameters play a major role in generating efficient results. Investigating their impact on the photocatalytic degradation processes brings out further understanding of the mechanisms and reactions that take place as light is irradiated onto the suspension. In this study, three operational parameters have been conducted since they were found to be of importance in the degradation of Rhodamine B organic dye: 1) catalyst loading, 2) concentration of dye, and 3) pH of the solution [78]. Explanation of their operation was previously investigated, with recommendation methods to improve them being detailed [67,78].

2.5.1 Catalyst loading

Moderation of catalyst loading was found to be necessary for understanding the amount of the catalyst to be used when reducing undesirable wastewater. A low concentration of catalyst allows

solar light to be highly dispersed in the suspension proceeding with decomposition, whereas a low generation of hydroxyl radicals (·OH) by the catalyst is observed [78,79]. An increase in the catalyst loading results in an increased number of catalyst active sites, high surface area, which results in more ·OH radicals thus improving the degradation efficiency. However, above optimum catalyst loading degradation efficiency decreases due to turbidity in the solution, blocking light absorption [66].

Tayade et al. [78] found that when the catalyst loading was varied, interesting results were obtained. For instance, increasing the catalyst loading above the optimum loading showed to be disadvantageous in terms of the degradation of methyl blue (MB). This can be noteworthily explained by the presence of light scattering and screening effect [78]. Implying that part of the catalyst surface with active sites was blocked as well as absorption and adsorption of photon and dye, respectively. Conversely, the carbon material is non-transparent, hindering the active site in TiO_2 catalyst leading to what has been named the shielding effect [79-81]. The shielding effect occurs when carbon added to TiO_2 suspension exceeds the optimum loading.

2.5.2 Dye concentration

Obtaining optimum dye concentration is important in the degradation of dye pollutants. In a study conducted by Tayade et al. [78], observed that with optimal operational parameters, a decrease in both degradation and decolorization of the dye in the solution is possible. When a low dye concentration was used, photons entered the solution faster as compared to when a high dye concentration was used [78]. An increase in initial dye concentration decreased the degradation efficiency of the composite as time progressed [78]. The reduction in degradation efficiency implies that hydroxyl radicals (·OH) have been consumed by the reactant [67,78]. The adsorption of the dye occurs on the surface of the catalyst with ·OH radicals being active, as a result increasing the initial dye concentration leads to blocked photons on the catalyst surface [82].

2.5.3 The pH of the solution

In pH studies, it is important to measure pH before degradation and take the final pH when the degradation is complete. The procedure helps gather more information about the mechanism that

occurs during dye degradation [84]. Alternatively, it is imperative to monitor the pH of the suspension as electron-proton trapping is observed [84]. TiO_2 has a point zero charge (pH_{zpc}) of 6 implying that at pH below 6, TiO_2 is positively charged whereas at pH above 6 it is negatively charged [78]. Consequently, varying pH will have an impact on the degradation of the catalyst. In photocatalytic degradation, a neutral final solution is desirable; neutral pH implies that degradation took place but most importantly, it gives more information about the remaining compounds in the solution. Adjusting the pH of the solution with acidic media (H_2SO_4) yields, positively charged TiO_2 surface which decreases both degradation and decolorization shown by **eq. 6**. Using basic media (NaOH) results in a negatively charged surface of TiO_2 shown by **eq. 7**, at which it was reported that there was a decrease in the degradation of the solution being attributed to inhibition of light penetration by the highly negative surface of the catalyst [78].

$$TiOH + H^+ \leftrightarrow TiOH_2^+ \qquad \text{(eq. 2.6)}$$

$$TiOH + OH^- \leftrightarrow TiO^- + H_2O \quad \text{(eq. 2.7)}$$

2.6 Carbon nanomaterials

Fullerenes were the first carbon allotropes that were discovered, and their study led to the later discovery of other shaped carbon nanomaterials [85]. Carbon spheres can have hollow, solid, and core-shell morphology. The outer carbon layer of carbon spheres has multiple layers, meaning it is thicker than that of fullerenes [85]. The major difference between carbon spheres and fullerenes is that carbon spheres are made of a discontinuous carbon layer whereas fullerenes are made of a continuous carbon layer [58,85]. Carbon spheres have been classified according to their arrangement of carbon layers such as being concentric, radial, or random [85]. Spherical carbons can also be classified according to their particle size; fullerenes are classified as carbon spheres with particle sizes less than 2 nm, carbon onions are between 2-20 nm, carbon spheres are between 50-1000 nm, and carbon beads above 1 μm. Carbon spheres with diameters less than 100 nm accrete forming chain-like structures [58].

The discovery of carbon led to manifold research worldwide being conducted for different applications [58,85-87]. Carbon spheres are viewed to have a graphene layer that allows them for fabrication in diamond films, special rubber additives, etc. Although relative to industry applications, carbon spheres can be broadly applied, there is a lack, therefore of preparing a large

number of carbon spheres under industrial-scale conditions [86,88]. In most applications, carbon spheres of interest have to be porous.

2.6.1 Carbon spheres

Carbon is a lightweight element and permits the ability to visualize carbon at the nano-level. This allows for the achievement of various synthesis methods and their different morphologies [90,91]. Interest in carbon spheres is attributed to their properties; high surface area, high thermal stability, high strength, and unique electronic properties [58,85,90,91]. Also, carbon spheres have been reported to show controllable particle size distribution, regular geometry, good liquidity, and graphitization [89,91]. Moreover, carbon spheres (CSs) are classified from microspores (below nm), mesoporous (2-50 nm), and macrospores (greater than 50 nm) [89-92]. Nanomaterials with a high surface area that allows for use in different applications are mostly preferred over bulk materials. The two types of carbon spheres that have been extensively studied: hollow carbon spheres (HCS) and solid carbon spheres (SCS) [91-93]. The focus in this study is on solid carbon spheres since they can be soluble and wettable which led to their wide range of applications that include dye encapsulation, lithium batteries, enzyme and protein protection, fuel cells, and removal of contamination in wastewater [94,95].

2.6.1.1 Synthesis of carbon spheres

Various synthesis methods have been proposed for the preparation of carbon spheres, these include arc discharge, laser ablation, and plasma processes, shock compression techniques, chemical vapor deposition (catalytic and non-catalytic), and autoclave process (catalytic and non-catalytic) [90,96-98]. The quest is to find a method that is relatively cheap and environmentally friendly, to be used for the production of carbon spheres [46]. Carbon spheres with high yield are mostly formed at temperatures above 700 ℃ and below 1000℃, depending on the choice of synthesis technique [46,58,96]. Due to the strong interaction between the carbon atoms, carbon spheres tend to agglomerate. Agglomerated carbon spheres are detrimental as they result in quasi-carbon spheres than the pronounced shape of spheres [85,88]. To overcome this limitation, Miao and colleagues [88] investigated the role of flow rate when annealing carbon spheres using the CVD method. They found that a flow rate of 200 sccm of inert gases plays a huge role in dispersing carbon spheres

with distinct spherical shapes [88]. They concluded that depending on the carbon precursor, nitrogen gas is the most preferred gas to be used while monitoring its flow rate [88,94,96]. On the other hand, gases such as ethylene, air, and hydrogen have also been used for the formation of CSs [94].

Although to produce quality carbon spheres it can be concluded that longer reaction times are much preferable, this results in agglomerated spherical shapes of the carbon material and bigger particles being formed [95]. Miao et al. [88] found that although prolonged synthesis temperatures resulted in a high yield of carbon spheres, these became agglomerated which are difficult to separate through grinding or sonication. Agglomeration of carbon radicals during pyrolysis is inevitable, although homogeneously preparing the samples was found to reduce agglomeration of active sites [99,100]. The preparation of carbon spheres is very sensitive to the type of carbon precursor used. In previous studies, carbon precursors such as polysaccharides, glucose, sucrose, and cyclodextrin have been used of which are synthetic precursors [92,101]. These carbon sources have been found to provide good dispersion on carbon spheres and they have been employed for different applications [92-101]. Reducing the time taken to anneal carbon spheres has been suggested to reduce agglomeration of carbon spheres, shown in **Figure 2.6** (**a**) [88]. In an attempt to separate carbon spheres that were produced from Kaolin, a 48% hydrofluoric acid (HF) solution was used [88]. The resulting carbon spheres maintained the shape. This meant that HF did not affect the spherical shape, although improvements to separate carbon spheres were unsuccessful as the produced spheres were still agglomerated, **Figure 2.6** (**b**) [88].

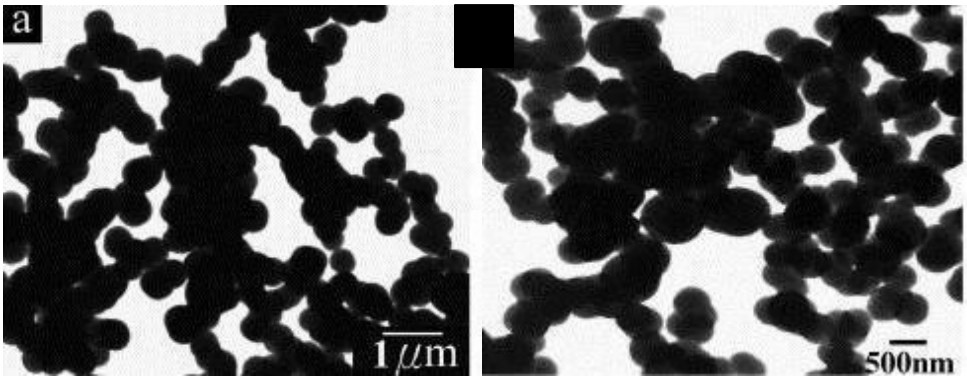

Figure 2.6: TEM images of (a) carbon spheres prepared by Kaolin at 200 sccm flow rate and (b) treated by HF (48%) solution [88].

Another study conducted by Zhang et al. [101] focused on finding methods that will disperse agglomerated carbon spheres. Obtained carbon spheres were synthesized at temperatures ranging from 600 – 1400 ℃. The obtained carbon spheres were graphitic, possessing properties such as high electrical and thermal conductivities and high strength with a diameter of 10-200 nm [101]. The resultant carbon spheres were agglomerated which meant that the diameter size was larger than desired. In an attempt to separate the agglomerated spheres, ultra-sonication of the product was proposed. This was done by dispersing the resultant carbon spheres in a polar solvent and ultra-sonicate for longer hours. They found that the ultra-sonicated carbon spheres resulted in less agglomeration of carbon spheres; even though interaction with each carbon atom was still present [101].

2.6.1.2 Strategies for improving chemical and physical properties of carbon spheres

Carbon spheres can be used in different applications due to their interesting properties [102]. However, the incorporation of heteroatoms into carbon materials has developed due to the manifested interest in the unique properties brought about by these elements [53]. Heteroatoms of interest include nitrogen, sulfur, boron, and phosphorus that all exhibit different properties of interest [53,58,92]. Many recent studies have focused on the production of carbon spheres as support for catalysts [103]. Indeed, undoped carbon spheres as support for catalysts demonstrate large surface areas although the degradation efficiency under visible light did not show an increase [104]. As a result, recent developments and investigations have focused on improving the properties of carbon spheres as support materials [53,58,96].

2.6.1.2.1 Heteroatom dopants for carbon spheres

The carbon element is relatively closer to the nitrogen element in the periodic table as a result, most studies have focused on nitrogen heteroatom on carbon impregnation to improve carbon properties [105, 106]. Carbon and nitrogen join chemically and result in better properties for varied applications [106-109]. Nitrogen doping achieves less coarseness and agglomeration of the carbon material, this owing to its chemical properties that are of interest when incorporated in carbon [109,110]. Interest in the use of nitrogen as a doping element for carbon material stimulates the properties of nitrogen such as being an n-type dopant with an extra electron that allows for donation

when carbon is replaced in the carbon matrix [106-111]. It has been reported that carbon spheres incorporated with nitrogen bonds have these three configurations: i) pyridinic, ii) pyrrolic, and iii) quaternary (**Figure 2.7)** [57,112,113]. Subsequently, carbon-doped with nitrogen in some cases results in nitrogen atoms being found on the edges of carbon layers, which in turn play a huge role in improving the properties of carbon materials [53,114].

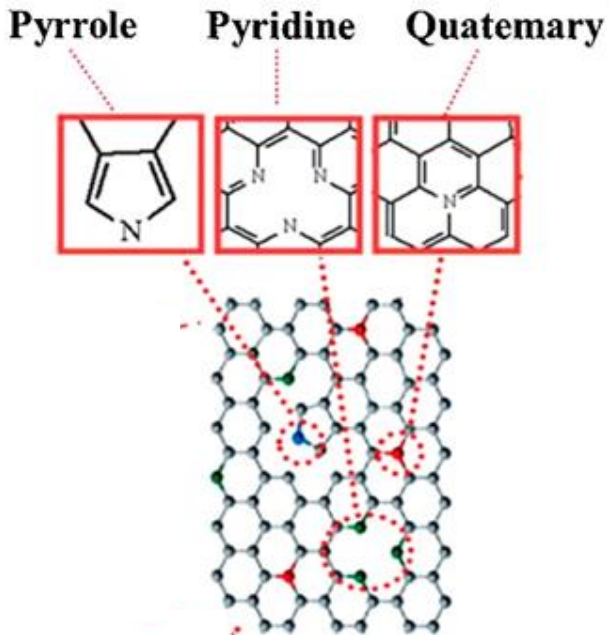

Figure 2.7: Incorporation of nitrogen onto the carbon sphere matrix [113].

Modification with boron incorporated into the carbon material has mostly been studied for fuel cell application [53]. Carbon nanotubes were the first to be incorporated with boron for oxidation-reduction reactions (ORR) application to enhance electrocatalysts activity [115,116]. Enhanced properties of carbon nanotubes incorporated with boron heteroatom were explained by the lower electronegativity of boron and durability of the catalyst when employed in fuel cells. Unlike nitrogen doping on carbon material, boron introduces p-type doping, that is electron deficiency bringing a new type of interaction with carbon atoms [115-117]. This recently discovered information about boron led to doping with other carbon allotropes being investigated, including hollow carbon spheres (HCSs) for application in various fields [111].

Sulfur doping has also been studied. A recent study that was conducted using carbon materials with sulfur sources obtained S-doped carbon with microspherical morphology with a high surface area as was confirmed by BET [118]. However, doping with sulfur is presumed difficult due to its

large atomic size and different binding behavior of sulfur atoms [73]. Large atoms and lone pairs of sulfur are believed to be the reason behind the enhancement of carbon materials properties such as its catalytic activity [53,118]. On the other hand, sulfur alters the spin density, polarizability, and structural defects of the carbon matrix thus improving its properties and allowing for vast applications such as in the photodegradation of organic pollutants [53,118,119].

The incorporation of phosphorus in carbon material was revealed to increase the catalytic activity together with the improvement of electron-donor properties [53]. Wu et al. [120] investigated the incorporation of phosphorus in hollow carbon spheres as electrocatalysts. Phosphorus was chosen among other heteroatoms due to its low electronegativity and large covalent radius believed to alter the structure and activity of carbon [120,121]. Modification of carbon material with phosphorus has been investigated for application as electrocatalysts in oxygen reduction reactions (ORR) [120].

As interest in heteroatoms developed, co-doping with each heteroatom mostly with nitrogen in anticipation to expand the already known properties has been investigated [53]. In essence, co-doping of heteroatoms brings forth synergistic effects on the matrix of the carbon material [94]. The effect on dual doping of nitrogen and phosphorus with carbon material was investigated [121, 122]. The studies found that nitrogen-phosphorus doping is an effective way to enhance the catalytic performance of carbon spheres. The conclusion was that each heteroatom brings forth its properties into the carbon material, which are unique and enhances the properties of carbon spheres [94,121-122]. Moreover, dual doping of phosphorus with nitrogen provided interesting characteristics especially since their electronegativity is very different [121]. Meanwhile, sulfur-nitrogen co-doping is relatively rare; however, it has been reported to enhance electrocatalysts in the application of ORR [123]. Boron and nitrogen were also investigated with carbon material, this pair was found to enhance carbon properties compared to monodoping of either of these heteroatoms [92,124]. Boron-Nitrogen-Phosphorus doping has been found to work best in improving carbon properties; however, more investigation is yet to be done to understand the fundamental principle of three-way doping [53].

2.6.1.2.2 Functionalisation of carbon spheres

The surface of carbon spheres is chemically inert, thus functionalization and doping have been used to enhance their wettability [58]. Functionalization of carbon spheres can be done during their synthesis, by heteroatom modifications where different functional groups are introduced into the graphitization of carbon spheres [90]. Moreover, functionalization is done to i) improve the carbon nanomaterial interaction with solvents and dispersion, ii) allow the attachment of metal nanoparticles, iii) modify the carbon nanomaterials adsorption properties, and iv) allow further chemical treatment on the carbon nanomaterials [90,125]. Surface functionalization of carbon spheres by oxidizing agents such as nitric acid (HNO_3), and sulphuric acid (H_2SO_4) introduces polar groups such as hydroxyl (^-OH), carboxyl (^-COOH), and carbonyl ($^-C=O$) which can be detected using the FTIR technique [69,90]. The introduction of polar groups to the surface of carbon spheres provides binding sites, which can be used when the material is incorporated with metal oxides for application in photocatalysis [88,125-129]. Illustration of surface functionalization by nitric acid (HNO_3) and sulphuric acid (H_2SO_4) is illustrated in **Figure 2.8** [90].

Carbon has both sp^2 and sp^3 hybrid orbitals, however, when functionalized with nitrogen it has been found that the carbon content reduces while the oxygen percentage increases and different bonds formed. The C-N, C=N, and N-O/N_2 bonds are imperative in photocatalysis as bonding sites for TiO_2 when nitrogen-doped carbon spheres used as support have been observed. Structural and binding properties of carbon spheres are shown to be enhanced as nitrogen atoms are incorporated [128].

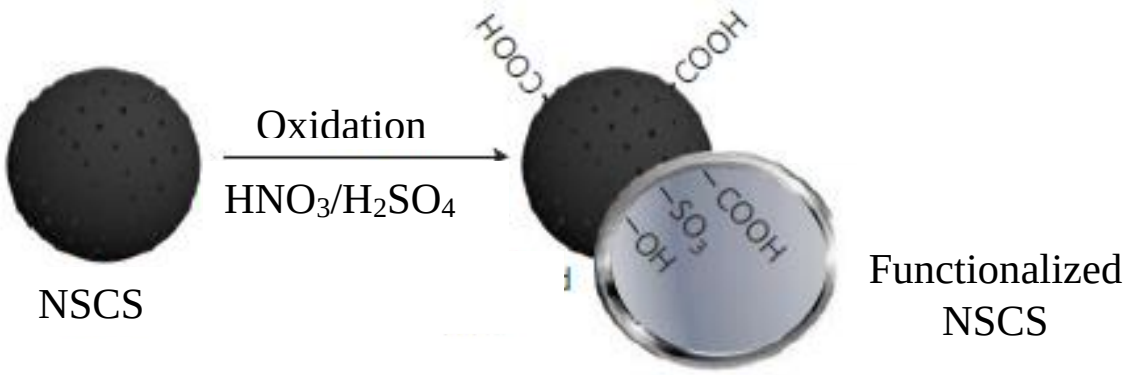

Figure 2.8: Functionalization of nitrogen, sulfur co-doped carbon spheres [90].

2.7 Green methods for the production of intrinsically doped Carbon Spheres

Green technology has developed in the past decades mostly as a substitute for synthetic carbon precursors by using natural precursors [130,131]. Health has to be prioritized when dealing with nanomaterials. As a result, sustainable chemistry aims at reducing the environmental effect caused by carbon materials preventing environmental pollution [131]. Consequently, leading to more focus on materials that are relatively cheap, renewable, economically viable, and environmentally friendly [130]. Hydrothermal carbonization using carbohydrates, fat, and protein has been one of the methods of interest to obtain carbon materials incorporated with heteroatoms. These carbon precursors contain heteroatoms before synthesis, producing self-doped carbon spheres or intrinsically doped carbon spheres [131-134]. In these studies, a single natural material is used as an all-in-one precursor for the carbon material and most interestingly as the heteroatom dopant [133]. During the synthesis of carbon spheres using the hydrothermal process, some of the minerals during the process dissolve in water and therefore do not participate in the carbonization reaction [132]. This then allows pure carbon spheres with heteroatoms to be obtained [132]. The sustainability of natural precursors has been reported to be manageable, and follow straightforward synthesis techniques, including the hydrothermal and the CVD processes [134]. A notable difference between self-doped precursors and post-doped precursors can be elaborated. Post doping is an extrinsic doping effect in which the amount of a specific dopant can be controlled e.g. 5 % or 10 % doping, depending on the amount required. While self-doping has been reported to result in a homogeneous distribution of the dopants, as it is an intrinsic doping effect [130,134]. Recently, progression in the various focus of green technology has been observed for use in different applications, some of the recent discoveries will be discussed.

Yu et al. [122] reported on the use of baking yeast as a carbon, nitrogen, and phosphorus source to synthesize N, P co-doped carbon spheres for application in electrochemistry. The main constituents of yeast are nitrogen, phosphorus, carbon, oxygen, and hydrogen elements [122]. The simple synthesis method, the hydrothermal method was followed to obtain co-doped carbon spheres. It is well known that using an autoclave technique results in less desired spherical shapes of carbon [122,133]. To improve the morphology, the CVD method was used to anneal the N, P co-doped carbon spheres under nitrogen gas [122]. For electrochemical applications surface area

of the catalyst is explained to be important, the authors reported an improved specific surface area of 1223 m^2 g^{-1} [122]. They concluded that N, P co-doped carbon spheres obtained from baking yeast without any use of templates proved to improve the catalytic activity of the electrocatalysts [122].

Ratchahat et al. [132] investigated the use of the hydrothermal process in the preparation of carbon microspheres using starch. The hydrothermal process was used with deionized water as a solvent. Carbonization under nitrogen atmosphere was later conducted using the CVD method [132]. On the other hand, oatmeal was investigated for sodium-ion battery application [113]. **Figure 2.9** illustrates an example of raw oatmeal and its constituents; nitrogen, carbon, hydrogen, and oxygen [113]. The nitrogen, doped-carbon spheres were obtained with long-term stability being one of the improved properties [113]. The effect of catalytic properties of nitrogen self-doped carbon materials may be due to the overlapping effects, catalysis by basic surface sites, and by electron donation [99]. An advantage of using natural precursors is that there is no need for surfactants or any organic solvents. Subsequently, the drawback of using raw natural precursors found was the agglomeration and the chain-like morphology explained to be as a result of the van der Waals forces between carbon-carbon interaction during the pyrolysis process [57,76,134]. Thus, activating agents are required to produce spherical shapes for carbons obtained from natural materials, as will be discussed below.

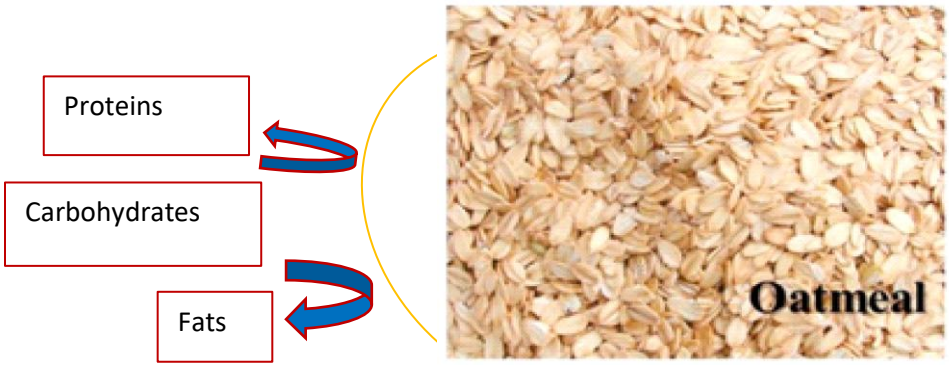

Figure 2.9: Schematic illustration of oatmeal with its nutrients [113].

2.7.1 Activating agents

Chemical activation is a procedure mostly done for carbon material obtained from natural products. The addition of activating agents is done using chemical activation where the activating agent is added to the carbon material before pyrolysis [135,136]. Subsequently, a homogeneous mixture of carbon spheres is produced. Frequently used activating agents consist of potassium hydroxide (KOH), sodium hydroxide (NaOH), and zinc chloride ($ZnCl_2$) [135,137]. According to Lozano-Castello et al. [136] after the heat treatment of the carbonaceous material, there is an improvement in the porosity and the spherical shape of the material. However, the disadvantage of chemical activation is the copious washing that is employed on the resulting material to remove any residuals of the activating agent. In this step, some of the chemical properties of the carbon material may be lost resulting in the material that is unproductive for different applications [135].

Using KOH as an activating agent was reported to result in microporous material, which is important for some applications [136]. KOH has a melting point of 360℃ meaning it melts at high temperatures and this is disadvantageous as it crystallizes the material at high temperatures (above 600℃) since KOH transforms to K_2CO_3 [136]. NaOH on the other hand has been described to work best as an activating agent for carbon spheres since it is less costly as compared to potassium hydroxide [137]. Whereas $ZnCl_2$ was found to be a better activating agent to obtain pronounced carbon spheres as it is assumed that it is controllable when it comes to the removal of the metal and the chlorides using hydrochloric acid (HCl) mixed with distilled water [138,139].

2.8 References

1. Zaharia C. & Suteu D. Textile organic dyes: characteristics, polluting effects and separation/elimination procedures from industrial effluents. A critical review. (2012); 2741, 31.
2. Kapias T. & Griffiths R.F. Accidental releases of titanium tetrachloride ($TiCl_4$) in the context of major hazards—spill behavior using REACTPOOL. Journal of Hazardous Materials A119 (2005); 41–52.
3. Carneiro P.A., Umbuzeiro G.A., Oliveira D. P. & Zanoni M.V.B. Assessment of water contamination caused by a mutagenic textile effluent/dye house effluent bearing disperse dyes. J. Hazard. Mater. (2010); 174, 694–699.
4. Weber E.J. & Stickney V.C. Hydrolysis kinetics of reactive blue19-vinyl sulfone. Water res (1993); 27:63-67.
5. Krupadam R.J., Khan M.S. & Wate S.R. Removal of probable human carcinogenic polycyclic aromatic hydrocarbons from contaminated water using molecularly imprinted polymer. Water Res. (2010); 44, 681–688.
6. https://www.trustedclothes.com/blog/2018/05/08/why-we-need-to-get-rid-of-azo-dyes (2019-09-04: 16:15).
7. Pirkarami A. & Olya M.E. Removal of dye from industrial wastewater with an emphasis on improving economic efficiency and degradation mechanism. Chem Soc. (2017); 179-186.
8. Hai F.I., Yamamoto K. & Fukushi K. Hybrid treatment systems for dye wastewater. Crit Rev Environ Sci Technol. (2007); 37(4):315-377.
9. Lahkimi A., Oturan M.A., Oturan N. & Chaouc M. Removal of textile dyes from water by the electro-Fenton process. Environ. Chem. (2007); 5(1), 35-39.
10. Saini R.D. Textile organic dyes: Polluting effects and elimination methods from textile wastewater. Int. J. Chem. Eng. (2017); 121-136.
11. Serp P. & Figueiredo J.L. Carbon materials for catalysis. Carbon as catalyst support (Chapter 4). Wiley; 1st Ed. (2009); 131-150.
12. Mishra G. & Tripathy M. A critical review of the treatments for decolourization of textile effluent, Colourage (1993); 40: 35–38.

13. Yu K., Yang S., He H., Sun C., Gu C. & Ju Y. Visible Light-Driven Photocatalytic Degradation of Rhodamine B over NaBiO3: Pathways and Mechanism. J. Phys. Chem. A (2009); 113, 10024–10032.
14. Zhao J., Wu T., Wu K., Oikawa K., Hidaka H. & Serpone N., Photoassisted degradation of dye pollutants. 3. Degradation of the cationic dye rhodamine B in aqueous anionic surfactant/TiO_2 dispersions under visible light irradiation: evidence for the need of substrate adsorption on TiO_2 particles. Environmental science & technology. (1998); 32(16), 2394-2400.
15. Kansal S.K., Singh M. & Sud D. Studies on photodegradation of two commercial dyes in aqueous phase using different photocatalysts. Journal of Hazardous Materials 141 (2007); 581–590.
16. Pan H.M., Feng J.H., He G.X., Cerniglia C.E. & Chen H.Z. Anaerobe, (2012);18: 445
17. Baca M., Wenelska K., Mijowska E., Kaleńczuk R.J. & Zielińska B. Physicochemical and photocatalytic characterization of mesoporous carbon/titanium dioxide spheres. Diamond & Related Materials 101 (2020); 107551.
18. He Z., Sun C., Yang S., Ding Y., He H. & Wang Z. Photocatalytic degradation of rhodamine B by Bi_2WO_6 with electron accepting agent under microwave irradiation: mechanism and pathway, J. Hazard. Mater. (2009); 162 1477–1486.
19. Chen F., Zhao J. & Hidaka H. Highly selective deethylation of Rhodamine B: Adsorption and photooxidation pathways of the dye on the TiO_2/SiO_2 composite photocatalyst. Int. J. Photoenergy (2003); 5 209–217.
20. Cinelli G., Cuomo F., Ambrosone L., Colella M., Ceglie A., Venditti F. & Lopez F. Photocatalytic degradation of a model textile dye using Carbon-doped titanium dioxide and visible light. Journal of Water Process Engineering (2017); 20 71–77.
21. Dias P., Lopes T., Andrade L. & Mendes A. Temperature effect on water splitting using a Si-doped hematite photoanode. J Power Sources. (2014); 272:567-580.
22. Cong Y., Zhang J., Chen F., & Anpo M. Synthesis and characterization of nitrogen-doped TiO_2 nanophotocatalyst with high visible light activity. Journal of Physical Chemistry C, (2007); 111(19), 6976–6982.

23. Mamaghani A.H., Haghighat F. & Lee C.-S. Photocatalytic oxidation technology for indoor environment air purification: The state-of-the-art. Applied Catalysis B: Environmental (2017); 203 247–269.
24. Hua Z., Dai Z., Bai X., Ye Z., Wang P., Gu H. & Huang X. Copper nanoparticles sensitized TiO_2<inf>2</inf> nanotube arrays electrode with enhanced photoelectrocatalytic activity for diclofenac degradation. Chem Eng J. (2016); 283:514-523.
25. Kwon S., Fan M., Cooper A.T. & Yang H. Photocatalytic Applications of Micro- and Nano-TiO_2 in Environmental Engineering. Vol 38; (2008).
26. Dahl M., Liu Y. & Yin Y. Composite Titanium Dioxide Nanomaterials. Chem. Rev. (2014); 114, 9853−9889.
27. Mishra A., Mehta A. & Basu S. Clay supported TiO_2 nanoparticles for photocatalytic degradation of environmental pollutants: A review. J Environ Chem Eng. (2018); 6(5):6088-6107.
28. Wu M.C., Hsiao K.C., Chang Y.H. & Chan S.H. Photocatalytic hydrogen evolution of palladium nanoparticles decorated black TiO_2 calcined in argon atmosphere. Appl Surf Sci. (2018); 430:407-414.
29. Dvoranová D., Brezová V., Mazúr M. & Malati M.A. Investigations of metal-doped titanium dioxide photocatalysts. Appl Catal B Environ. (2002); 37(2):91-105.
30. Khataee A.R. & Kasiri M.B. Photocatalytic degradation of organic dyes in the presence of nanostructured titanium dioxide: Influence of the chemical structure of dyes. J Mol Catal A Chem. (2010); 328 (1-2):8-26.
31. Chen S., Wang Y., Li J., Hu Z., Zhao H., Xie W. & Wei Z. Synthesis of black TiO_2 with efficient visible-light photocatalytic activity by ultraviolet light irradiation and low temperature annealing. Mater Res Bull. (2018); 280-287.
32. Chen X., Liu L., Yu P.Y. & Mao S.S. Supporting Material for Increase Solar Absorption for Photocatalysis with Black Hydrogenated Titanium Dioxide Nonocrystals. Science (80). (2011); 331:746-751.
33. Scarpelli F., Mastropietro T.F., Poerio T. & Godbert N. Mesoporous TiO_2 Thin Films: State of the Art. Interchopen. (2018).

34. Moellmann J., Ehrlich S., Tonner R. & Grimme S. A DFT-D study of structural and energetic properties of TiO_2 modifications. J. Phys.: Condens. Matter 24 (2012); 424206 (8pp).
35. Sze Tung W. & Daoud W.A. Self-cleaning fibers via nanotechnology: A virtual reality. Journal of Materials Chemistry. (2011); 21:7858-7869.
36. Srinivasu P., Singh S.P., Islam A. & Han L. Novel approach for the synthesis of nanocrystalline anatase titania and their photovoltaic application. Adv. Optoelectron. (2011).
37. Watson S. S., Beydoun D., Scott J. A. & Amal R. The effect of preparation method on the photoactivity of crystalline titanium dioxide particle. Chemical Engineering Journal 95 (2003); 213–220.7
38. Ahmad Md. I., Fasel C., Mayer T., Bhattacharya S.S. & Hahn H. High temperature stability of nanocrystalline anatase powders prepared by chemical vapour synthesis under varying process parameters. Applied Surface Science 257 (2011); 6761–6767.
39. Miranda S.M., Romanos G.E., Likodimos V., Marques R.R.N., Favvas E.P., Katsaros F.K., Stefanopoulos K.L., Vilar V.J.P., Faria J.L., Falaras P. & Silva A.M.T. Pore structure, interface properties and photocatalytic efficiency of hydration/dehydration derived TiO_2/CNT composites, Appl. Catal. B: Environ. 147 (2014) 65–81.
40. Cao T., Li Y., Wang C., Shao C. & Liu Y. A facile in situ hydrothermal method to $SrTiO_3/TiO_2$ nanofiber heterostructures with high photocatalytic activity. Langmuir. (2011); 27, 6, 2946-2952.
41. Maletic´ M., Vukcˇevic´ M., Kalijadis A., Jankovic´-Cˇastvan I., Dapcˇevic´ A., Lausˇevic´ Z. & Lausˇevic´ M. Hydrothermal synthesis of TiO_2/carbon composites and their application for removal of organic pollutants. Arabian Journal of Chemistry (2019); 12, 4388–4397.
42. Karkare M.M. Choice of precursor not affecting the size of anatase TiO_2 nanoparticles but affecting morphology under broader view. Int Nano Lett. (2014); 4(3).
43. Pan J.H., Cai Z., Yu Y. & Zhao X.S. Controllable synthesis of mesoporous F-TiO_2 spheres for effective photocatalysis. J Mater Chem. (2011); 21(30):11430-11438.
44. MiarAlipour S., Friedmann D., Scott J. & Amal R. TiO_2/porous adsorbents: Recent advances and novel applications. J Hazard Mater. (2018); 341.

45. Shayegan Z., Lee C.-S. & Haghighat F. TiO_2 photocatalyst for removal of volatile organic compounds in gas phase – A review. Chem Eng J. (2018); 334.
46. Velasco L.F., Haro M., Parmentier J., Gadiou R., Vix-Guterl C. & Ania C.O. Tuning the Photocatalytic Activity and Optical Properties of Mesoporous TiO_2 Spheres by a Carbon Scaffold . J Catal. (2012); 1-9.
47. Budiartia H.A., Puspitasaria R.N., Hattaa A.M., Sekartedjoa & Risantia D.D. Synthesis and Characterization of TiO_2@SiO_2 and SiO_2@TiO_2 Core-Shell Structure Using Lapindo Mud Extract via Sol-Gel Method. Procedia Engineering 170 (2017); 65 – 71.
48. Zhang G., Ding X., Hu Y., Huang B., Zhang X., Qin X., Zhou J. & Xie J. Photocatalytic Degradation of 4BS Dye by N, S-Codoped TiO_2 Pillared Montmorillonite Photocatalysts under Visible-Light Irradiation. J. Phys. Chem. C (2008); 112, 17994–17997.
49. Ao Y., Xu J., Fu D. & Yuan C. A simple method to prepare N-doped titania hollow spheres with high photocatalytic activity under visible light. Journal of Hazardous Materials 167 (2009); 413–417.
50. Li T., Liu S., Zhang H., Wang E., Song L. & Wang P. J. Ultraviolet upconversion luminescence and its application in photocatalysis. Mater. Sci. (2011); 46, 2882-2886.
51. Chen H., Shen M., Chen R., Dai K. & Peng T. Photocatalytic degradation of commercial methyl parathion in aqueous suspension containing La-doped TiO_2 nanoparticles. Environ Technol. (2011); 32(13):1515-1522.
52. Cong Y., Li Z., Zhang Y., Wang Q. & Xu Q. Synthesis of α-Fe2O3/TiO2 nanotube arrays for photoelectro-Fenton degradation of phenol. Chemical Engineering Journal (2012); 111(19), 356–363.
53. Paraknowitsch J.P. & Thomas A. Doping carbons beyond nitrogen: An overview of advanced heteroatom doped carbons with boron, sulfur and phosphorus for energy applications. Energy Environ Sci. (2013); 6(10):2839-2855.
54. Hlekelele L. Synthesis and characterization of TiO_2 and TiO_2 based quaternary mixed metal oxides supported on carbon and fly ash-based materials. Thesis (University of the Witwatersrand, Johannesburg, 2016).
55. Dlamini M.W. Spherical carbons as model supports for Fe, Co and Fe-Co Fischer-Tropsch catalysts. Thesis (University of the Witwatersrand, Johannesburg, 2016).

56. Cong Y., Zhang J., Chen F. & Anpo M. Synthesis and characterization of nitrogen-doped TiO_2 nanophotocatalyst with high visible light activity. J Phys Chem C. (2007); 111(19):6976-6982.
57. Ao Y., Xu J., Zhang S. & Fu D. A one-pot method to prepare N-doped titania hollow spheres with high photocatalytic activity under visible light. Appl Surf Sci. (2010); 256(9):2754-2758.
58. Manikai S.M. the Synthesis of Nitrogen Doped Carbon Spheres as Supports for Palladium Catalysts in the Hydrogenation of cinnamaldehyde. Thesis (University of the Witwatersrand, Johannesburg, 2015).
59. Di Valentin C., Pacchioni G. & Selloni A. Theory of Carbon Doping of Titanium Dioxide. Chem. Mater. (2005); 17, 6656-6665.
60. McKee G.S.B. & Vecchio K.S. Thermogravimetric analysis of synthesis variation effects on CVD generated multiwalled carbon nanotubes. J Phys Chem B. (2006); 110(3):1179-1186.
61. Ndungu P., Nechaev A., Titinchi S., Petrik L. & Hintsho N. Photo-catalytic activity of titanium dioxide carbon nanotube nano-composites modified with silver and palladium nanoparticles. Appl Catal B Environ. (2014); 156-157:273-283.
62. Wang Q., Shang J., Song H., Zhu T., Ye J., Zhao F., Li J. & He S. Visible-light photoelectrocatalytic degradation of rhodamine B over planar devices using a multi-walled carbon Nanotube-TiO 2 composite. Mater Sci Semicond Process. (2013); 16(2):480-484.
63. Natarajan T.S., Lee J.Y., Bajaj H.C., Jo W.-K. & Tayade R.J. Synthesis of multiwall carbon nanotubes/TiO_2 nanotube composites with enhanced photocatalytic decomposition efficiency, Catal. (2017); 282, 13–23.
64. Puma G.L., Li Z., Gao B., Chen G.Z., Mokaya R. & Sotiropoulos S. Carbon nanotube/titanium dioxide (CNT/TiO_2) core-shell nanocomposites with tailored shell thickness, CNT content and photocatalytic/photoelectrocatalytic properties. Appl Catal B Environ. (2011); 110:50-57.
65. Ceragioli1 H.J., Peterlevitz A.C., Quispe J.C.R., Larena A., Pasquetto M.P., Sampaio M.A. & Baranauskas V. Synthesis and characterization of boron-doped carbon nanotubes. Journal of Physics: (2008); 052029.

66. Shaban M., Ashraf A. M. & Abukhadra M.R.TiO_2 Nanoribbons/Carbon Nanotubes Composite with Enhanced Photocatalytic Activity; Fabrication, Characterization, and Application. Scientific reports (2018); 8:781.
67. Perera S.D., Mariano R.G., Vu K., Nour N., Seitz O., Chabal Y. & Balkus K.J. Hydrothermal Synthesis of Graphene-TiO_2 Nanotube Composites with Enhanced Photocatalytic Activity. ACS Catal. (2012); 2(6):949-956.
68. Wang Y., Wang X. & Antonietti M. Polymeric graphitic carbon nitride as a heterogeneous organocatalyst: From photochemistry to multipurpose catalysis to sustainable chemistry. Angew Chemie - Int Ed. (2012); 51(1):68-89.
69. Araña J., Doña-Rodríguez J.M., Rendón T.E., Cabo G.C., Gonzalez-Diaz O., Herrera-Melian J.A., Perez-Pena J., Colon G. & Navio J.A. TiO_2 activation by using activated carbon as a support: Part II. Photoreactivity and FTIR study. Appl Catal B Environ. (2003); 44(2):153-160.
70. Novoselov K.S., Geim A.K., Morozov S.V., Jiang D., Zhang Y., Dubonos S.V., Grigorieva I.V. & Firsov A.A. Electric field effect in atomically thin carbon films, Science 306 (2004); 666–669.
71. Rao C.N.R., Sood A.K., Subrahmanyam K.S. & Govindaraj A. Graphene: the new two-dimensional nanomaterial, Angew. Chem. Int. Ed. 48 (2009); 7752–7777.
72. Ahmadkhaniha R., Izadpanah F. & Rastkari N. Reduced graphene oxide-TiO_2 nanocomposite facilitated visible light photodegradation of gaseous toluene, J. Environ. Prot. 8 (2017); 591–602.
73. Tan L.-L., Chai S.-P. & Mohamed A.R. Synthesis and applications of graphene-based TiO_2 photocatalysts. ChemSusChem. (2012); 5(10):1868-1882.
74. Sun S.M. Studies on Photo-Catalysis Degradation of Rhodamine B Using Titanium Dioxide - Carbon Composite Materials. Adv Mater Res. (2012); 485:161-164.
75. Toyoda M., Nanbu Y., Kito T., Hirano M. & Inagaki M. Preparation and performance of anatase-loaded porous carbons for water purification. Desalination. (2003); 159(3):273-282.
76. Shi J.-W., Zong X., Wu X., Cui H.-J., Xu B., Wang L.& Fu M.-L. Carbon-doped Titania Hollow Spheres with Tunable Hierarchical Macroporous Channels and Enhanced Visible Light-induced Photocatalytic Activity. ChemCatChem (2012); 4, 488 – 491.

77. Khalid N.R., Majid A., Tahir M.B., Niaz N.A. & Khalid S. Carbonaceous-TiO_2 nanomaterials for photocatalytic degradation of pollutants: A review. Ceram Int. (2017); 43 (17):14552-14571.
78. Tayade R.J., Natarajan S.T. & Bajaj H.C. Photocatalytic Degradation of Methylene Blue Dye Using Ultraviolet Light Emitting Diodes. Ind. Eng. Chem. Res. (2009); 48, 10262–10267.
79. Xu R., Li J., Wang J., Wang X., Liu B., Wang B., Luan X. & Zhang X. Photocatalytic degradation of organic dyes under solar light irradiation combined with Er^{3+}:$YAlO_3$/Fe- and Co-doped TiO_2 coated composites. Solar Energy Materials & Solar Cells 94 (2010); 1157–1165.
80. Ong W.-J., Gui M.M., Chai S.-P. & Mohamed A.R. Direct growth of carbon nanotubes on Ni/TiO_2 as next generation for photoreduction of CO_2 to methane by water under visible light irradiation. RSC Adv. (2013); 3, 4505.
81. Gui M.M., Tan L.-L., Ong W.-J., Chai S.-P. & Mohamed A.R. CO_2 photocatalytic reduction: photocatalyst choice and product selectivity. Chem. Commun. (2015); 51, 858.
82. Zhu S. & Wang D. Photocatalysis: Basic Principles, Diverse Forms of Implementations and Emerging Scientific Opportunities. Adv. Energy Mater. (2017); 7, 1700841.
83. Davis R.J., Gainer J.L., Neal G.O. & Wenwu I. Photocatalytic decolorization of wastewater dyes. Water EnViron. Res. (1994); 66, 50–63.
84. Matthews R.W. Photocatalytic oxidation and adsorption of methylene blue on thin films of near-ultraviolet-illuminated TiO_2. J. Chem.Soc., Faraday Trans. (1989); 85, 1291–1302.
85. Deshmukh A.A., Mhlanga S.D. & Coville N.J. Carbon spheres. Mater Sci Eng R 70 (2010); 70(1-2):1-28.
86. Dresselhaus M.S., Villalpando-Paez F., Samsonidze G.G., Chou S.G., Dresselhaus G., Jiang J., Saito R., Filho A.G.S., Jorio A., Endo M. Kim Y.-A. Raman scattering from one-dimensional carbon systems. Phys E Low-Dimensional Syst Nanostructures. (2007); 37(1-2):81-87.
87. Wissler M. Graphite and carbon powders for electrochemical applications. J Power Sources. (2006); 156(2):142-150.

88. Miao J.-Y., Hwang D.W., Narasimhulu K.V., Lin P.-I., Chen Y.-T., Lin S.-H. & Hwang L.-P. Synthesis and properties of carbon nanospheres grown by CVD using Kaolin supported transition metal catalysts. Carbon N Y. (2004); 42(4):813-822.
89. Sun X. & Li Y. Colloidal Carbon Spheres and Their Core/Shell Structures with Noble-Metal Nanoparticles. Angew Chemie - Int Ed. (2004); 43(5):597-601
90. Liu J., Wickramaratne N.P., Qiao S.Z. & Jaroniec M. Molecular-based design and emerging applications of nanoporous carbon spheres. Nat Mater. (2015); 14(8):763-774.
91. Coville N.J., Mhlanga S.D., Nxumalo E.N. & Shaikjee A. A review of shaped carbon nanomaterials. S Afr J Sci. (2011); 107(3/4):1-15.
92. Tetana Z.N. Boron and nitrogen doped carbons for photochemical degradation reactions. Thesis (University of the Witwatersrand, Johannesburg, 2013).
93. Toit J. Hollow Carbon Nanospheres: A Structural Integrity Investigation. MSc Dissertation (University of Stellenbosch, 2018).
94. Li S., Li F., Wang J., Tian L., Zhang H. & Zhang S. Preparation of Hierarchically Porous Graphitic Carbon Spheres and Their Applications in Supercapacitors and Dye Adsorption. Nanomaterials. (2018); 8(8):625.
95. Xiong H., Moyo M., Motchelaho M.A., Tetana Z.N. & Dube S.M.A., Jewell L.L. & Coville N.J. Fischer–Tropsch synthesis: Iron catalysts supported on N-doped carbon spheres prepared by chemical vapor deposition and hydrothermal approaches. Journal of Catalysis (2014); 311: 80–87.
96. Zhang Y., Yang W., Luo R.Y. & Shang H.D. Preparation of carbon nanospheres by non-catalytic chemical vapor deposition and their formation mechanism. New Carbon Mater. (2016); 31(5):467-474.
97. Faisal A.D. & Aljubouri A.A. Synthesis and Production of Carbon Nanospheres Using Noncatalytic CVD Method. Int J Adv Mater Res. (2016); 2(5):86-91.
98. Tian F. & He C.N. Fabrication and growth mechanism of carbon nanospheres by chemical vapor deposition. Mater Chem Phys. (2010); 123(2-3):351-355.
99. Mhlanga S.D., Coville N.J., Iyuke S.E., Afolabi A.S., Abdulkareem A.S. & Kunjuzwa N. Controlled syntheses of carbon spheres in a swirled floating catalytic chemical vapour deposition vertical reactor. J Exp Nanosci. (2010); 5(1):40-51.

100. Serp P. & Figueiredo J.L. Carbon materials for catalysis: Catalytic properties of N-containing carbons (Chapter 7.): Wiley; 1st ed. (2009); 219-257.
101. Zhang C. & Zhou B. Highly dispersible carbon nanospheres in a polar solvent and methods for making same. Headwaters Technology Innovation Group Inc, (2010); 7,666,915.
102. Wickramaratne N.P. & Jaroniec M. Activated carbon spheres for CO_2 adsorption. ACS Appl Mater Interfaces. (2013); 5(5):1849-1855.
103. Sakthivel S. & Kisch H. Daylight Photocatalysis by Carbon-Modified Titanium Dioxide. Angew Chemie - Int Ed. (2003); 42(40):4908-4911.
104. Zhang X., Sun Y., Cui X. & Jiang Z. Carbon-incorporated TiO_2 microspheres: Facile flame assisted hydrolysis of tetrabutyl orthotitanate and photocatalytic hydrogen production. Int J Hydrogen Energy. (2012); 37(2):1356-1365.
105. Chizari K. & Sundararaj U. The effects of catalyst on the morphology and physicochemical properties of nitrogen-doped carbon nanotubes. Mater Lett. (2014); 116:289-292.
106. Ewels C.P. & Glerup M. Nitrogen Doping in Carbon Nanotubes. J Nanosci Nanotechnol. (2005); 5(9):1345-1363.
107. Shao Y., Sui J., Yin G. & Gao Y. Nitrogen-doped carbon nanostructures and their composites as catalytic materials for proton exchange membrane fuel cell. Appl Catal B Environ. (2008); 79(1):89-99.
108. Cao Z., Zhang J., Ding Y., Li Y., Shi M., Yue H., Qiao Y., Yin Y. & Yang S. In situ synthesis of flexible elastic N-doped carbon foam as a carbon current collector and interlayer for high-performance lithium sulfur batteries. J Mater Chem A. (2016);4(22).
109. Xiong H., Moyo M., Rayner M.K., Jewell L.L., Billing D.G. & Coville N.J. Autoreduction and Catalytic Performance of a Cobalt Fischer-Tropsch Synthesis Catalyst Supported on Nitrogen-Doped Carbon Spheres. ChemCatChem. (2010); 2(5):514-518.
110. Deshmukh A.A., Islam R.U.I., Witcomb M.J., van Otterlo W.A.L. & Coville N.J. Catalytic activity of metal nanoparticles supported on nitrogen-doped carbon spheres. ChemCatChem. (2010); 2(1):51-54.
111. Ranganathan K., Morais A., Nongwe I., Longo C., Nogueira A.F. & Coville N.J. Study of photoelectrochemical water splitting using composite films based on TiO_2 nanoparticles

and nitrogen or boron doped hollow carbon spheres as photoanodes. J Mol Catal A Chem. (2016); 422:165-174.

112. Pei F., An T., Zang J., Zhao X., Fang X., Zheng M., Dong Q. & Zheng N. From Hollow Carbon Spheres to N-Doped Hollow Porous Carbon Bowls: Rational Design of Hollow Carbon Host for Li-S Batteries. Adv. Energy Mater. (2016); 6, 1502539.
113. Yan D., Yu C., Zhang X., Qin W., Lu T., Hu B., Li H. & Pan L. Nitrogen-doped carbon microspheres derived from oatmeal as high capacity and superior long life anode material for sodium ion battery. Electrochim Acta. (2016); 191:385-391.
114. Zhou X., Yang Z., Nie H., Yao Z., Zhang L. & Huang S. Catalyst-free growth of large-scale nitrogen-doped carbon spheres as efficient electrocatalysts for oxygen reduction in alkaline medium. J Power Sources. (2011); 196(23):9970-9974.
115. Mondal K.C., Coville N.J., Witcomb M.J., Tejral G. & Havel J. Boron mediated synthesis of multiwalled carbon nanotubes by chemical vapor deposition. Chem Phys Lett. (2007); 437(1-3):87-91.
116. Fathalian A., Dou S.X. & Moradian R. Boron doping effects on the electronic structure of normal and superconductor carbon nanotubes. Phys B Condens Matter. (2010); 405(4):1125-1129.
117. Wang Y., Li H., Yao J., Wang X. & Antonietti M. Synthesis of boron doped polymeric carbon nitride solids and their use as metal-free catalysts for aliphatic C-H bond oxidation. Chem Sci. (2011); 2(3):446-450.
118. Zhang B., Qin X., Li G. R. & Gao X. P. Enhancement of long stability of sulfur cathode by encapsulating sulfur into micropores of carbon spheres. Energy Environ Sci. (2010); 3(10):1531-1537.
119. Sun Y., Wu J., Tian J., Jin C. & Yang R. Sulfur-doped carbon spheres as efficient metal-free electrocatalysts for oxygen reduction reaction. Electrochim Acta. (2015); 178:806-812.
120. Wu J., Jin C., Yang Z., Tian J. & Yang R. Synthesis of phosphorus-doped carbon hollow spheres as efficient metal-free electrocatalysts for oxygen reduction. Carbon 82 (2015); 562–571.

121. Zhang C., Hou L., Cheng C., Zhuang Z., Zheng F. & Chen W. Nitrogen and Phosphorus Co-doped Hollow Carbon Spheres as Efficient Metal-Free Electrocatalysts for the Oxygen Reduction Reaction. ChemElectroChem. (2018); 5(14):1891-1898.

122. Yu Y.-N., Wang M.-Q. & Bao S.-J. Biomass-derived synthesis of nitrogen and phosphorus Co-doped mesoporous carbon spheres as catalysts for oxygen reduction reaction. J Solid State Electrochem (2017); 21:103–110.

123. Liu Z., Nie H., Yang Z., Zhang J., Jin Z., Lu Y., Xiao Z. & Huang S. Sulfur-nitrogen co-doped three-dimensional carbon foams with hierarchical pore structures as efficient metal-free electrocatalysts for oxygen reduction reactions. Nanoscale. (2013); 5(8):3283-3288.

124. Bepete G., Voiry D., Chhowalla M., Chiguvare Z. & Coville N.J. Incorporation of small BN domains in graphene during CVD using methane, boric acid and nitrogen gas. Nanoscale. (2013); 5(14):6552-6557.

125. Phaahlamohlaka T.N. Synthesis of carbon nanofibers and their subsequent use as catalyst supports for Fischer-Tropsch synthesis. MSc Dissertation (University of the Witwatersrand, Johannesburg, 2013).

126. Osorio A.G., Silveira I.C.L., Bueno V.L. & Bergmann C.P. H_2SO_4/HNO_3/HCl-Functionalization and its effect on dispersion of carbon nanotubes in aqueous media. Applied Surface Science 255 (2008); 2485–2489.

127. Jin Y.Z., Gao C., Kroto H.W. & Maekawa T. Polymer-Grafted Carbon Spheres by Surface-Initiated Atom Transfer Radical Polymerization. Macromol. Rapid Commun. (2005); 26, 1133–1139.

128. Du D., Zou Z., Shin Y., Wang J., Wu H., Engelhard M.H., Liu J., Aksay I.A. & Lin Y. Sensitive Immunosensor for Cancer Biomarker Based on Dual Signal Amplification Strategy of Graphene Sheets and Multienzyme Functionalized Carbon Nanospheres. Anal. Chem. (2010); 82, 2989–2995.

129. Sekhar C., Ray S. C., Tetana Z. N., Erasmus R., Mathur A. & Coville N. J. Carbon spheres for energy applications: Raman and X-ray photoemission spectroscopy studies. Int. J. Energy Res. (2014); 38:444–451.

130. Yahya M.A., Al-Qodah Z. & Ngah C.W.Z. Agricultural bio-waste materials as potential sustainable precursors used for activated carbon production: A review. Renew Sustain Energy Rev. (2015); 46:218-235.

131. Yang S., Mao X., Cao Z., Yin Y., Wang Z., Shi M. & Dong H. Onion-derived N, S self-doped carbon materials as highly efficient metal-free electrocatalysts for the oxygen reduction reaction. Appl Surf Sci. (2018); 427:626-634.
132. Ratchahat S., Viriya-Empikul N., Faungnawakij K., Charinpanitkul T. & Soottitantawat A. Synthesis of Carbon Microspheres from Starch by Hydrothermal Process. Sci J UBU. (2010); 1(2):40-45
133. Mongwe T.H., Matsoso B.J., Mutuma B.K., Coville N.J. & Maubane M.S. Synthesis of chain-like carbon nano-onions by a flame assisted pyrolysis technique using different collecting plates. Diam Relat Mater. (2018); 90:135-143.
134. Liu D., Zhang W., Lin H., Li Y., Lu H. & Wang Y. A green technology for the preparation of high capacitance rice husk-based activated carbon. J Clean Prod. (2016); 112:1190-1198.
135. Huang Y., Ma E. & Zhao G. Thermal and structure analysis on reaction mechanisms during the preparation of activated carbon fibers by KOH activation from liquefied wood-based fibers. Ind Crops Prod. (2015); 69:447-455.
136. Lozano-Castelló D., Lillo-Ródenas M.A., Cazorla-Amorós D. & Linares-Solano A. Preparation of activated carbons from Spanish anthracite - I. Activation by KOH. Carbon. (2001); 39:741–749.
137. Lillo-Ródenas M.A., Lozano-Castelló D., Cazorla-Amorós D. & Linares-Solano A. Preparation of activated carbons from Spanish anthracite - II. Activation by NaOH. Carbon. (2001); 39:751-759.
138. Caturla F., Molina-Sabio M. & Rodr´ıguez-Reinoso F. Carbon (1991); 29(7):999–1007.
139. Rodr´ıguez Reinoso F. & Molina-Sabio M. Carbon (1992); 30(7):1111–8).

CHAPTER 3: CHARACTERISATION TECHNIQUES

3.1 Introduction

Experimental methodology and characterization techniques are of paramount importance in understanding the structural morphology and behavior of the as-prepared products. In this chapter, the focus is on the characterization techniques that were used, the emphasis is on the fundamental principle behind each chosen technique. Experimental methods will be reported in the following chapters with more details being explained in the results.

3.1.1 Transmission Electron Microscopy (TEM)

TEM was used to characterize the solid material; studying the structure, morphology, and size to examine the defects and to determine the distribution of elements in the material. Average particle size was also obtained, and in most cases, a histogram is plotted demonstrating the distribution of the materials' particles. TEM is very dependent on the preparation of the material as very thin sample films are required, as a result, the prepared material followed a well-known type of experimental procedure. The samples were prepared by taking a small portion of the material (*ca*. 5 mg), dispersed in ethanol then ultra-sonicated to allow further dispersion. A copper grid was used to disperse the suspension. Images were then taken using the FEI G^2 SPIRIT TECNAI T12 TEM instrument at an accelerating voltage of 120 kV.

3.1.2 Scanning Electron Microscopy (SEM)

The FEI Nova Nanolab 600 FIB scanning electron microscope (30 kV) was used to study the morphology of the prepared samples with their surface qualities. Approximately 5 mg of the solid material was prepared on the aluminum stub, coated with double-sided carbon tape to make the material stick onto the stub. Coating in most instances is done to minimize surface charging, the samples were coated with carbon and gold/palladium alloy by using a sputter coater. The sample holder was then loaded into the microscope stage.

3.1.3 CHNS elemental analysis

CHNS elemental analyzer obtains information about the presence of carbon, hydrogen, nitrogen, and sulfur in the carbon material. It can be used for a variety of sample types, which include solids, liquids, volatile and viscous samples. A high temperature is required for combustion of an environment with oxygen which can be carried out under two conditions, i) static condition where different types of volumes are introduced based on the oxygen present and ii) dynamic condition only a constant volume of oxygen is applied depending on the amount needed [1]. This is a bulk technique, which offers information on the total elements in the sample. In this study, the total quantification of N, S, C, and H elements present in NSCS material was obtained.

3.1.4 Powder X-ray diffraction (PXRD)

To confirm the crystallinity, interlayer spacing, structural strain, and impurities in the synthesized NSCS and the TiO_2_NSCS composites, PXRD analysis was carried out. In this method, the arrangement of the atom particles in the instrument is very important as the diffraction pattern that will be obtained will be used to determine the differences in the samples analyzed [1]. To do this, a Bruker D2 phaser equipped with Co K alpha radiation (30 kV, 10 mA) was used. The following variables were kept constant throughout the analysis; 2θ at 10-90° with a scan step mode of 0.026°. A zero-background sample holder was used to mount the solid powdered samples. The average crystallite size of TiO_2 and TiO_2_NSCS composites was obtained by Debye Scherer's equation using the (101) reflection.

$$D_{hkl} = \frac{K \times \lambda}{\beta \times cos\ \theta} \quad \text{.....eq. 3.1}$$

Where D_{hkl} is the crystallite size, K is a factor of the instrument of which in this case 0.9 was used, λ - the X-ray wavelength, β- is the full-width half-maximum in radians and θ is the Bragg angle [1].

3.1.5 Laser Raman spectroscopy

Raman spectroscopy is a non-destructive and very effective method that can be used for the characterization of the detailed bonding structure of carbon nanomaterials. Raman spectroscopy was advantageous in distinguishing the chemical properties; crystallinity, strain, and symmetries of the molecule, which mainly focuses on the change from sp^2 to sp^3 hybridization [2-4]. In addition, the ratio of the intensity of D/G peaks is a measure of the defects present on the carbon nanomaterials structure. The measurements for the synthesized materials were done using a Bruker Raman Senterra spectrometer where the laser was excited at 532 nm.

3.1.6 Fourier Transmittance Infrared (FTIR) spectroscopy

FTIR spectroscopy is used for the determination and identification of molecular structures. It can be used for structural analysis of solutions, liquids, vapor phases, and solids [5]. Organic molecules are obtained in the mid-infrared region in ranges of 4000-400 cm^{-1} while inorganic molecules are observed in the far-infrared region in ranges of 400-33 cm^{-1}. In this work, FTIR was used to get an insight into the surface binding of which chemical interaction between the elements occurred [6,7,8]. Bruker TENSOR 27 FT-IR spectrometer was used for the measurements of the solid materials.

3.1.7 X-ray Photoelectron Spectroscopy (XPS)

X-ray photoelectron spectroscopy (XPS) is a surface technique with elemental information obtained on the surface of the material. The ratio of the material can be observed, also the configuration of the heteroatoms that are interacting with the material. Elemental analysis of the surface functional groups on the carbons and the elements present in the composites were done using Physical Electronics Quantum 2000 using a monochromatic Al Kα source (1486.7 eV) and a working pressure of $1.8x10^{-8}$ torr. Quantification of the elements with their atomic percentage was obtained equating to a hundred percent of the analyzed sample. The measurements were performed at NMISA, Pretoria.

3.1.8 Thermogravitational analysis (TGA)

TGA is a technique that is used to monitor the weight change of a sample as it is heated in gas/air, as a function of temperature or time. Detection of mass loss is indicative of the presence of volatile components observed at specific temperature ranges. TGA analysis was carried out to investigate the thermal degradation behavior of NSCS and TiO_2_NSCS composites. For the analysis of the sample, a solid sample of *ca.* 10 mg was placed into a sample pan, the sample was heated using a 10 ℃/ min heating rate with a flow rate of 20 ml/min under N_2 gas. The TGA measurements were done using PerkinElmer Pyris STA6000, from Pyris software.

3.1.9 Brunauer-Emmett-Teller (BET)

BET studies give information about the surface area, pore-volume, and pore size of the material. BET allows for the specificity of surface area, percentage porosity, and pore size distribution at low temperatures (77 K). Adsorption-desorption isotherms of liquid N2 at 77 K for all samples were measured with Micrometrics TriStar 3000 surface area analyzer to obtain hysteresis loop and type of pores present in the material under investigation. In this study, a comparison of the specific surface area of the carbon spheres before being incorporated with TiO_2 was done, confirming the effect of TiO_2 on the carbon porosity. The sample was degassed in nitrogen gas at 150 ℃ for 4 hours before analysis.

3.1.10 UV-Vis spectroscopy

UV-vis spectroscopy is usually set in the wavelength of 200-800 nm, compounds obtained below this range may have to be conducted under vacuum, as the presence of oxygen is undesired. A concentration of the unknown can be plotted to obtain a calibration curve [9]. UV-Vis spectroscopy was used to understand the photodegradation of the TiO_2 when undoped and compared with TiO_2 when supported on NSCS to degrade Rhodamine B dye. The wavelength of Rhodamine B is 553 nm, where an absorption peak will be detected under the solar spectrum. A spectrophotometer with a tungsten halogen light source was used with measurements taken between 200-800 nm.

3.2 Photocatalytic degradation

In photocatalytic degradation, three steps are imperative, 1) dye adsorption 2) absorption of light by the catalyst and 3) charge-transfer reactions for radicals' generation. As light is irradiated, electrons (e^-) move from the valence band to the conduction band leaving behind a positive hole (h^+). The positive hole reacts with an electron donor such as H_2O forming hydroxyl ($^{\cdot}OH$) radicals, which are responsible for dye degradation. Degradation of organic pollutants has been said to occur on the surface of the TiO_2 semiconductor, not in the solution of the bulk [10]. Consequently, the expected interaction of TiO_2_NSCS catalyst with RhB is expected to occur on the surface of the catalyst. It is noteworthy that dyes in the aqueous suspension photodegrade form non-toxic minerals, while in the presence of a catalyst convert to cationic dye radicals, this was confirmed by HPLC-MS analysis [10,11]. Different masses of photocatalysts were prepared and added to a 50 ml of RhB prepared at different concentrations. The suspensions were magnetically stirred in the dark for 2 hours. This was done to ensure that the suspension reached adsorption-desorption equilibrium. 1 ml of the suspension was sampled during the photocatalytic degradation using a syringe fitted in 0.25 μl syringe filter.

The solar simulator resembles the solar spectrum, which includes both UV and IR radiations. A continuous solar simulator uses the Xenon arc lamp that can measure 1000 W/m^2 shown in **Figure 3.1** [1].

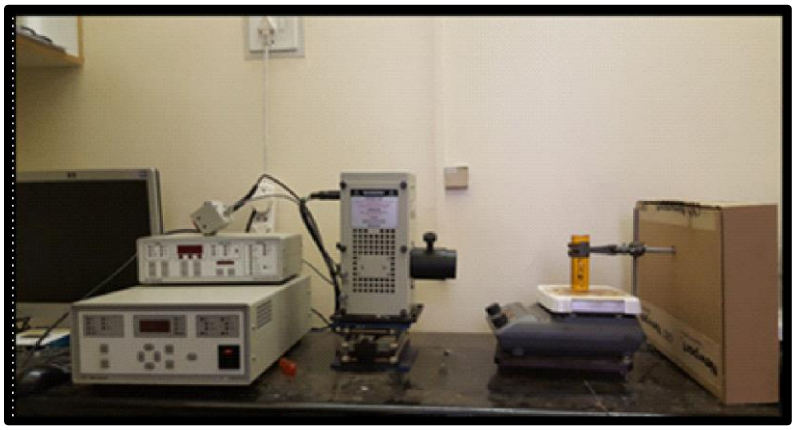

Figure 3.1: Schematic representation of the Newport Illuminator Solar Simulator Oriel Instruments WX00048 [1].

3.2.1 High performance liquid chromatography (HPLC)

HPLC is an analytical technique used to quantify and specify compounds in a molecule. The compound is injected using a syringe and passes through the stationary and the mobile phase of the column [12,13]. The column consists of solid adsorbents of which interact differently with the injected material and results in different flow rates which are then interpreted by the retention time. HPLC determines what is inside the sample and using differential migration components of the sample can be separated. The detector obtains a chromatogram with molecules recorded as a function of separation time [12]. Chromatographic analysis can be used in complex dye molecules to understand their decomposition in the presence of light. RhB degradation and pathway mechanism of degradation were previously studied using HPLC [14,15]. The motivation to use HPLC was to understand the photodegradation of different dye compounds, using a process that goes through a structural breakdown resulting in the production of less toxic compounds [14]. HPLC then was found to quantify the breakage of the compounds. A prominent peak from the chromatogram, which is of the parent, was observed at the beginning of the reaction as irradiation time passes the peak diminishes confirming the breaking down of different molecules in the structure. Interestingly there is a difference in the retention time for the molecules that were broken down [14,15]. The analysis of the sample was performed on a Bruker Compact Q-TOF high resolution Compact mass spectrophotometer. A 10µL of the sample was injected into the UHPLC and run through a loop at 50% Solvent A consisting of 0.1 % formic acid in H2O (v/v) and 50% solvent B consisting of 0.1 % formic acid in Acetonitrile (v/v).

3.2.2 Mass Spectrometry (MS)

Mass spectrometry is an analytical technique used for the identification of quantitation of polyatomic compounds [16,17]. Mostly the compounds used in MS are complex and thus simplification of their molecules is usually of interest. The principle behind MS is the fragmentation of ion sources to various ions, which are determined by the mass-to-charge ratio (m/z) [17]. A mass spectrum is obtained from the detector of which the intense peak is mostly of the parent cation, which is the indication of the abundance of the compound. Fragmentation of the ions with characteristics of the parent ion is observed with time. In dye degradation, mass

spectrometry is used as a post-analyzing technique to understand the photocatalytic mechanism pathway of the compound. In a study conducted by Tayade et al. [18], the photodegradation of RhB was studied and MS was used for the investigation of the mechanism pathway. They observed that the parent cation diminished with time with a distance between peaks being observed, representing the loss of ion fragmentation from the compound [17,18]. Like most techniques, MS can be hyphenated with HPLC, resulting in HPLC-MS improving the efficiency of these two techniques.

HPLC-MS was used to study and understand the principle behind the mechanism degradation pathway of RhB under TiO_2 and TiO_2_NSCS catalysts.

3.3 References

1. Hlekelele L. Synthesis and characterization of TiO_2 and TiO_2 based quaternary mixed metal oxides supported on carbon and fly ash-based materials. Thesis (University of the Witwatersrand, 2016)
2. Deshmukh A.A., Mhlanga S.D. & Coville N.J. Carbon spheres. Mater Sci Eng R 70 (2010); 70(1-2):1-28.
3. Ferrari A.C. & Robertson J. Interpretation of Raman spectra of disordered and amorphous carbon. Phys. Soc. (2000); 14095.
4. Robertson J. Diamond-like amorphous carbon. Mat. Sci and Eng. (2002); 37: 129-281.
5. Araña J., Doña-Rodríguez J.M., Rendón T.E., Cabo G.C., Gonzalez-Diaz O., Herrera-Melian J.A., Perez-Pena J., Colon G. & Navio J.A. TiO_2 activation by using activated carbon as a support: Part II. Photoreactivity and FTIR study. Appl Catal B Environ. (2003); 44(2):153-160.
6. Harvey D. Modern Analytical Chemistry. First edition. Chapter 10. McGraw-Hill. United States of America (2000).
7. Fifield F.W. & Kealey D. Principles and Practice of Analytical Chemistry. Chapters 7 and 9. Fifth Edition. Blackwell Science. UK (2000).
8. Jeffrey G. H., Bassett J., Mendham J. & Denney R. C. Vogel's Textbook of Quantitative Chemical Analysis. Chapter 19. Fifth Edition. UK (1999).
9. Anderson R.J. & Bendell D.J. PW. Groundwater, Organic Spectroscopic Analysis, 1st Edition. The Royal society of Chemistry, United Kingdom (2004) pp 1-10.
10. Zhao J., Wu T., Wu K., Oikawa K., Hidaka H. & Serpone N. Photoassisted Degradation of Dye Pollutants. 3. Degradation of the Cationic Dye Rhodamine B in Aqueous Anionic Surfactant/TiO_2 Dispersions under Visible Light Irradiation: Evidence for the Need of Substrate Adsorption on TiO_2 Particles. Environ. Sci. Technol. (1998); 32, 2394-2400.
11. Ao Y., Xu J., Fu D. & Yuan C. Visible-light responsive C, N-codoped Titania hollow spheres for X-3B dye photodegradation. Microporous and Mesoporous Materials 118 (2009); 382–386.
12. Synder L.R., Kirkland J.J. & Dolan J.W. Introduction to Modern Liquid Chromatography, John Wiley and Sons, United States of America. 3rd Edition, pp 1-27, (2012)

13. Lough W.J. & Wainer I.W. High Perfomance Liquid Chromatography: Fundamental Principles and Practice. Chapman and Hall, United Kingdom. 1st Edition, (1995); 1-34.
14. Rasheed T., Bilal M., Iqbal H.M.N., Hu H. & Zhang X. Reaction Mechanism and Degradation Pathway of Rhodamine 6G by Photocatalytic Treatment. Water Air and Soil Pollution. (2017); 228; 291-101.
15. Rasheed T., Bilal M., Iqbal H.M.N., Shah S.Z.H., Hu H., Zhang X. & Zhou Y. TiO_2/UV-assisted rhodamine B degradation: putative pathway and identification of intermediates by UPLC/MS. Environmental technology. (2018); 12: 1533–1543.
16. Harrison A.G. Chemical ionization mass spectrometry. CRC Press. United Kingdom. 2nd edition. (1992); 1-5.
17. Gross J.H. Mass spectrometry. Springer-Verlag Berlin Heildelberg, Germany. 1st edition. (2004); 1-10.
18. Tayade R.J., Natarajan S.T. & Bajaj H.C. Photocatalytic Degradation of Methylene Blue Dye Using Ultraviolet Light Emitting Diodes. Ind. Eng. Chem. Res. (2009); 48, 10262–10267.

CHAPTER 4: Effects of activating agent and annealing temperature on the preparation of the nitrogen and sulfur co-doped carbon spheres (NSCS) using an onion

4.1 Introduction

Activation of carbon spheres differs depending on the carbon precursor, synthesis method and the application to be studied. Some of the activating agents that have been investigated include phosphoric acid (H_3PO_4), zinc chloride ($ZnCl_2$), potassium hydroxide (KOH), and sodium hydroxide (NaOH) [1-4]. The NSCS material was activated before annealing using the chemical vapor deposition (CVD) method. It has been previously reported that carbon spheres possess properties such as improved porosity, high specific surface area, and large micro-pore volume being altered due to the addition of activating agents [2]. Carbon precursors that are obtained from raw materials are physically mixed with activating agents. This is because natural carbon precursors do not always result in fully developed spherical-shaped carbons. Whereas during the pyrolysis of these raw materials with employed activating agents, obtained carbon spheres are well-ordered and spherical [1].

In studies conducted by Lozano-Castello et al. [1,2], KOH and NaOH activating agents were studied using Spanish anthracite as a natural carbon precursor for the growth of carbon spheres. The raw material was synthesized using the pyrolysis method and they observed that regardless of the type of activating agent used, carbon spheres fully formed [1]. It is well known that activating agents have to go through the washing step after pyrolysis to remove any metal residual and this was also the case with KOH and NaOH activating agents [1,2]. They discovered that acid washing and water washing resulted in similar observations, with water washing being generally used. However, with basic activating agents (KOH, NaOH), large volumes of water are required for the washing step to reach a neutral pH (~ 7) this in turn, affects the yield of the carbon spheres.

In another study by Yang et al. [4], $ZnCl_2$ was used as an activating agent for onion raw material to produce nitrogen and sulfur co-doped carbon spheres for electrocatalysis application. The hydrothermal and pyrolysis methods were applied sequentially, later followed by hydrochloric acid washing step to remove $ZnCl_2$. Conversely, due to the difficulty in removal of the $ZnCl_2$ during the washing process, harsher techniques have been employed, as the use of the hydrochloric

acid [4]. Due to the presence of the common ion, in this study, Yang and colleagues observed minimal dissolution of the $ZnCl_2$ [4]. However, even though $ZnCl_2$ removal was not as significant in other protocols [1-3]. Yang and colleagues observed that the activation process using $ZnCl_2$ was favorable as it promoted the formation of high surface area carbon spheres due to the defects incorporated by the addition of $ZnCl_2$ [4].

Several studies have demonstrated that KOH as an activating agent is mostly preferred due to the low temperatures and reduced time that can be used for the synthesis of activated carbon spheres [5]. However, KOH exhibits some corrosive traits towards aluminum and alloys due to the formation of hydrogen gas. The corrosive nature of KOH is generally observed when exposed to high-temperature synthesis. On the other hand, $ZnCl_2$ was found to be stable and less corrosive when exposed to high synthesis temperatures [1,2]. Therefore, the production of carbon spheres at high temperatures with the use of $ZnCl_2$ as the activating agent was investigated.

Biomass-derived carbon spheres discovery became of interest as they were earlier found to be applicable in paints, inks, resins, batteries, etc. [1-7]. Carbon spheres have interesting properties that attracted many researchers [5,6]. These include chemical stability, flexibility, smooth surface area, controllable pore distribution, and high mechanical strength [1-8]. As a result, the mechanism of the growth of spherical-shaped carbon spheres has been considerably studied due to exposure to high temperature conditions [9]. Equally, carbon spheres produced from different synthesis methods are desirable as they result in the size, diameter, and chemical properties of the spheres being improved. However, van der Waals forces are highly active in the chemical bonding of the C-C bond leading to agglomeration, which has been the major problem concerning the production of carbon spheres [5,9].

Synthetic and natural carbon precursors have been investigated for the production of carbon spheres. For example, Aili et al. [10] reported on the use of acetylene as a carbon precursor to produce carbon spheres using the furnace pyrolysis method [10]. Numerous synthetic carbon precursors have been used such as glucose, polysaccharides, organometallic compounds, etc. for the synthesis of carbon spheres [10]. Of late, natural carbon precursors have been investigated for the production of carbon spheres, as part of biomass development. Zhao et al. [11] investigated the use of potato starch by the use of an autoclave method, followed by carbonization of the material

[11]. While Wang et al. reported the use of sugar as a carbon precursor to produce shaped carbon material [12]. Additionally, the shell of broad beans (SB) has been investigated [13].

The latest quest has been to consider carbon precursors that are relatively cheap, abundant, renewable, and environmentally friendly [11-15]. Conversely, the elemental composition and microstructure of natural materials are of interest as they ensemble the above-mentioned criteria. Carbon spheres (CSs) obtained from onion material follow a green process as surfactants, catalysts, or organic solvents are not used for their production. In this work, a simple yet detailed hydrothermal assisted pyrolysis method was demonstrated for producing nitrogen, sulfur co-doped carbon spheres by using green, renewable, and widespread onion as the carbon precursors.

Since agglomeration has been reported to occur during the pyrolysis process as well as resulting in reduced chemical inertness on the surface of CSs, the functionalization process has been used [16,17]. Functionalization is a technique mostly used for the introduction of functional groups on the surface area of carbon material [16]. Enhancement of carbon spheres' inert surface using different functionalization methods improves compatibility and dissolution properties in the solution [17]. To introduce functional groups on CSs surfaces an acidic solution consisting of nitric acid (HNO_3) and sulphuric acid (H_2SO_4) is normally used [16,17]. The ratio of the acids used usually varies depending on the study being conducted. Also, the introduction of functional groups is believed to improve the distribution of carbon spheres in a solution [16,18-20].

In this study, the focus is on co-doped carbon spheres with nitrogen and sulfur heteroatoms using onion material as the carbon precursor. The advantage of using carbon precursors that already have heteroatom groups within them is that homogeneous distribution of the functional groups within the produced material has been observed [4,7]. In our work, KOH and $ZnCl_2$ activating agents were used for the growth of NSCS using natural onion raw material as the nitrogen, sulfur, and carbon-containing source. **Figure 4.1** illustrates raw and ground onion material with its elemental compositions (C, N, S, O, and H). The NSCS were produced by the hydrothermal method followed by the furnace pyrolysis method in the presence of activating agents; while parameters such as the mass ratio of activating agents to carbon precursor, reaction temperature, and type of washing step condition were evaluated. In this work, NSCS were annealed at various temperatures (850, 900, and 950 ℃), followed by functionalization of the obtained product in acidic media.

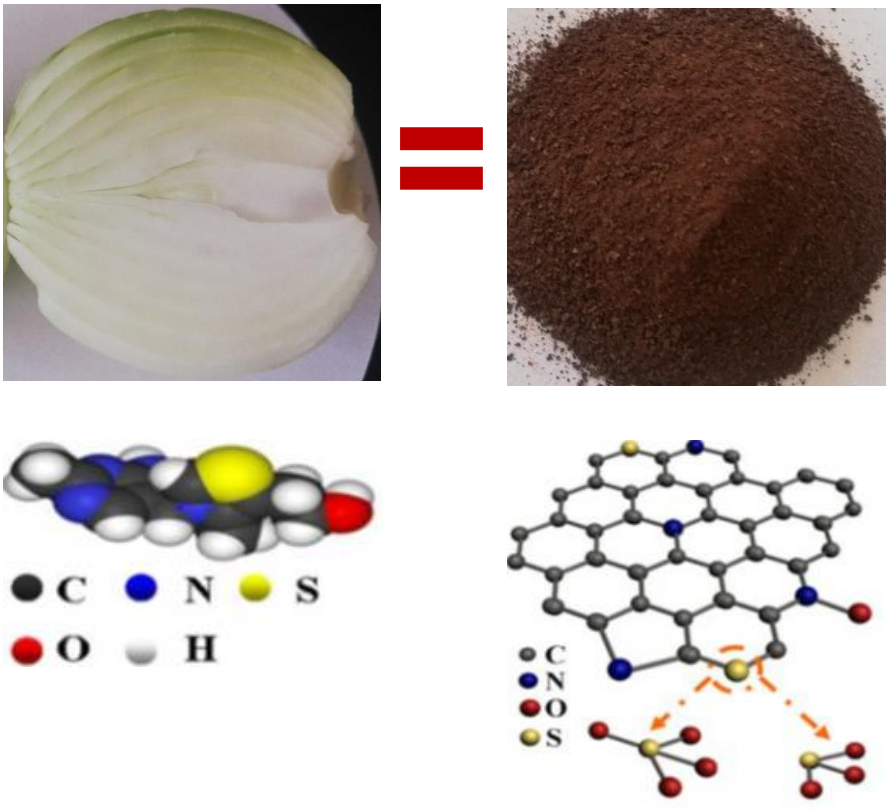

Figure 4.1: Illustration of raw onion before pyrolysis and ground onion after pyrolysis with elemental composition [4].

4.2. Experimental

4.2.1 Effect of activating agents on the growth of NSCS

NSCS was prepared using a modified method copied from the work of Yang and colleagues [4] with a few modifications. Onions used in this study were obtained from the market. The experimental procedure is shown in **Figure 4.2**. Onions were peeled and washed with distilled water before use, and properly dried in an oven at 90 ℃. After sufficient drying, the onion was ground obtaining a brown powder. Subsequently, the ground brown powder was sieved by a 150-micron mesh sieve. The resulting brown powder was later mixed with ammonium bicarbonate NH_4HCO_3 (16 mM) and dispersed in 50 mL distilled water (H_2O). This mixture was sealed in a 60 mL Teflon-equipped stainless steel autoclave reactor. The autoclave was then placed in a muffle furnace with the temperature set to 200 ℃ ramped at 5 ℃ /min and maintained at this temperature for 12 hours. After drying, different ratios (1:2 and 1:3) of KOH and $ZnCl_2$ activating agents were

added to the carbon precursor to obtain pronounced heteroatom carbon spheres; as it was reported that optimizing activating agents for tuneable carbon spheres play a huge role in the making of carbon spheres [4]. Successively, the obtained product was placed in a quartz tube, annealed at 850 °C under the N_2 gas atmosphere for two hours in a horizontal furnace with a heating rate ramped at 5 °C/min. The obtained product was labeled as NSCS while depending on the amount of activating agent used were then denoted as NSCS2 (NSCS2 KOH; NSCS2 $ZnCl_2$) and NSCS3 (NSCS3 KOH; NSCS3 $ZnCl_2$). NSCS without activation was discussed for the material without activating agents, this was done for comparison.

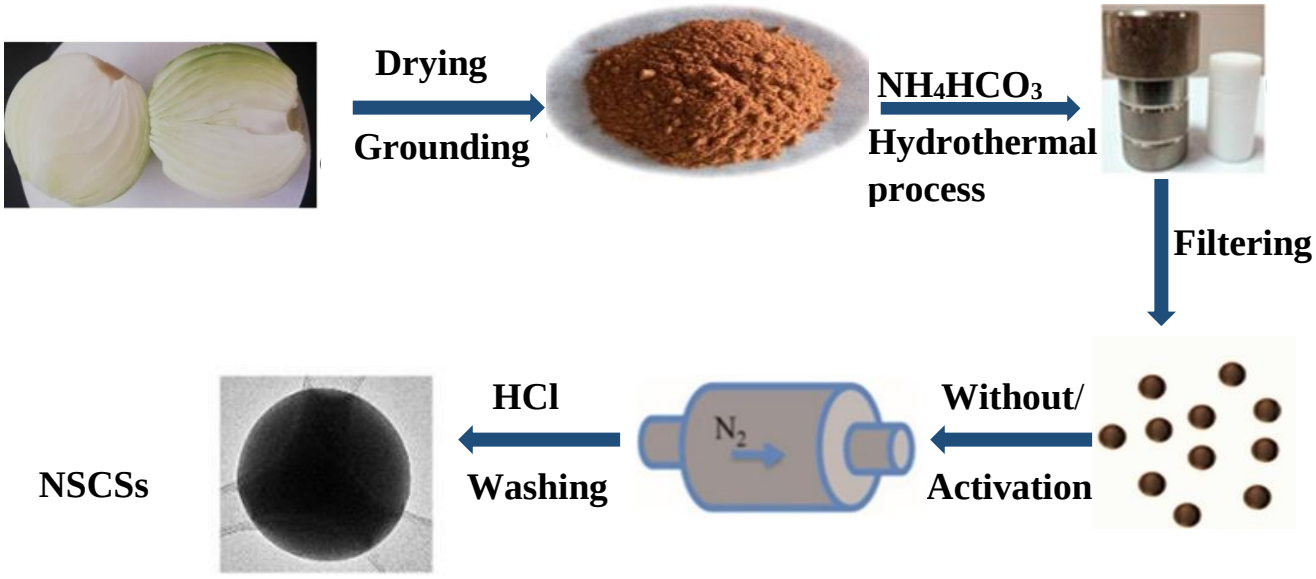

Figure 4.2: Schematic diagram showing the synthesis of NSCS using onion raw material [4].

4.2.2 Effect of the annealing temperature and functionalization on the properties of the NSCS

The results that were obtained from using KOH activating agent were comparable with those where $ZnCl_2$ was used. Nevertheless, the outcome was not completely favorable at high temperatures, this resulted in non-continuation of the KOH activating agent. A similar method as that reported in section **4.1.2** was employed**,** $ZnC1_2$ activating agent being used and annealed at

the following temperatures: 850, 900, and 950 ℃ under N_2 atmosphere for two hours in a horizontal furnace with a heating rate of 5 °C/min. The obtained products were also labeled as NSCS without activation, while depending on the synthesis temperature were then denoted as NSCS2 $ZnCl_2$ @ 850 °C, NSCS2 $ZnCl_2$ @ 900 °C, and NSCS2 $ZnCl_2$ @ 950 °C, respectively.

After NSCS was synthesized via the CVD method, approximately 1 g of the material was dispersed in an acidic mixture of HNO_3 and H_2SO_4 where different volume ratios were used. Under fume-hood, a 250 mL round bottom flask with the suspension was placed in an oil bath and heated at 110 ℃ for 3 hours. The mixture was then left to cool down to room temperature and was later refluxed until all the solvents were evaporated under rotary evaporation at 70 ℃. Due to the acidity of the solution that was used, the obtained product was filtered using a large volume of distilled H_2O until a neutral pH (~7) was reached. This was done to avoid any residual of the acidic solution in the material before its application. The sample was dried in an oven at 60 ℃ overnight.

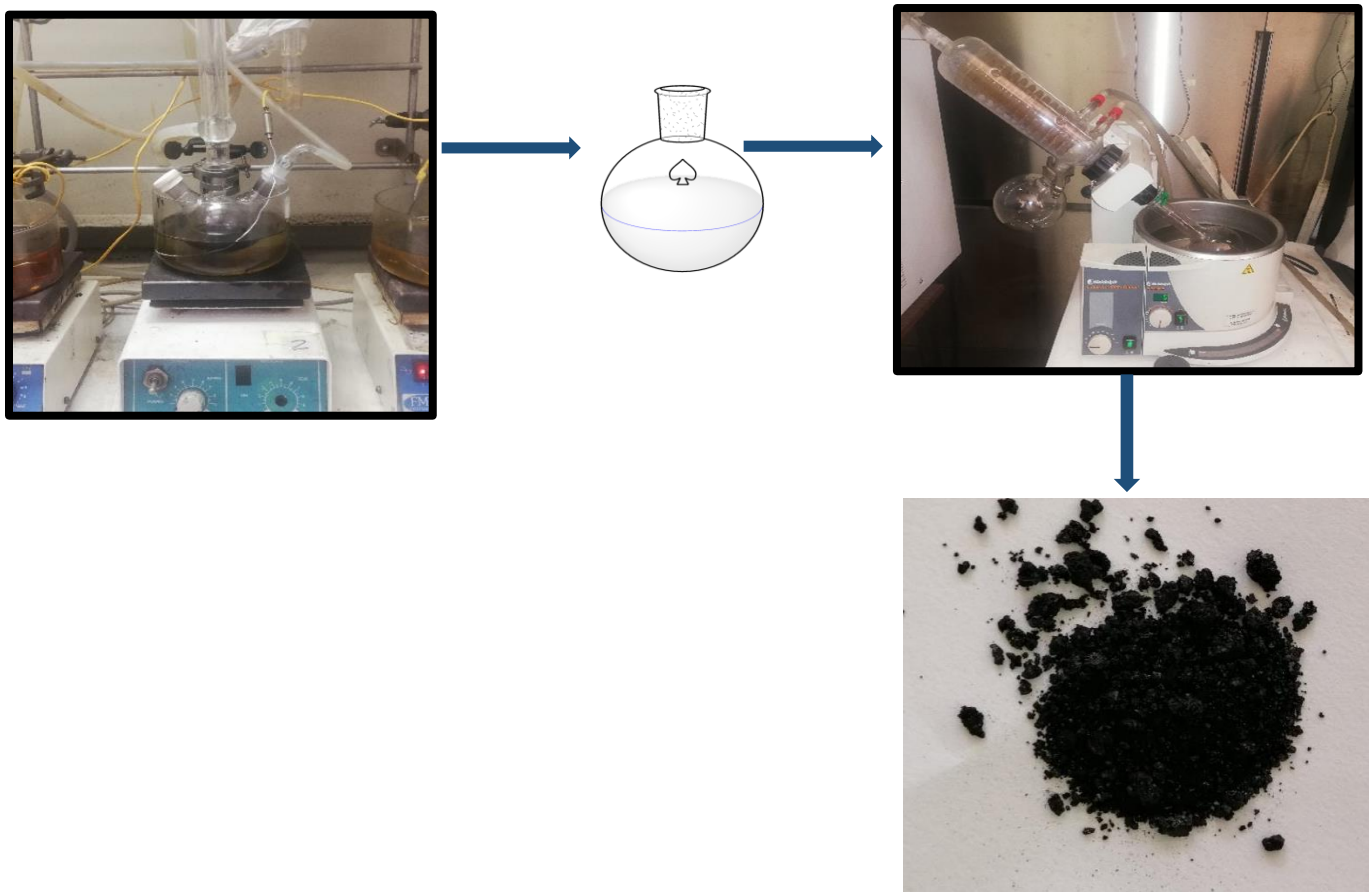

Figure 4.3: Experimental set-up of functionalization of NSCS nanoparticles using HNO_3 and H_2SO_4 acid solution.

4.3 Results and Discussion

4.3.1 Effect of activating agents on the growth of the NSCS

4.3.1.1 TEM analysis of the NSCS

TEM was used for the elucidation of the morphology, size, and structural features of the carbon materials. The effect of activation was investigated with a mass ratio of 2:1 and 3:1 $ZnCl_2$ and KOH raw material with a constant temperature of 850 ℃. **Figure 4.4** are the TEM images of the produced materials. As can be seen from **Figure 4.4** (**a**)**,** there is a presence of agglomerated solid material without a defined shape. This was attributed to the carbon precursor that was used, in this case, the onion raw material without the addition of the activating agents in the material. In the presence of activating agents, controllable and fully spherical-shaped NSCS was observed. In **Figure 4.4** (**b**) and (**d**)**,** where KOH was used for activation, there was a more uniform dispersion of the NSCS in both mass ratios (1:2 and 1:3). Whereas **Figure 4.4** (**c**) and (**e**) are images where $ZnCl_2$ activation was used, the spheres were more agglomerated. This was attributed to the material going under carbonization, which breaks down carbon atoms into radicals then binds together as chain-like carbon materials [3,5,8,20]. In an attempt to separate the connected carbon spheres, the product was ultra-sonicated for over 5 hours to improve the interconnection of the carbon material. However, there was no improvement observed, agreeing with most reports in the literature [19,21]. The particle diameter of the as-synthesized NSCS were 58, 76, 62, and 128 nm for the NSCS2 KOH, NSCS2 $ZnCl_2$, NSCS3 KOH, and NSCS3 $ZnCl_2$, respectively. The samples with $ZnCl_2$ activating agent have a slightly larger particle size while particle size distribution is similar. Whereas the samples with KOH activating agent it was observed that the nanoparticles were highly distributed.

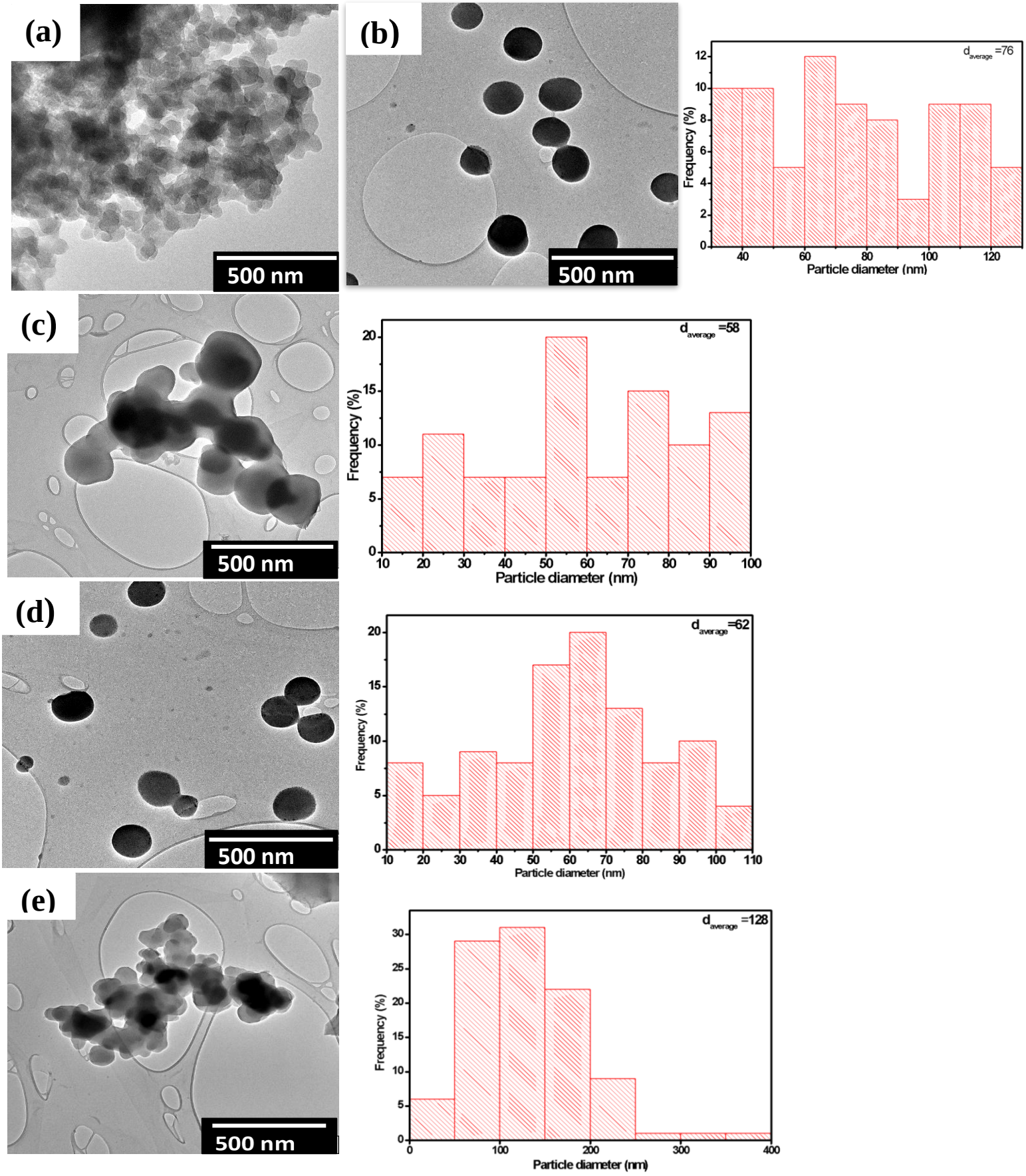

Figure 4.4: TEM images of (a) NSCS without activation, (b) NSCS2 KOH, (c) NSCS2 $ZnCl_2$, (d) NSCS3 KOH, and (e) NSCS3 $ZnCl_2$ all synthesized @ 850 ℃.

4.3.1.2 CHNS elemental analysis of the NSCS

CHNS elemental analysis was conducted to understand the percentages of C, N, S, and H elements that were present in the NSCS material as was stipulated that the onion raw material consists of these elements. CHNS was also used to understand the effect of the addition of activating agents on the elemental composition of the NSCS. **Table 4.1** shows the results of NSCS without activation, NSCS2 $ZnCl_2$, and NSCS3 $ZnCl_2$ samples. All the above-mentioned elements (C, N, S, H) were present at different percentages and varied depending on the amount of activating agent used. NSCS without an activating agent was observed to contain a high amount of carbon with a low amount of sulfur of which the CHNS technique was unable to detect. The sulfur quantity of 1.51 % was observed at low addition of $ZnCl_2$ whereas an undetected sulfur quantity was reported at the NSCS3 $ZnCl_2$ ratio. This was attributed to the increase of $ZnCl_2$ activating agent in the NSCS sample. It is noteworthy that the annealing temperature used was the same (850 ℃) in all the activated samples. The presence of sulfur was further evaluated by the XPS technique (section 4.3.2.7) and was found to be less than 0.5 %.

Table 4.1: CHNS elemental analysis comparison of NSCS without activation and NSCS activated with $ZnCl_2$ at different mass ratios.

Sample	**C (%)**	**H (%)**	**N (%)**	**S (%)**
NSCS without activation	70.92	0.65	5.66	Not detected
NSCS2 $ZnCl_2$	47.87	1.21	4.07	1.512
NSCS3 $ZnCl_2$	48.47	1.80	6.31	Not detected

4.3.1.3 PXRD analysis

The PXRD studies were performed to understand the degree of graphitization of the NSCS materials. The PXRD patterns of the nitrogen and sulfur co-doped carbon spheres prepared with activating agents are shown in **Figure 4.5**. The PXRD patterns showed that there is a shift of 2θ degrees when looking at the 1:2 ratio versus the 1:3 ratio in both KOH and $ZnCl_2$. The NSCS without activation consists of impurities marked with asterisks that are not present in the activated materials. This implies that there is an improvement in the material after the addition of activating agents [4]. The asterisks were observed at these different 2θ degree 16 °, 31 °, 35 °, and 44 °. While the value at 23° corresponds to the (002) interplane of graphite. The (002) peak was narrow compared to the other peaks; this implies improved crystallinity of the NSCS material. The PXRD patterns of the activated NSCS materials showed a broad peak at approximately 2θ = 26 ° and a very weak peak at 2θ = 43 ° (**Figure 4.5**), which are the characteristics of graphitic carbon materials with low graphitization degree. The implications of activation of NSCS were seen in the broader, well-defined (002) peak which shifted from the previously observed position in the NSCS without activation (23 to 26 °).

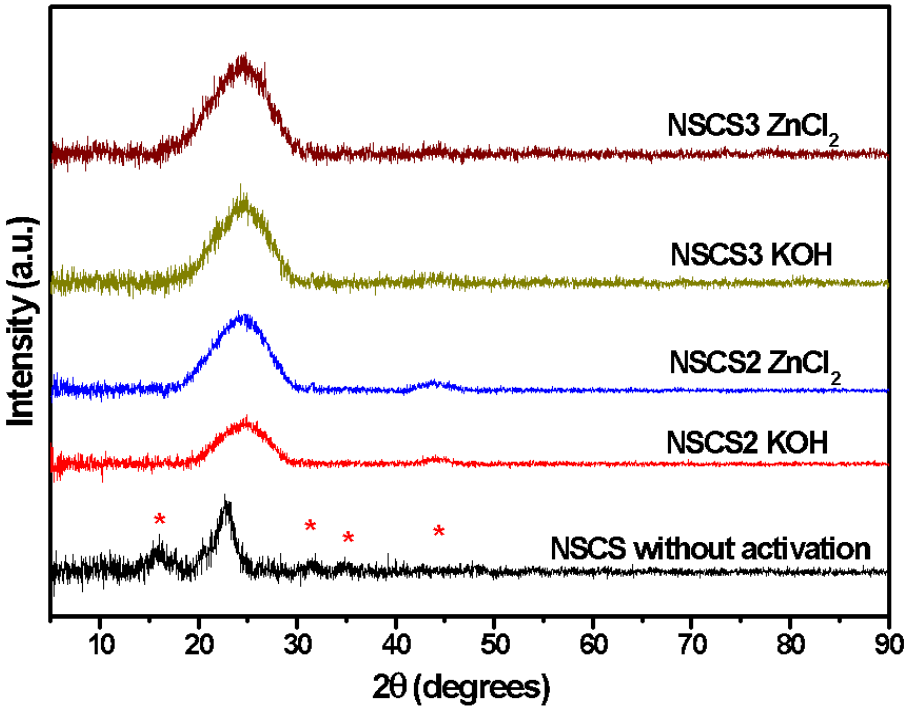

Figure 4.5: PXRD patterns of NSCS material showing the effect of an activating agent.

4.3.1.4 BET

The BET was used to obtain the specific surface area, pore-volume, and pore size of the NSCS material shown in **Table 4.2**. The specific surface area was observed at 130.7 m^2g^{-1}, 531.0 m^2g^{-1}, 532.1 m^2g^{-1}, 642.6 m^2g^{-1}, and 677.2 m^2g^{-1} for NSCS, NSCS2 KOH, NSCS2 $ZnCl_2$, NSCS3 KOH, and NSCS3 $ZnCl_2$, respectively. The higher specific surface area was observed with activated NSCS, this implies that the NSCS had characteristics of graphitic carbon materials with low graphitization degree as shown by the PXRD (section 4.3.1.3) [1,2,4]. which are the characteristics of graphitic carbon materials with low graphitization degree Moreover, the $ZnCl_2$ activated NSCS consists of a higher specific surface area and pore volume. This was attributed to more defects on the NSCS being introduced by $ZnCl_2$. From the BET it can be seen that different activating agents do not show much variation in the NSCS, however, the higher the ratio of the activating agent was added to the carbon material the higher the surface area was observed. The NSCS with the increased surface area can accommodate more titanium dioxide (TiO_2) nanoparticles and thus reduce the fast electron-hole recombination during photodegradation of dyes in the presence of a simulator solar light.

Table 4.2: BET results of NSCS at different activation ratios.

Sample	**Surface area** (m^2g^{-1})	**Pore volume** (cm^3g^{-1})	**Pore size** ***(nm)***
NSCS without activation	130.7	0.086	2.4
NSCS2 $ZnCl_2$	532.1	0.313	2.3
NSCS2 KOH	531.0	0.329	2.2
NSCS3 $ZnCl_2$	677.2	0.425	2.5
NSCS3 KOH	642.6	0.366	2.4

4.3.1.5 FTIR analysis

Chemical and structural information about the NSCS materials was further obtained from the FTIR spectra (**Figure 4.6**). The FTIR of NSCS without activation showed some of the prominent peaks including the C=C, C=N, and the carbonyl groups. Meanwhile, in the FTIR data obtained for both NSCS with KOH and NSCS with $ZnCl_2$, it is noticeable that the expected functional groups of the carbon spheres are present. These include the presence of C-S band around 1000 cm^{-1}, carboxylic anhydride band around 1220 cm^{-1}, C=C, C=N ($\tilde{\upsilon}$ = 1700 cm^{-1}), carbonyl groups ($\tilde{\upsilon}$ = 1600 cm^{-1}), C≡C, C≡N ($\tilde{\upsilon}$ = 2108 cm^{-1}), C-H stretching ($\tilde{\upsilon}$ = 2902 cm^{-1}) [22-24]. However, some of the bands are more prominent in the presence of KOH activation while others are more prominent in the presence of $ZnCl_2$. This can be attributed to the structural properties of the activating agents; KOH is more basic and $ZnCl_2$ is acidic, as a result, their effects on the NSCS material differ. It is evident that N and S functional groups are present in the carbon spheres' matrix.

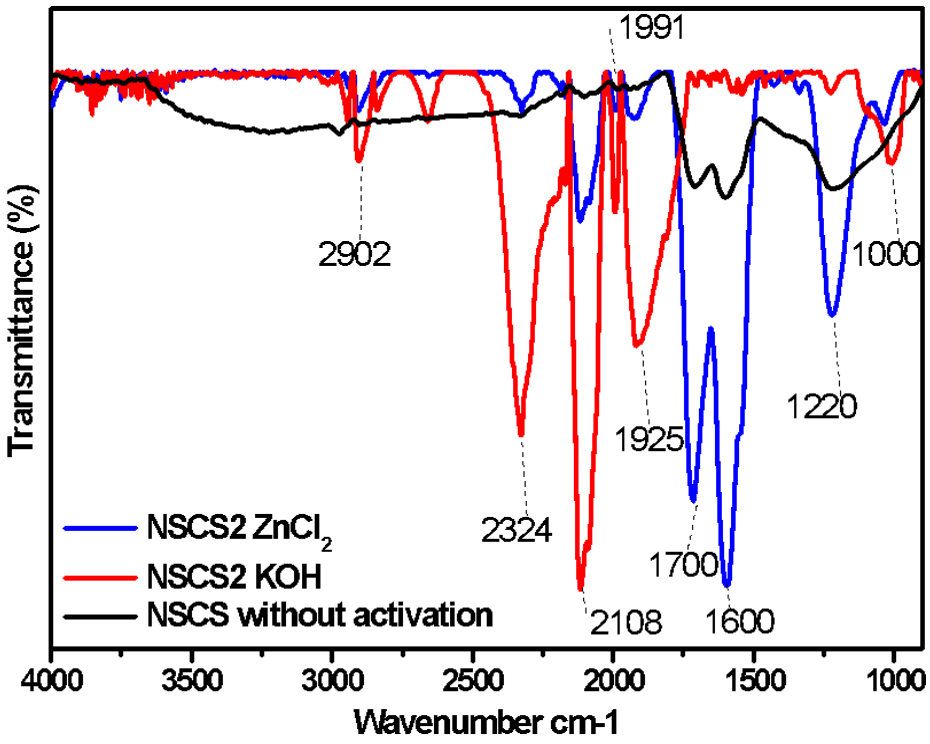

Figure 4.6: FTIR spectra of NSCS without activation, NSCS2 KOH, and NSCS2 $ZnCl_2$.

4.3.1.6 Laser Raman spectroscopy analysis

Figure 4.7 shows the laser Raman spectra of the NSCS without activation, NSCS2 KOH, and NSCS2 $ZnCl_2$ that were obtained using the hydrothermal process and annealed at 850 ℃ using a CVD method. Raman spectroscopy data were analyzed and from this, it can be concluded that the degree of carbonization was very high [25,26]. In Raman spectroscopy, the D band is disorder-induced, and the G band is associated with the C=C bond, sp^2-hybridized carbon [26]. The I_D/I_G ratio is often used to measure the level of disorder in graphite/graphene; where a ratio closer to 1 ensures more defects on the material. Raman spectra (**Figure 4.7**) reveal that both amorphousness and crystalline carbon coexist in these materials. The intensity ratios of the D and G bands (I_D/I_G and A_D/A_G) are nearly the same for these NSCS-based samples, reflecting their similar graphitization degree (**Table 4.3**). The Raman spectra corresponded with PXRD, and TEM analysis results where the presence of graphitic and a high level of disorder in NSCS material was reported.

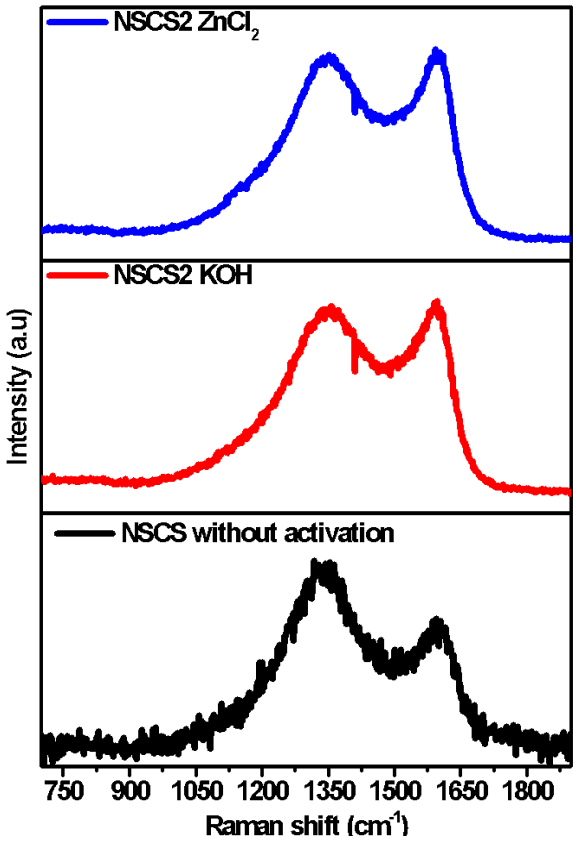

Figure 4.7: Raman spectra of (a) NSCS2 KOH, and (b) NSCS2 $ZnCl_2$.

Table 4.3: Laser Raman D and G, I_D/I_G ratio, and A_D/A_G of NSCS.

Sample	D (cm^{-1})	G (cm^{-1})	I_D/I_G	A_D/A_G
NSCS without activation	1339	1591	0.84	2.96
NSCS2 KOH	1362	1591	0.85	3.08
NSCS2 $ZnCl_2$	1353	1580	0.85	1.63

4.3.2 Effect of the annealing temperature and functionalization on the properties of the NSCS

4.3.2.1 TEM analysis of the annealed NSCS

Figure 4.8 shows TEM images of the NSCS2 $ZnCl_2$ prepared at various annealing temperatures followed by acid-functionalization to introduce functional groups on the surfaces of the NSCS. The functionalized NSCS material remained unbroken after the functionalization process. The chosen acid functionalization method has been reported that it does not change the morphology of the NSCS material, however, introduces functional groups on the surface of the NSCS [27]. The NSCS was observed to be accreted, forming a chain-like morphology. It is evident that agglomeration of NSCS does not completely change with annealing temperature, the average particle diameter however differs from 58, 74, and 64 nm, at 850, 900, and 950 ℃, respectively. The resultant particle diameters with variation of temperature were found to be comparable with the material activated by KOH. The temperature was introduced to improve the properties of NSCS such as large specific surface area, thermal, structural, and chemical. At 900 and 950 ℃ (**Figure 4.8** (**b)** and (**c**)), some roughness in the images was observed qualitatively, which can be proposed to be a result of high synthesis temperature [19,20]. The flake-like nature of the NSCS implies that the surface structure is defective. This suggests that if metals are attached to the surface they should bind with ease, resulting in application in photocatalysis degradation.

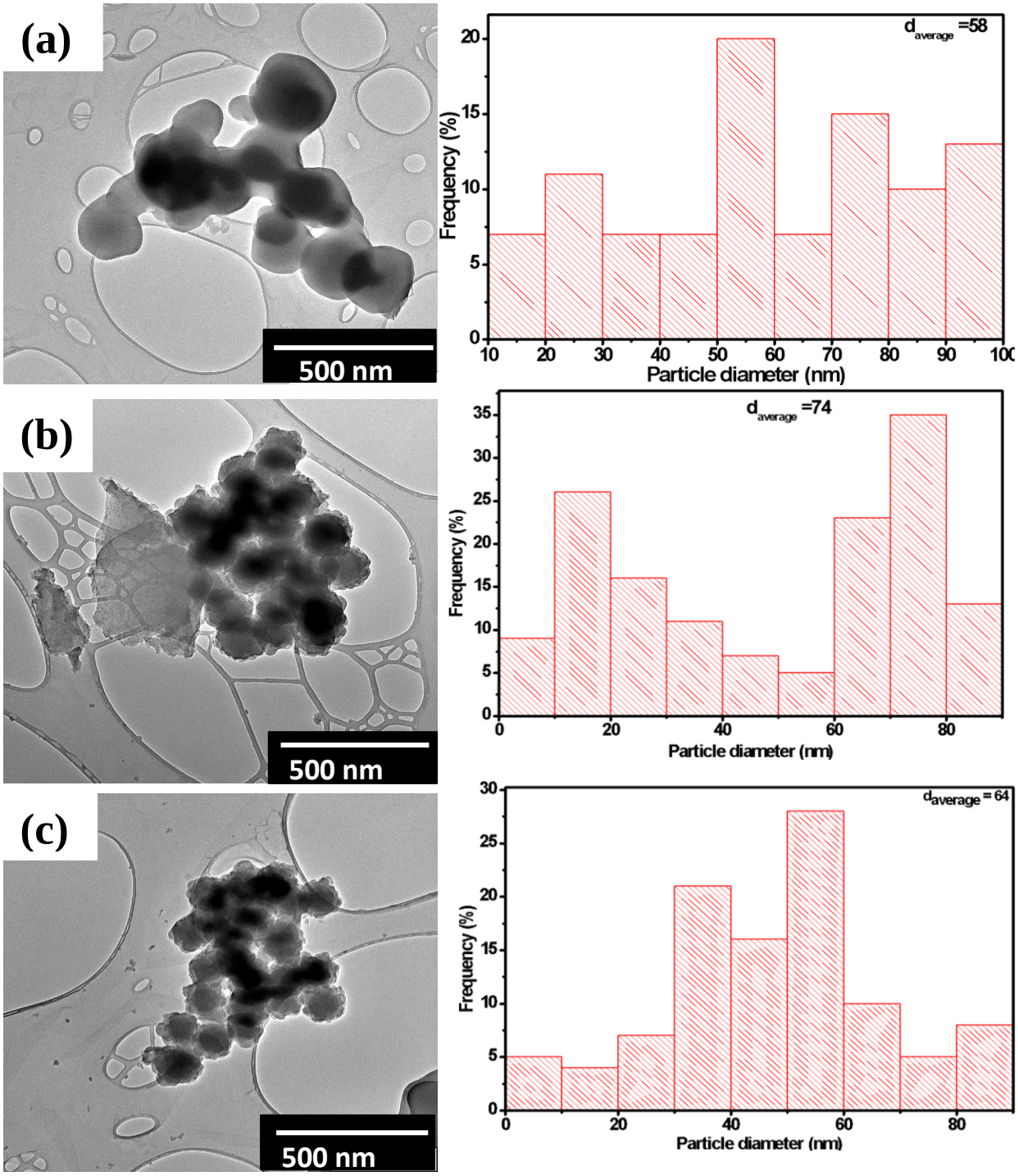

Figure 4.8. TEM images of the as-prepared: (a) NSCS2 $ZnCl_2$ @850 ℃, (b) NSCS2 $ZnCl_2$ @900 ℃, and (c) NSCS2 $ZnCl_2$ @950 ℃ with corresponding histograms.

4.3.2.2 SEM analysis of the annealed NSCS

It was observed that with an increase in annealing temperature the surface of the NSCS spheres transformed from smooth to rough. The roughness of the surface of carbon spheres has been explained to be consistent with the specific surface area of these materials and the introduction of the activating agent [4]. From SEM, the roughness of the NSCS material was evident and supported by the change in the morphology of the material. At 850 ℃, NSCS is spherical and resembles smooth and fluff-like materials; however, with the increase in temperature the spheres became agglomerated and exhibited spheres that could be described as rough. The spherical shape at annealing temperatures of 900 and 950 ℃ exist in different sizes. This can be attributed to the increase in thermal temperature as alluded to in the TEM analysis above.

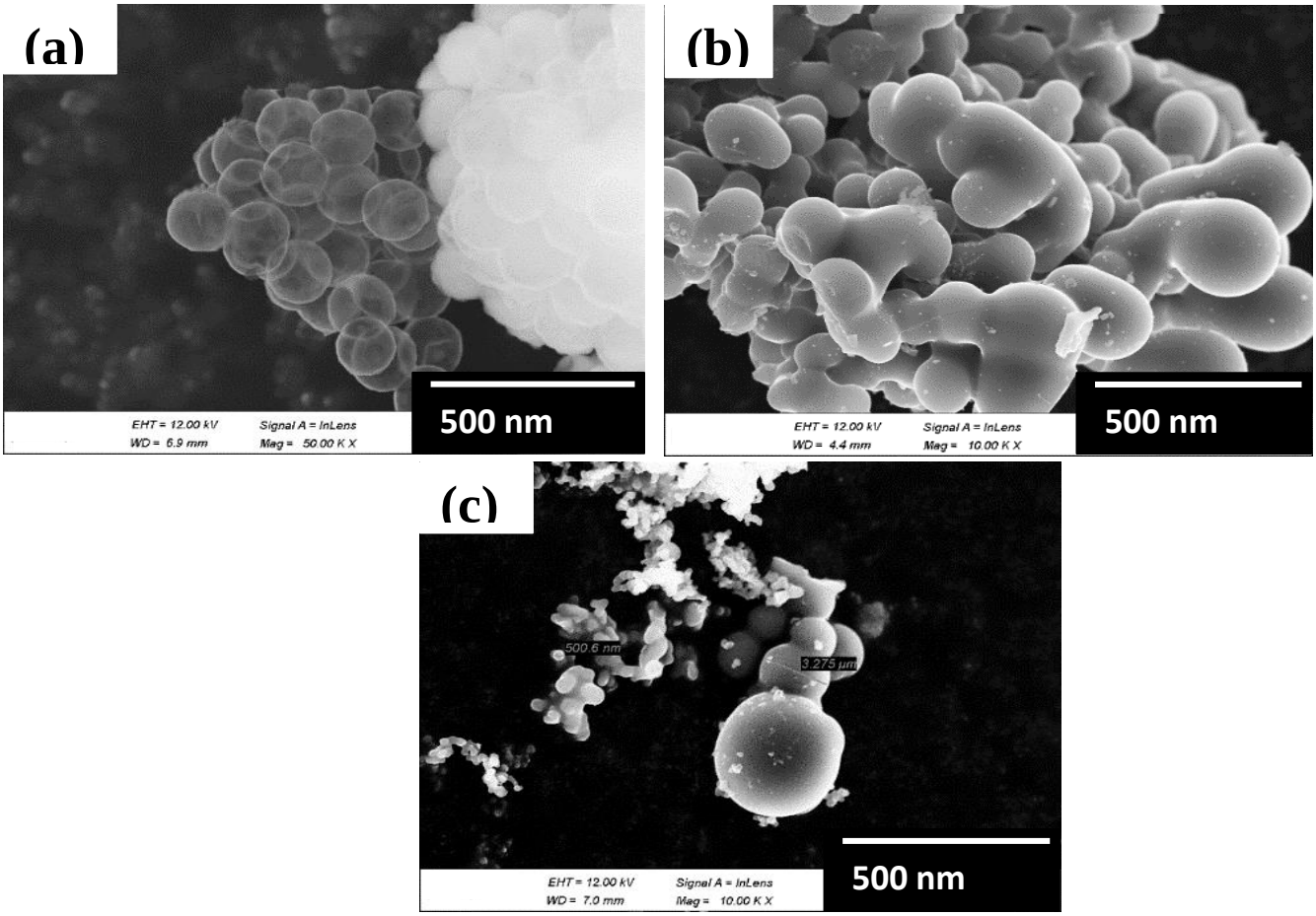

Figure 4.9. SEM images of the as-prepared: (a) NSCS2 $ZnCl_2$ @850 ℃, (b) NSCS2 $ZnCl_2$ @900 ℃, and (c) NSCS2 $ZnCl_2$ @950 ℃.

4.3.2.3 PXRD analysis of the annealed NSCS

The PXRD technique was used to investigate the properties of the NSCS material, **Figure 4.10**. It was observed that the (002) peaks are centered at 24.6 °, 25.3 °, and 25.5 ° for 850, 900, and 950 ℃ synthesis temperatures, respectively. Subsequently, the (100) peak at (44.1, 44.2, and 44.4 °) became more distinct and intense with an increase in thermal temperature, indicating increase in carbonization degree of the NSCS material. The (100) peak is that of in-plane scattering that suggests highly disordered amorphous carbon. The broad diffraction peaks (002) confirmed the presence of characteristics of the amorphous carbon phase of the NSCS materials. Previous studies reported that broadness in carbon spheres suggests the presence of an amorphous carbon phase within the carbon matrix [27,28]. The presence of amorphous properties improves the properties of carbon spheres and therefore their use in different applications. An improved crystallinity in the NSCS material was observed as the synthesis temperature increased.

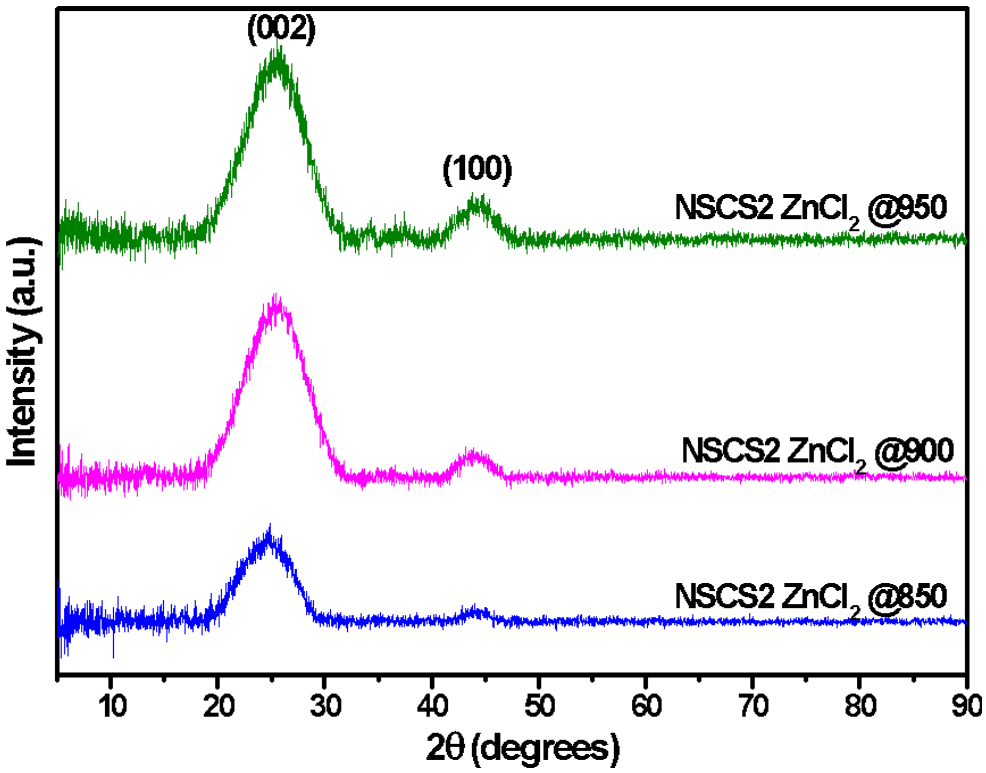

Figure 4.10: PXRD patterns of the NSCS materials at different synthesis temperatures.

4.3.2.4 Laser Raman spectroscopy analysis of the annealed NSCS

Laser Raman spectroscopy was applied to further understand the structural defects that were introduced by heteroatoms and $ZnCl_2$ activating agent in the NSCS. The first peak observed in all the spectra is that of the D band which differs in all the samples as shown in **Table 4.4**. The D band gave more information about the defects in the material attributed to the presence of N, S heteroatoms, and the added $ZnCl_2$ [4]. It is similarly ascribed to defects in hexagonal sp^2 carbon structure whereas the G-band is ascribed to sp^2 hybridized graphitic carbon atoms [19,20,27]. The G band showed that NSCS synthesized at 950 ℃ showed higher graphitic carbon, seen in the intensity of the G band peak. To further understand the effect brought forth by the variation of synthesis temperature in the material, I_D/I_G and A_D/A_G ratio were used to measure the degree of defects present in the NSCS, results are shown in **Table 4.4**. In all the samples, a D band was exhibited between 1349 cm^{-1} and 1355 cm^{-1}, **Figure 4.11**. In addition, a strong and narrow G peak was observed between 1580 cm^{-1} and 1589 cm^{-1}. The D band and G band peaks represent disordered sp^3 carbons and ordered sp^2 crystalline graphite-like structures, respectively [19-21]. The I_D/I_G ratio of all the analyzed material was found to be similar as a result of similar condition employed. This can be explained by the use of similar conditions to synthesize these materials, with emphasis on the increase in temperature does not distort the NSCS material.

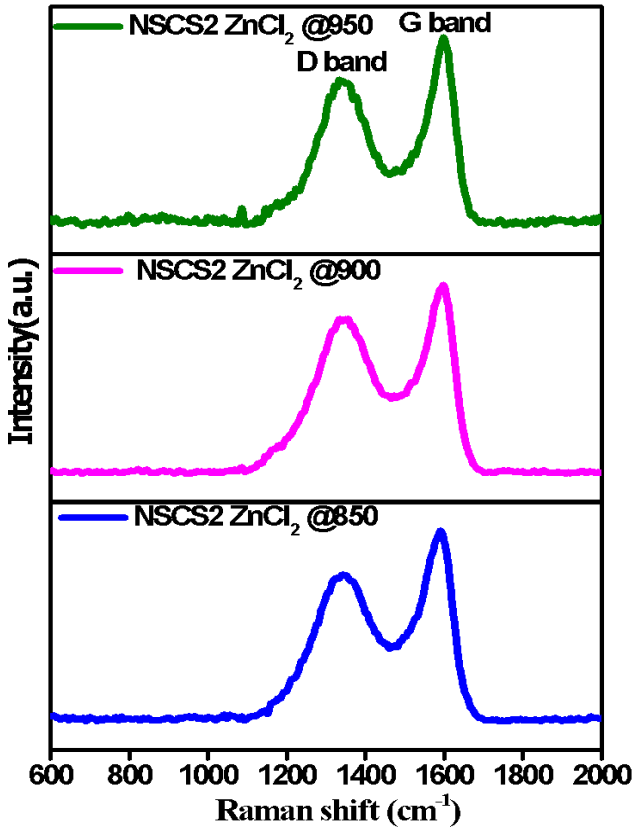

Figure 4.11: Raman spectra of NSCS2 $ZnCl_2$ annealed at different temperatures.

Table 4.4: Laser Raman D and G, I_D/I_G ratio, and A_D/A_G of the NSCS.

Sample	D (cm^{-1})	G (cm^{-1})	I_D/I_G	A_D/A_G
NSCS2 $ZnCl_2$ @ 850	1353	1580	0.85	1.63
NSCS2 $ZnCl_2$ @ 900	1355	1580	0.85	1.83
NSCS2 $ZnCl_2$ @950	1349	1589	0.85	1.52

4.3.2.5 BET analysis of the annealed NSCS

The BET analysis was used to investigate the specific surface area of the synthesized NSCS. In **Table 4.5**, specific surface area, pore-volume, and mean pore diameters are listed (at various synthesis temperatures). The NSCS material annealed at 850 ℃ showed a low specific surface area of 532.1 m^2g^{-1} with a corresponding mean pore diameter of 2.3 nm. However, as the synthesis temperature increased from 850 to 950 ℃, the specific surface area of NSCS decreased from 630.2 observed at 900 ℃ to 536.9 m^2g^{-1} at 950 ℃. The synthesized NSCS reveals no clear trend as synthesis temperature was increased. The NSCS sample synthesized at 900 ℃ showed a higher specific surface area, this observation was also supported by the decrease in the oxygen content observed in **Table 4.6**. The reduction in O_2 content observed when synthesis temperature is increased supports the increase in specific surface area in carbonaceous materials [28].

Table 4.5: Comparison of the NSCS annealed at different temperatures.

Sample	**Surface area (m^2g^{-1})**	**Pore volume (cm^3g^{-1})**	**Pore diameter (nm)**
NSCS2 $ZnCl_2$ @850	532.1	0.31	2.3
NSCS2 $ZnCl_2$ @900	630.2	0.36	2.7
NSCS2 $ZnCl_2$ @950	536.9	0.33	2.5

4.3.2.6 FTIR analysis of the annealed NSCS

FTIR is a technique that measures the quantity of radiation observed in correspondence to its frequency. In the fingerprint region, below 1400 cm^{-1} there is a peak observed in all the spectra which correspond to the C-S bond ($\tilde{\upsilon}$ = 1000 cm^{-1}). This further confirms the presence of sulfur

heteroatom. It is noticeable that the expected functional groups on the surface of NSCS are present. These include the presence of the C-S band, carboxylic anhydride band, C=C, C=N, carbonyl groups, C≡C, C≡N, and C-H stretching [22-24]. A spectrum of the quantity of radiation absorbed versus frequency was plotted, **Figure 4.12**. This gave information about the different regions present and those prominent in the desired NSCS. With different synthesis temperatures, there are some differences in the spectra, however, all the spectra depict similar bonding as explained in section 4.3.1.5. In addition, information about the covalent bonding of N=C and C-S components was observed from the NSCS material.

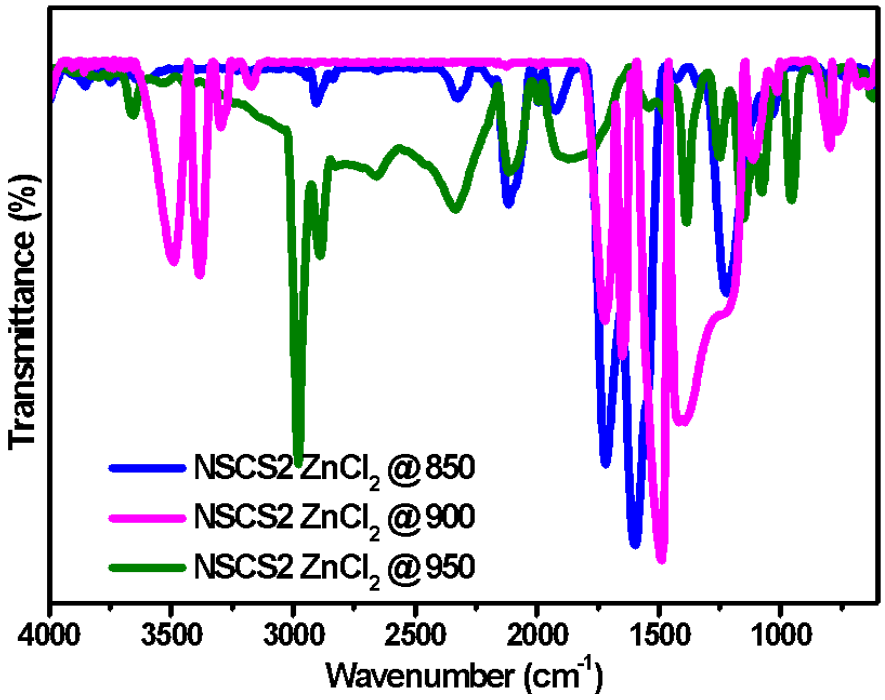

Figure 4.12: FTIR spectra of as-synthesized NSCS2 at 850, 900, and 950 ℃.

4.3.2.7 XPS Analysis of the annealed NSCS

More insight about the chemical surface covalent bonding of N, S, C, and O elements was investigated by XPS. **Figure 4.13** illustrates the spectra of NSCS annealed at various temperatures with corresponding **Table 4.6** showing the elemental identification and atomic percentages of the elements found in the sample. The NSCS material without activation was included for comparison. Here it can be seen that NSCS material consists of a high percentage of O_2 content (21.2 %). However, the increase in synthesis temperature and addition of $ZnCl_2$ activation resulted in a decrease in oxygen content (8.2, 4.3, and 7.4 % for temperatures at 850, 900, and 950 ℃, respectively). This observation is interconnected with the BET analysis (section 4.3.2.5), that the reduced O_2 content results in a high specific surface area [20]. The XPS spectrum survey demonstrates the C1s peaks being the dominant peaks at 284.4 eV, an O 1s peaks at 532.0 eV, an N 1s peak (399.8 eV), and an S peak (164.1 eV) in all the samples. The sulfur peak is very weak in all the materials with the obtained content of less than 0.5 % as confirmed by CHNS elemental analysis (section 4.3.1.2).

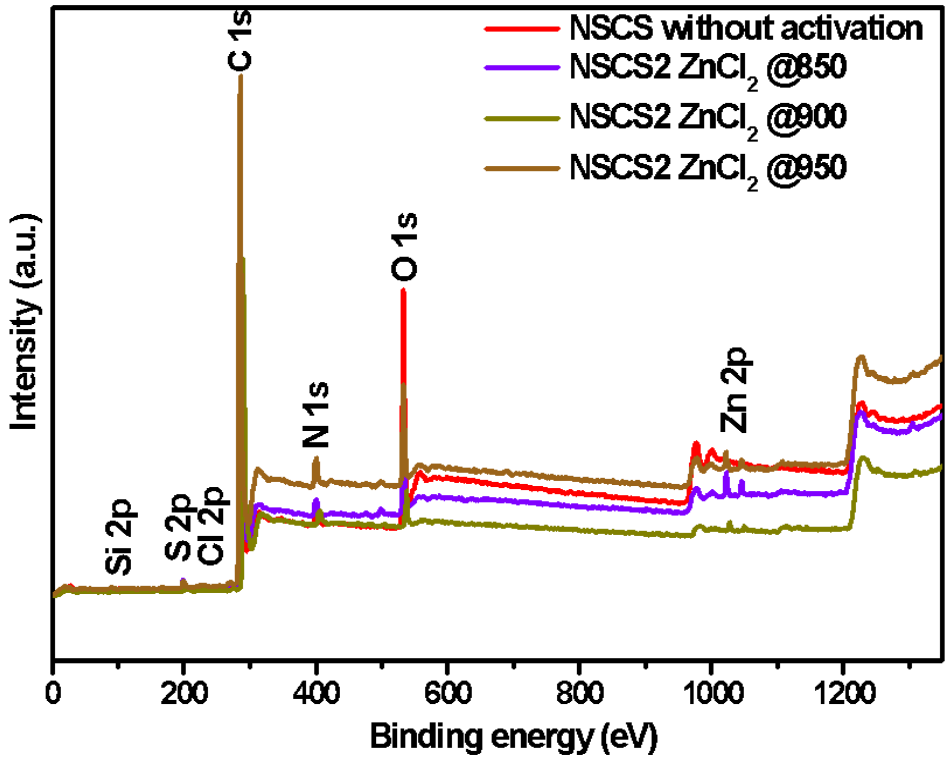

Figure 4.13: XPS spectra of as-synthesized NSCS, NSCS2 at 850, 900, and 950 ℃.

Table 4.6: XPS elemental analysis of NSCS materials synthesized at various temperatures in .

Sample	**%C 1s**	**%O 1s**	**%N 1s**	**%S 2p**	**%Cl 2p**	**%Zn 2p**	**%Si 2p**
NSCS without activation	75.5	21.2	2.8	0.3	-	-	0.2
NSCS2 $ZnCl_2$ @850	86.3	8.2	3.6	0.2	1.0	0.3	0.2
NSCS2 $ZnCl_2$ @900	90.2	4.3	4.2	0.2	0.6	0.2	0.4
NSCS2 $ZnCl_2$ @950	86.5	7.4	4.6	0.3	0.7	0.3	0.2

The high-resolution spectra of C 1s and O 1s are shown in **Figure 4.14** below. The C 1s spectrum was deconvoluted into different C 1s species; C-C sp2 at 284.2 eV, C-C sp3 at 285.0 eV, C-O at 286.4. eV, C=O at 287.8 eV, and O-C=O at 288.8 eV. These were the probable surface chemical bonding of the carbon element. While **Figure 4.14** (**b**) demonstrates a high resolution of O 1s species. Three different peaks were designated to: C-O at 529.6 eV, C-O at 531.2 eV, and C=O at 532.4 eV [8,20].

The nitrogen spectrum was further deconvoluted into three Gaussian peaks shown in **Figure 4.14** (**c**)**.** The different types of N groups that were observed are, 397.9, 399.4, 400.3, and 405.2 eV. These were attributed to pyridinic-N, pyrrolic-N, quaternary-N, and oxidized-N, respectively [20]. The sulfur deconvoluted spectrum proved to be difficult due to low percentages in the material (**Figure 4.14** (**d**))**.** However, the sulfur species could be deconvoluted into three types of sulfur: C-SOx (169.8 eV), C=S (167.8 eV), and 166.4 eV corresponding to S $2p_{1/2}$ and S $2p_{3/2}$ of the C-S-C. The XPS analysis also showed the characterization of the oxidation states of the pyrite S $2p_{1/2}$ and S $2p_{3/2}$ (**Figure 4.14** (**d**)). These different types of chemical bonding configurations suggest that the synergy effect took place between N 1s, S 2p, and C atoms. In the above observation, there are some impurities observed in the prepared material, as there are peaks from Zn and Cl from

$ZnCl_2$ activation, with a 0.8 % content (**Table 4.6**). The present impurities are a result of the washing step where it has been explained that removal of metals is difficult, however, with such a low amount of content it can be anticipated that the NSCS can still be used as support for TiO_2 semiconductor. A small percentage of 1 % was allocated to Si due to silicon (SiO_2), which came from the sample preparation before XPS analysis. Since the observed impurities contributed a small percentage (1.8 %) in the bulk of the material, their impact on the material was expected to be trivial. Just as FTIR proved the presence of N, S, and C elements, XPS further confirmed the presence of different types of configurations in the onion raw material that benefits the material for biomass use.

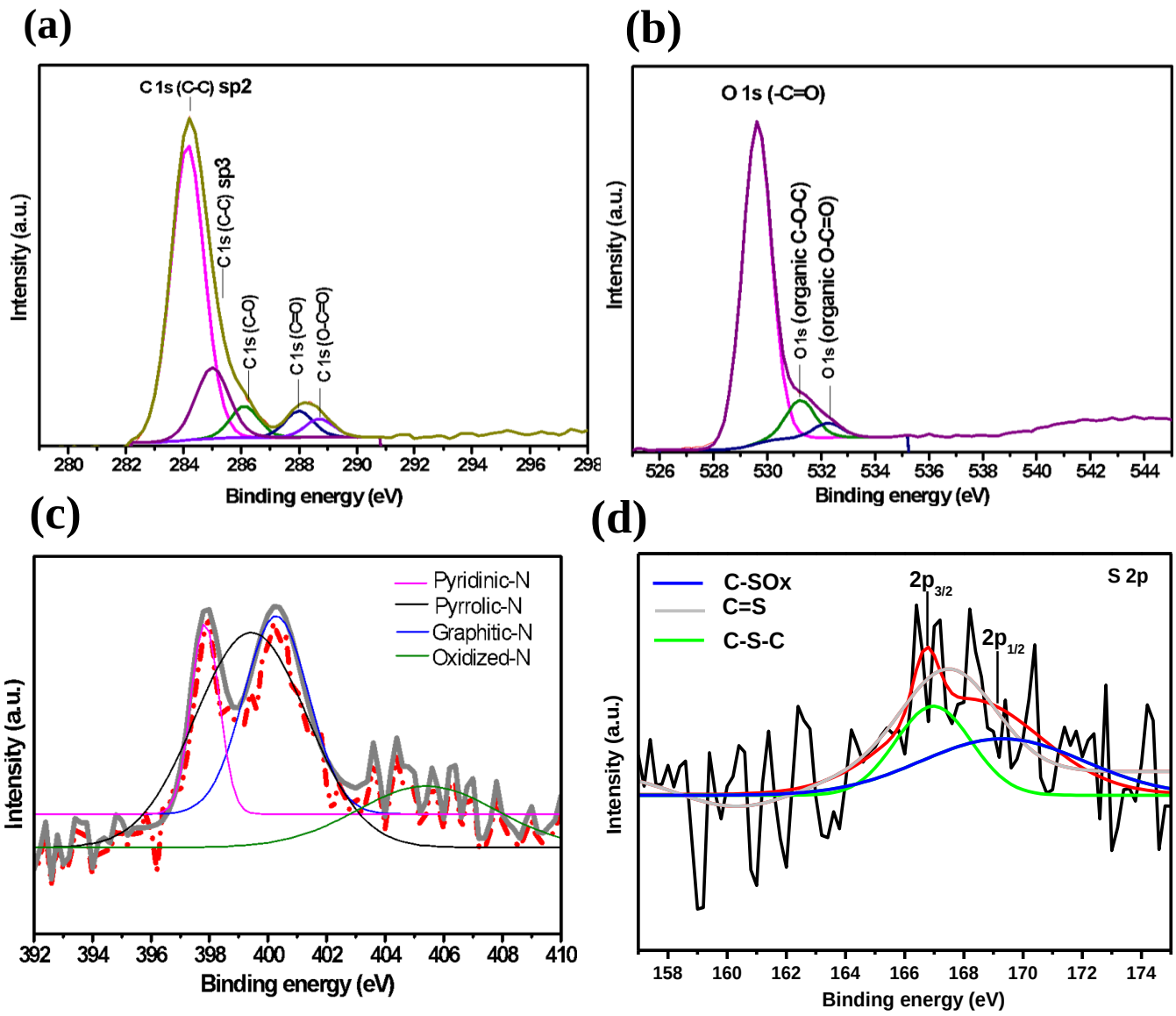

Figure 4.14: High-resolution XPS spectra of the annealed NSCS (a) C 1s, (b) O 1s, (c) N 1s, and (d) S 2p.

4.3.2.8 TGA analysis of the annealed NSCS

The TGA shows two decomposition peaks, corresponding to the oxidation of carbon in NSCS and oxidation of graphite. The TGA graph depicts that the thermal stability of the material varies with the synthesis temperature. This is consistent with the results obtained from Raman spectra where the increase in synthesis temperature resulted in more crystalline materials. Two thermal decomposition steps were observed in all the materials synthesized at various temperatures. The

first thermal decomposition can be seen from ~99 ℃ which can be attributed to the moisture in the sample with (~20-25 wt.%). The second step represents the decomposition of the carbon material. The carbon material is completely burnt off with 0 wt.% observed in all the TGA profiles. **Figure 4.15** (**b**) shows the percentage of decomposition temperature. It can be seen that with the increase in annealing temperature the carbon decomposition peaks were similar showing high thermal stability. From the obtained TGA there was no weight loss around 400 ℃ due to the amorphous carbon in the NSCS, which is then in agreement with PXRD observations about the presence of amorphous carbon. The high thermal stability of NSCS can allow for use as support materials for TiO_2 producing NSCS_TiO_2 composite and the further testing of the prepared composite under photodegradation application at ambient temperatures.

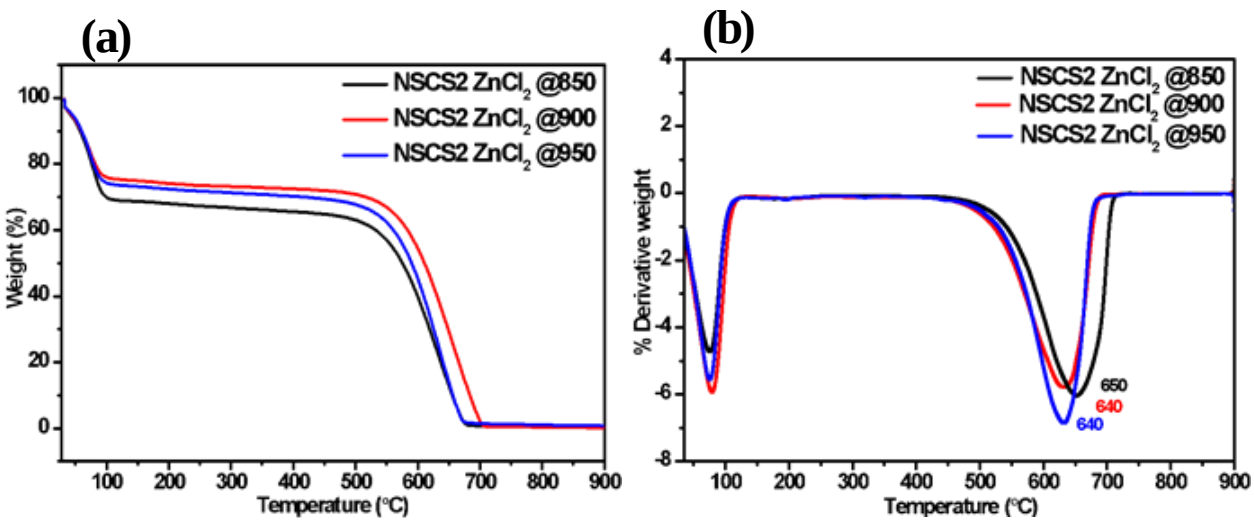

Figure 4.15: (a) TGA and (b) DTG thermograms of NSCS annealed at 850, 900, and 950 ℃.

4.4 CONCLUSION

NSCS with different diameters were synthesized from the onion raw material through a hydrothermal process followed by the CVD method. NSCS was annealed at 850 °C under the N_2 gas atmosphere for two hours in a horizontal furnace with a heating rate of 5 °C/min. A mass ratio of (1:2 and 1:3) of KOH and $ZnCl_2$ activating agents were employed in the synthesis of NSCS for the improvement of spherical shapes. In this study, the morphology of the as-prepared NSCS material was investigated by the TEM technique. TEM showed that after the addition of KOH and $ZnCl_2$, NSCS with improved spherical shapes formed. After annealing NSCS activated with KOH

and $ZnCl_2$ proved to have different average diameters (58, 76, 62, and 128 nm). From SEM it was observed that at high annealing temperatures NSCS spheres became highly agglomerated. PXRD and Raman spectroscopy showed that variation in annealing temperature in nitrogen, sulfur co-doped carbon spheres was found to be highly graphitized. Analysis of BET showed an increase in specific surface area when NSCS without activation was employed and when activating agents were added (130.7 to 677.2 m^2/g). This increase agrees with the roughness of the spheres obtained in TEM and SEM.

The TEM and SEM of NSCS material that was synthesized by employing $ZnCl_2$ activating agent and later subjected to variation of synthesis temperatures (850-950 ℃); showed similar morphological and particle diameter improvement as explained above. CHNS elemental analysis showed that NSCS contained carbon, nitrogen, sulfur, and hydrogen elements. The NSCS was found to have a nitrogen content of 3.6, 4.2, and 4.6 for NSCS synthesized at 850, 900, and 950 ℃, respectively as determined by XPS. Four bonding configurations of nitrogen were obtained: pyridinic-N, pyrrolic-N, quaternary-N, and oxidized-N. Furthermore, peaks denoted to C=S and C-S-C bonding configurations were obtained at 167.8 eV and 166.4 eV from the XPS spectra. This confirmed the presence of N, S, and C elements from the onion material, which substantiates the self-doping of the material. As the developing research in heterogeneous, the NSCS material can be used as support for TiO_2 semiconductor to study the effects and improvements that happen in the photodegradation of organic dyes.

4.5 References

1. Lozano-Castello´D., Lillo-Ro´denas M.A., Cazorla-Amoro´s D. & Linares-Solano A. Preparation of activated carbons from Spanish anthracite I. Activation by KOH. Carbon 39 (2001); 741 –749.
2. Lillo-Ro´denas M.A., Lozano-Castello´D., Cazorla-Amoro´s D. & Linares-Solano A. Preparation of activated carbons from Spanish anthracite II. Activation by NaOH. Carbon 39 (2001); 751 –759.
3. Wickramaratne N.P.& Jaroniec M. Activated Carbon Spheres for CO_2 Adsorption. ACS Appl. Mater. Interfaces (2013); (5): 1849−1855.
4. Yang S., Mao X., Cao Z., Yin Y., Wang Z., Shi M. & Dong H. Onion-derived N, S self-doped carbon materials as highly efficient metal-free electrocatalysts for the oxygen reduction reaction. Appl Surf Sci. (2018); 427:626-634.
5. Deshmukh A.A., Mhlanga S.D. & Coville N.J. Carbon spheres. Mater Sci Eng R Reports. (2010); 70(1-2):1-28.
6. Jin Y.Z., Kim Y.J., Gao C., Zhu Y.Q., Huczko A., Endo M. & Kroto H.W. Carbon. (2006); 44, 724.
7. Serp P. & Figueiredo J.L. Carbon materials for catalysis: Catalytic properties of N-containing carbons (Chapter 7.): Wiley; 1st ed. (2009); 219-257.
8. Tetana Z.N. Boron and nitrogen doped carbons for photochemical degradation reactions. Thesis (University of the Witwatersrand, Johannesburg, 2013).
9. Zhang Y., Yang W., Luo R. & Shang H. Preparation of carbon nanospheres by non-catalytic chemical vapor deposition and their formation mechanism. New Carbon Materials. (2016); 31(5): 467-474.
10. Aili M., Xiaomin W., Tianbao L., Xuguang L. & Bingshe X. Characteristics of carbon microspheres and study on its adsorption isotherms. Mater. Sci. Eng. A 443 (2007); 54-59.
11. Zhao S., Wang C.-Y., Chen M.-M. & Sun J.-H. Mechanism for preparation of carbon spheres from potato treated by NH_4Cl. Carbon. (2009); 47 (1): 331-333.
12. Wang Q., Li H., Chen L. & Huang X. Monodispersed hard carbon spherules with uniform nanopores. Carbon. (2001); 39(14): 2211-2214.

13. Xu G., Han J., Ding B., Nie P., Pan J., Dou H., Li H. & Zhang X. Biomass-derived porous carbon materials with sulfur and nitrogen dual-doping for energy storage Green Chemistry. (2015); 17(3): 1668-1674.
14. Yu Y.-N., Wang M.-Q. & Bao S.-J. Biomass-derived synthesis of nitrogen and phosphorus Co-doped mesoporous carbon spheres as catalysts for oxygen reduction reaction. J Solid State Electrochem. (2017); 21:103–110.
15. Osorio A.G., Silveira I.C.L., Bueno V.L. & Bergmann C.P. H_2SO_4/HNO_3/HCl-Functionalization and its effect on dispersion of carbon nanotubes in aqueous media. Applied Surface Science 255 (2008); 2485–2489.
16. Guo X., Yang Y. & Liu X. Preparation and characterisation of vinyl-functionalized carbon spheres by allylamine. Applied surface science (2011); 257(15): 6672-6677.
17. Du D., Zou Z., Shin Y., Wang J., Wu H., Engelhard M.H., Liu J., Aksay A.I. & Lin Y. Sensitive Immunosensor for Cancer Biomarker Based on Dual Signal Amplification Strategy of Graphene Sheets and Multienzyme Functionalized Carbon Nanospheres. Anal. Chem. (2010), 82, 2989–2995.
18. Paraknowitsch J.P. & Thomas A. Doping carbons beyond nitrogen: An overview of advanced heteroatom doped carbons with boron, sulphur, and phosphorus for energy applications. Energy Environ Sci. (2013); 6(10):2839-2855.
19. Manikai S.M. The Synthesis of Nitrogen Doped Carbon Spheres as Supports for Palladium Catalysts in the Hydrogenation of cinnamaldehyde. Thesis (University of the Witwatersrand, Johannesburg, 2015).
20. Dlamini M.W. Spherical carbons as model supports for Fe, Co and Fe-Co Fischer-Tropsch catalysts. Thesis (University of the Witwatersrand, Johannesburg, 2016).
21. Mongwe T.H., Matsoso B.J., Mutuma B.K., Coville N.J. & Maubane M.S. Synthesis of chain-like carbon nano-onions by a flame assisted pyrolysis technique using different collecting plates. Diam Relat Mater. (2018); 90:135-143.
22. Harvey D. Modern Analytical Chemistry. First edition. Chapter 10. McGraw-Hill. United States of America (2000).
23. Fifield F.W. & Kealey D. Principles and Practice of Analytical Chemistry. Chapters 7 and 9. Fifth Edition. Blackwell Science. UK (2000).

24. Jeffrey G. H., Bassett J., Mendham J. & Denney R. C. Vogel's Textbook of Quantitative Chemical Analysis. Chapter 19. Fifth Edition. UK (1999).
25. Ferrari A.C. & Robertson J. Interpretation of Raman spectra of disordered and amorphous carbon. Phys. Rev. Soc. (2000); 61:14095.
26. Robertson J. Diamond-like amorphous carbon. Mat. Sci. and Eng. (2002); 37: 129-28.
27. Phaahlamohlaka T.N. Synthesis of carbon nanofibers and their subsequent use as catalyst supports for Fischer-Tropsch synthesis. MSc Dissertation (University of the Witwatersrand, Johannesburg, 2013).
28. Yan D., Yu C., Zhang X., Qin W., Lu T., Hu B., Li H. & Pan L. Nitrogen-doped carbon microspheres derived from oatmeal as high capacity and superior long life anode material for sodium ion battery. Electrochimica Acta. (2016); 191:385-391.

CHAPTER 5:
Synthesis and characterization of TiO_2 nanoparticles and TiO_2 incorporated with NSCS prepared by the sol-gel method for photodegradation of Rhodamine B

5.1 Introduction

The industrialization has resulted in extensive pollution of the environment. This has been followed by widespread studies on ways of controlling and mitigating the consequences of pollution. Textiles, food processing, cosmetics, and pharmaceuticals are some of the growing industries that have been causing the rise in environmental pollution [1-5]. For instance, in the textile industries, dyes and large volumes of water are employed for fabrics manufacturing, while discharging the wastewater to various water bodies [1]. Conversely, dyes during the operation process produce harmful compounds that include but are not limited to non-biodegradable intermediate dyes, waste solvents, inorganic compounds, and organometallic compounds, which are usually found at different pH, concentration, and quantities [1,2]. Techniques including adsorption, electrolysis, ion exchange, reverse osmosis, and advanced oxidation processes (AOPs) have been used for wastewater treatment [1-5]. However, most of these processes lead to post-treatments which can be costly. As a result, industries avoid the post-treatment stage.[3]. AOPs remain the choice of purification method as they make use of destructive processes that are non-selective on the type of pollutant to be degraded [4]. This process works on active species found in wastewater, which when coupled with light it generates hydroxyl groups, that oxidize the organic pollutant [4]. Semiconductors such as TiO_2, ZnO, ZnS, and others have been studied [3-5].

In this study, the focus is on the use of TiO_2 composited with carbonaceous materials. The drawbacks experienced when applying TiO_2 as a photocatalyst encouraged further investigations to advance the use of TiO_2 as a catalyst. Investigations on different ways of modification of semiconductor electronic structure of TiO_2 using metals and non-metals have been studied [6-10]. A study conducted by Shayegan et al. [11] found that anionic doping of TiO_2 with either N, S, C, P or B replaces O_2 atoms from TiO_2 thus enhancing the photocatalytic activity. Modification of TiO_2 is mostly based on its electronics and optical properties to enhance its photocatalytic activity

under the visible region of the light spectra, when used as a photocatalyst for photodegradation of organic pollutants [12,13]. Schottky barrier takes place with carbonaceous material incorporated with TiO_2, which is merely a formation of the space-charge region during the photochemical process [6]. Doped carbon materials have been reported to be resistant to both acidic and basic media; the structure of the doped carbon is stable at high temperatures and carbons are relatively cheaper compared to other conventional catalyst support [14-18]. In literature, it has been explained that grain boundaries in interconnected spherical TiO_2 particles are expected to be high, due to the high resistance that is experienced by the particles [19,20]. Heteroatom doped carbon spheres were later investigated as plausible support for TiO_2 in photodegradation studies [7].

The photocatalytic studies for the anatase TiO_2 incorporated with NSCS will be evaluated separately under solar simulator light. This present study aimed at understanding the influence introduced by nitrogen, sulfur co-doped carbon spheres (NSCS) in photocatalytic degradation. This process involves a suspension with water as the solvent of choice interacting with the photocatalyst. Rhodamine B (RhB) was chosen as the organic pollutant; its photocatalytic degradation in TiO_2 suspension has been vastly studied [4-12,21,22]. The interest emerged from the aromatic rings present in the RhB structure, which required more time to decompose as compared to other organic dyes that had structures with less aromatic rings. Aromatic rings consist of pi (π) electrons that are delocalized around the compound, as a result are difficult to break down using natural sunlight.

5.2 Experimental procedure

5.2.1 Sol-gel method for preparation of TiO_2, and TiO_2-NSCS catalysts

The sol-gel method is the most preferred method for the synthesis of anatase TiO_2 as it can reduce the particle size to nanoparticles. Herein, 0.02 percent of NSCS was mixed with ethanol and stirred vigorously while titanium (IV)-n-butoxide ($Ti(OBu)_4$) was slowly added by use of a burette shown in **Figure 5.1**. To obtain homogeneity, the mixture was stirred for an hour. Nitric acid was added dropwise with distilled water to make up 99.98 percent of TiO_2 in total. The reaction was performed at room temperature while constantly stirring for 3 hours under the fume-hood. The mixture was left to age for 24 hours to allow the sol to transform into a gel. Solvents were

evaporated followed by annealing of the composite under N_2 gas at 450℃ held for 3 hours. Production of white nanoparticles of TiO_2 was synthesized following the same procedure as below.

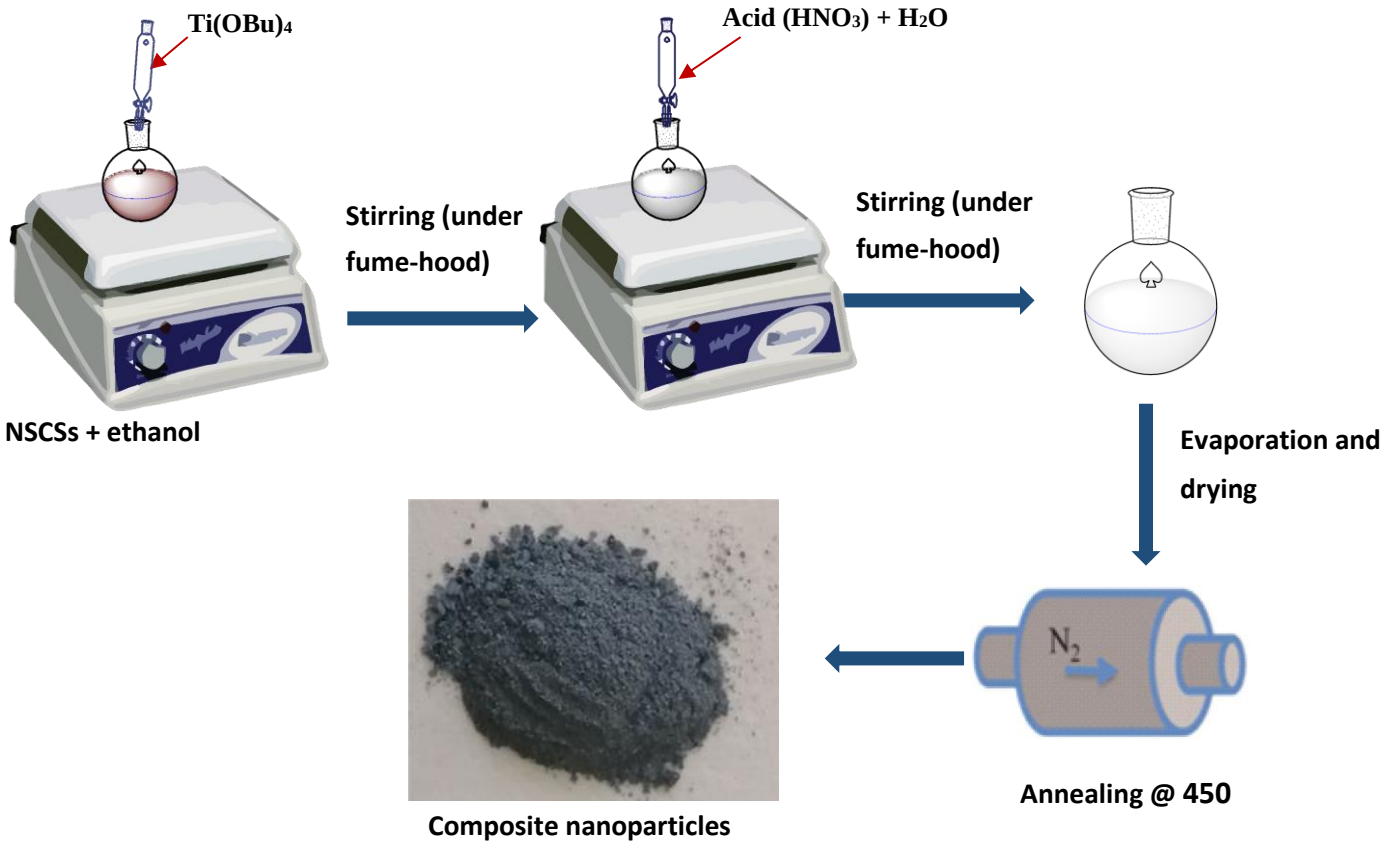

Figure 5.1: Experimental procedure of preparation of TiO_2 nanoparticles and the composite.

5.2.2 Photodegradation measurements

The chemicals and the Rhodamine B dye employed in this work were obtained from the laboratory type of environment. Thus far, the optimum dye concentration that has been used for dye degradation is 50 mgL^{-1}. Dye removal was done at room temperature (25 ℃). The as-prepared photocatalyst was used for the degradation of RhB dye. A stock solution was prepared in a 500 mL volumetric flask, this was then varied in terms of dye concentration (i.e., 5, 10, 15, 20, and 25 ppm). Consequently, the photocatalyst loading was varied (5, 10, 15, 20 mg). A 50 mL cylindrical

glass containing a suspension of the dye and TiO_2_NSCS was stirred in the dark for an hour to allow for homogeneity. An aliquot (~3 mL) was taken before exposing the solution to light which was then analysed using the UV-Vis spectroscopy. The solution was then exposed to light using Newport model solar simulator and the same number of aliquots (~3 mL) were taken every 15 minutes for 150 minutes. Dye composition was determined using UV-Vis spectroscopy at a wavelength of 553 nm determining the sample's absorbance. UV-Vis spectroscopy was calibrated using standard solutions [12,23].

5.3 Results and Discussions

5.3.1 Materials characterization

5.3.1.1 PXRD analysis

The PXRD technique was studied to determine the crystal phase composition of pure TiO_2 and the TiO_2_NSCS catalysts. The PXRD diffractograms of pure TiO_2 and the TiO_2_NSCS composites are shown in **Figure 5.2.** The PXRD analysis of TiO_2_NSCS catalysts synthesized at 850, and 900 ℃ predominantly showed peaks of the anatase phase TiO_2. The observations differ from what was observed in **Figure 4.3.1.3**, where (002) and (100) indexed were seen at ~25 and ~44 (2 theta degrees), respectively for the NSCS material. The diminishing NSCS peaks were attributed to the overlap of the NSCS with the intensity of TiO_2 peaks [24]. However, all the characterized materials depict similar peaks of TiO_2 in anatase phase, with an intense peak being that of the (101) hkl plane. The pure TiO_2 diffractogram showed more crystalline peaks. While after NSCS incorporation, the width of the TiO_2 peaks became broader depending on the synthesis temperature and the amount of activating agent used. The width difference has been previously reported to be due to the incorporation of carbonaceous materials that alter the unit cell of TiO_2 [24]. The average crystallite size was calculated using Debye Scherer's equation. The average crystallite size was calculated to be 12, 8.2, and 9.9 nm for TiO_2, TiO_2_NSCS2 @850, and TiO_2_NSCS3 @900, respectively (**Table 5.1**). It was observed that incorporation of NSCS material results in a decrease in the average crystallite size of TiO_2. This decrease was attributed to the C material defects that are introduced on the surface of TiO_2.

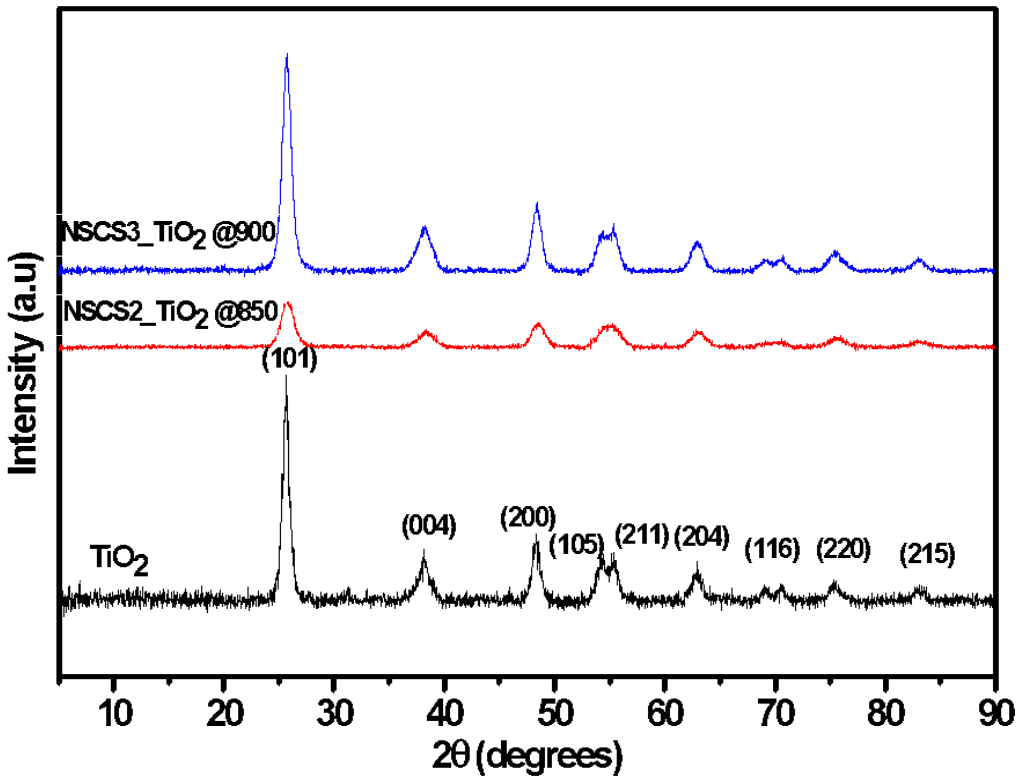

Figure 5.2: PXRD patterns of the synthesized TiO_2 and the TiO_2_NSCS catalysts.

Table 5.1: Average crystallite size of TiO_2 and TiO_2_NSCS composites.

Sample	Crystallite size (nm)
TiO_2	12.0
NSCS2_ TiO_2 @850	8.2
NSCS3_ TiO_2 @900	9.9

5.3.1.2 TEM analysis of TiO_2 and TiO_2_NSCS

TEM analysis of TiO_2 and TiO_2_NSCS composite was done to understand the morphology that occurred. TiO_2 nanoparticles viewed from TEM were found to be highly agglomerated with non-

uniform and irregularities on the spherical shapes (**Figure 5.3** (**a**)). This was supposed to be as a result of annealing of TiO_2 nanoparticles at 450 ℃, which was done to improve its stability in photodegradation. Although the morphology of the TiO_2 nanoparticles obtained showed nearly spherical morphology, it is noteworthy to report that the observed particle size was found to be 12 nm as seen in the PXRD (**Figure 5.2). Figure 5.3** ((**b**) and (**c**)) depicts TiO_2_NSCS composites annealed at 850 and 900 ℃, TiO_2 nanoparticles were observed at the edges of NSCS spherical structures as shown in **Figure 5.3** (**c**). This is evident that the physical and chemical interaction of

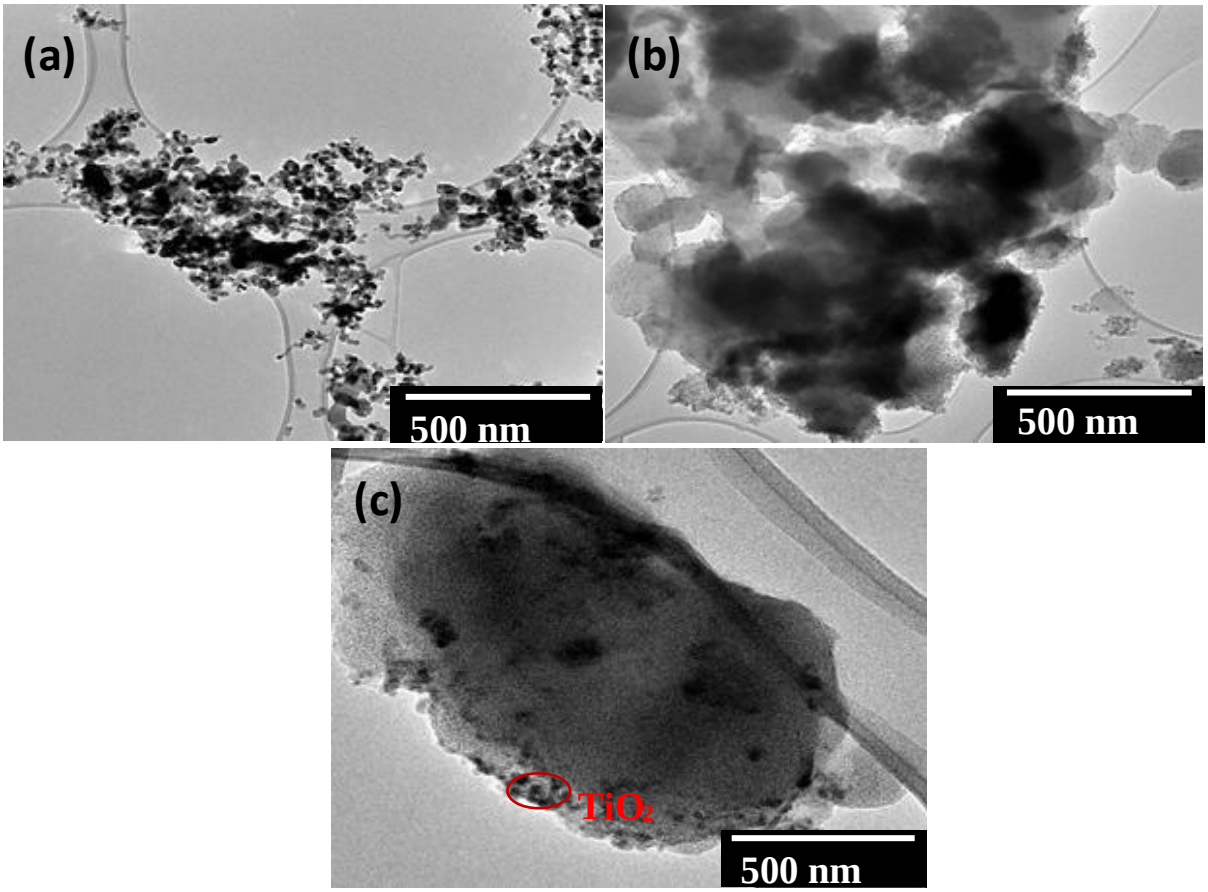

these materials took place. The uniform distribution of TiO_2 nanoparticles on NSCS material was found to be advantageous for photocatalytic application.

Figure 5.3: TEM micrograph of: (a) TiO_2, (b) NSCS_ TiO_2 @ 850 and (c) NSCS_ TiO_2 @ 900 ℃ composites.

5.3.1.3 SEM of TiO_2 and TiO_2_NSCS

To ascertain the surface structure of TiO_2 and its composites, SEM was studied. **Figure 5.4** (**a**) depicts agglomerated spherical-shaped TiO_2 nanoparticles with an average diameter of 12 nm. TiO_2 was prepared using the sol-gel method with vigorous stirring used to ensure a homogeneous mixture. The composites predominantly consist of light, and smooth surfaces representing TiO_2 nanoparticles. This was expected as above 90 % in the composite was TiO_2 (**Figure 5.4** (**b**) and (**c**)). However, the observed morphology of the composites showed no definite spherical shape. It is well known that the presence of carbon material inhibits the growth of TiO_2 particles as a result yields highly agglomerated nanoparticles [25]. In this research, it was seen that the composite images adhered to previous reports on physical and chemical interaction taking place between TiO_2 nanoparticles and NSCS during the hydrolysis process [25,26].

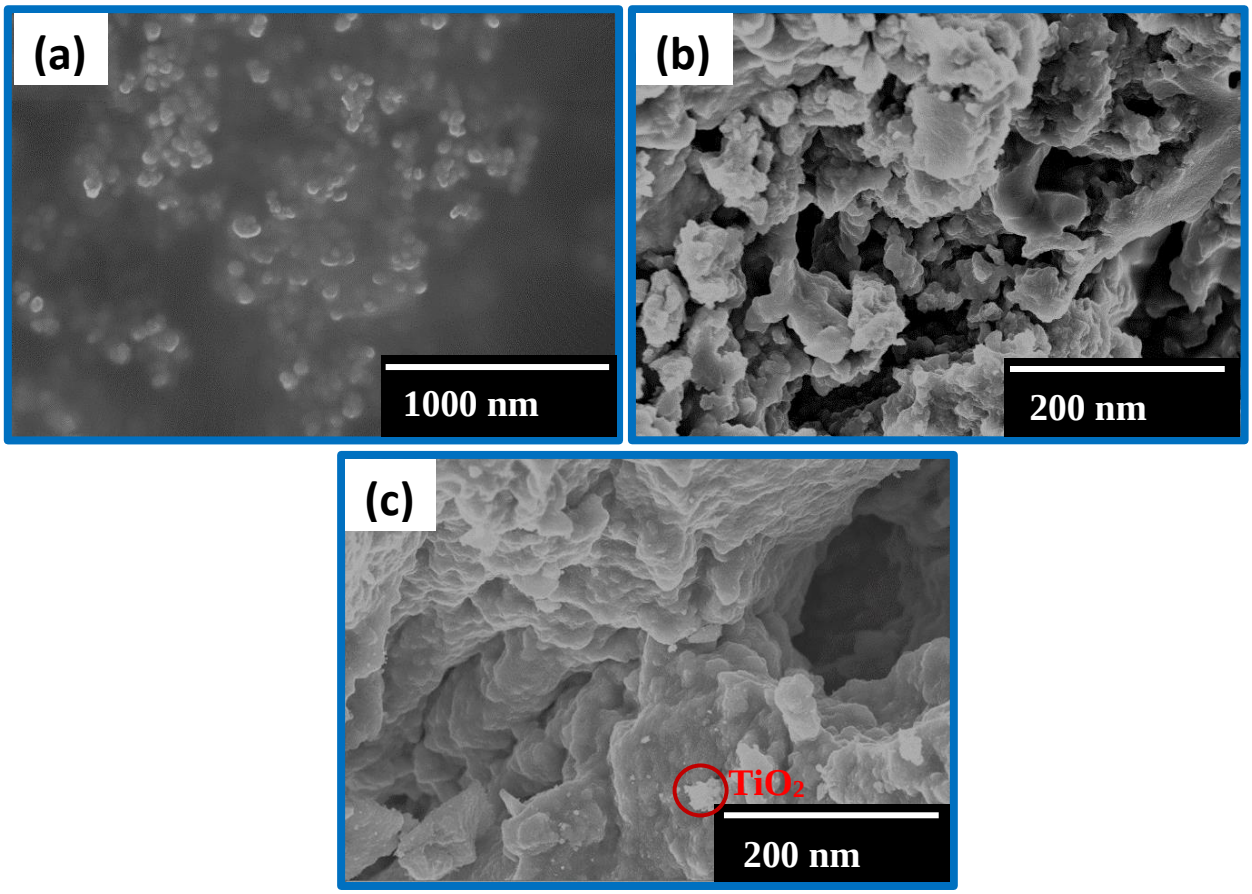

Figure 5.4: SEM of the synthesized (a) TiO_2, (b) NSCS_ TiO_2 @ 850, and (c) NSCS_ TiO_2 @ 900 ℃ composites.

5.3.1.4 FTIR Spectroscopy

Different types of covalent bonding of TiO_2_NSCS composites were investigated by the use of FTIR spectroscopy. **Figure 5.5** gives information on the pure TiO_2 with a broad peak observed at 710 cm^{-1}. The peak was assigned to Ti-O and Ti-O-Ti absorption bands. The two other absorption peaks were assigned to OH and O-H absorption bonds. TiO_2_NSCS composites annealed at 850 and 900 ℃ show incorporation of NSCS with TiO_2, this was supported by the presence of C=C, CH_2, CH, N=C=N, and N=C=S, and C-S functional groups [15,24]. The absorption peak at 755 cm^{-1} was assigned to the Ti-O-C functional group, which further confirms the interaction of TiO_2 with NSCS. Using FTIR gave an insight on the surface binding of TiO_2_NSCS composite while the interaction was seen between surface hydroxyl groups of TiO_2 particles to the NSCS material.

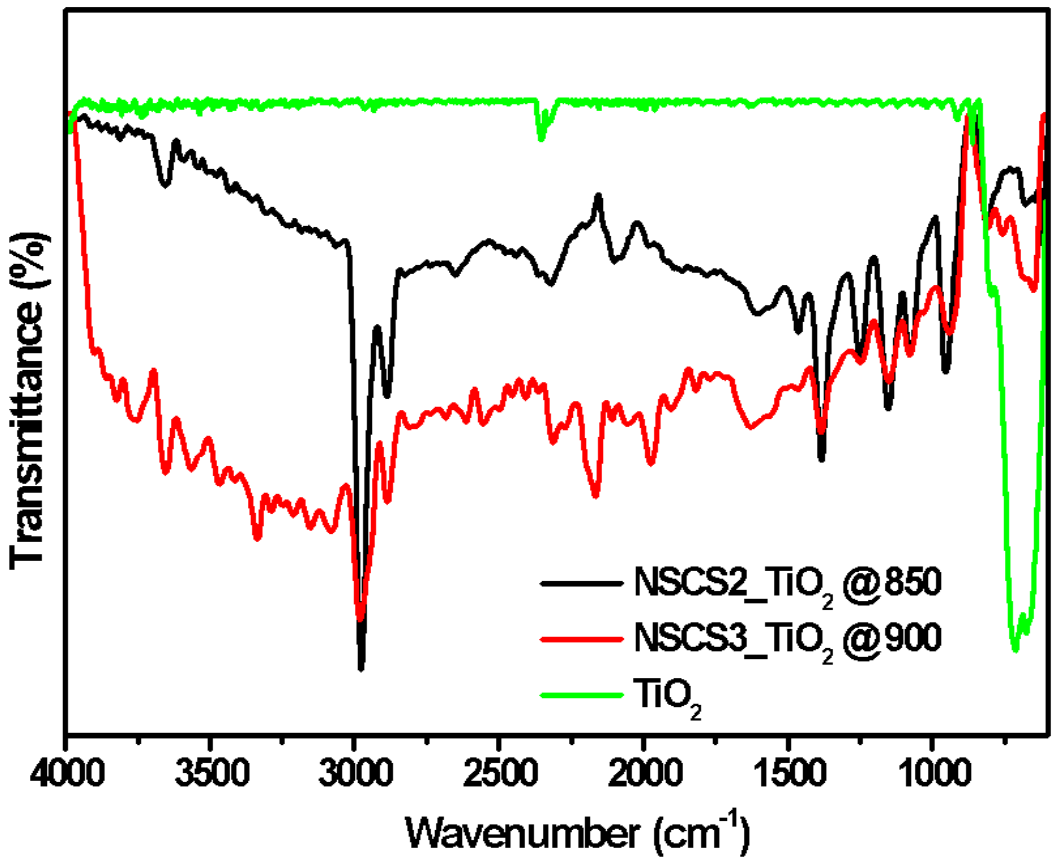

Figure 5.5: FTIR spectra of (a) TiO_2, (b) TiO_2_NSCS2 @ 850 ℃, and TiO_2_NSCS3 @ 900 ℃.

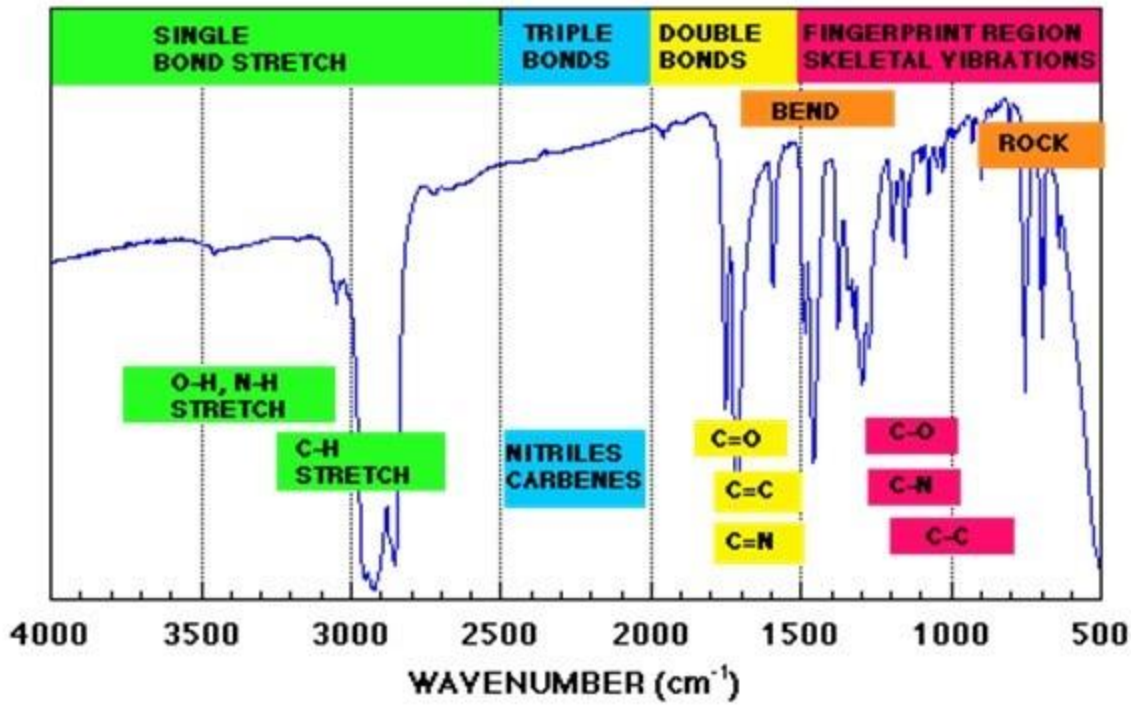

Figure 5.6: Interpretation of the FTIR spectra of the carbon material [24]

5.3.1.5 BET analysis

The specific surface area of TiO_2 and TiO_2_NSCS composites were investigated by BET technique. Nitrogen adsorption-desorption isotherms of TiO_2 and TiO_2_NSCS composites are shown in **Figure 5.7**. TiO_2 nanoparticles show a type 1 isotherm microporous, with a corresponding specific surface area of 51 m^2/g (**Table 5.2**). Both TiO_2_NSCS composites represent type IV mesoporous materials (**Figure 5.7** (**b**) and (**c**)) [20,26]. It was observed that the specific surface area of the composites decreases from 532 to 111.8 and 142 to 100 m^2/g for TiO_2_NSCS2 @ 850 and TiO_2_NSCS3 @ 900 composites, respectively. The decrease in specific surface area can be attributed to the carbon material blocking the pores of TiO_2 nanoparticles thus resulting in the decrease of the post-incorporation specific surface area of the TiO_2_NSCS composite. The obtained surface area and type IV isotherms enhance the surface of the composites to be able to adsorb more dye molecules during photodegradation [26]. Annealing the NSCS at different temperatures was observed in **Table 5.2** with an increase in pore size (4.48 and 6.61 nm) as the temperature was increased from 850 to 900 ℃.

Table 5.2: BET surface area of TiO_2 and TiO_2_NSCS composites

Sample	Surface area (m^2/g)	Pore volume (cm^3/g)	Pore size (nm)
TiO_2	51.2	0.308	24.09
TiO_2_NSCS2 @850	111.8	0.143	4.48
TiO_2_NSCS3 @900	100.0	0.165	6.61

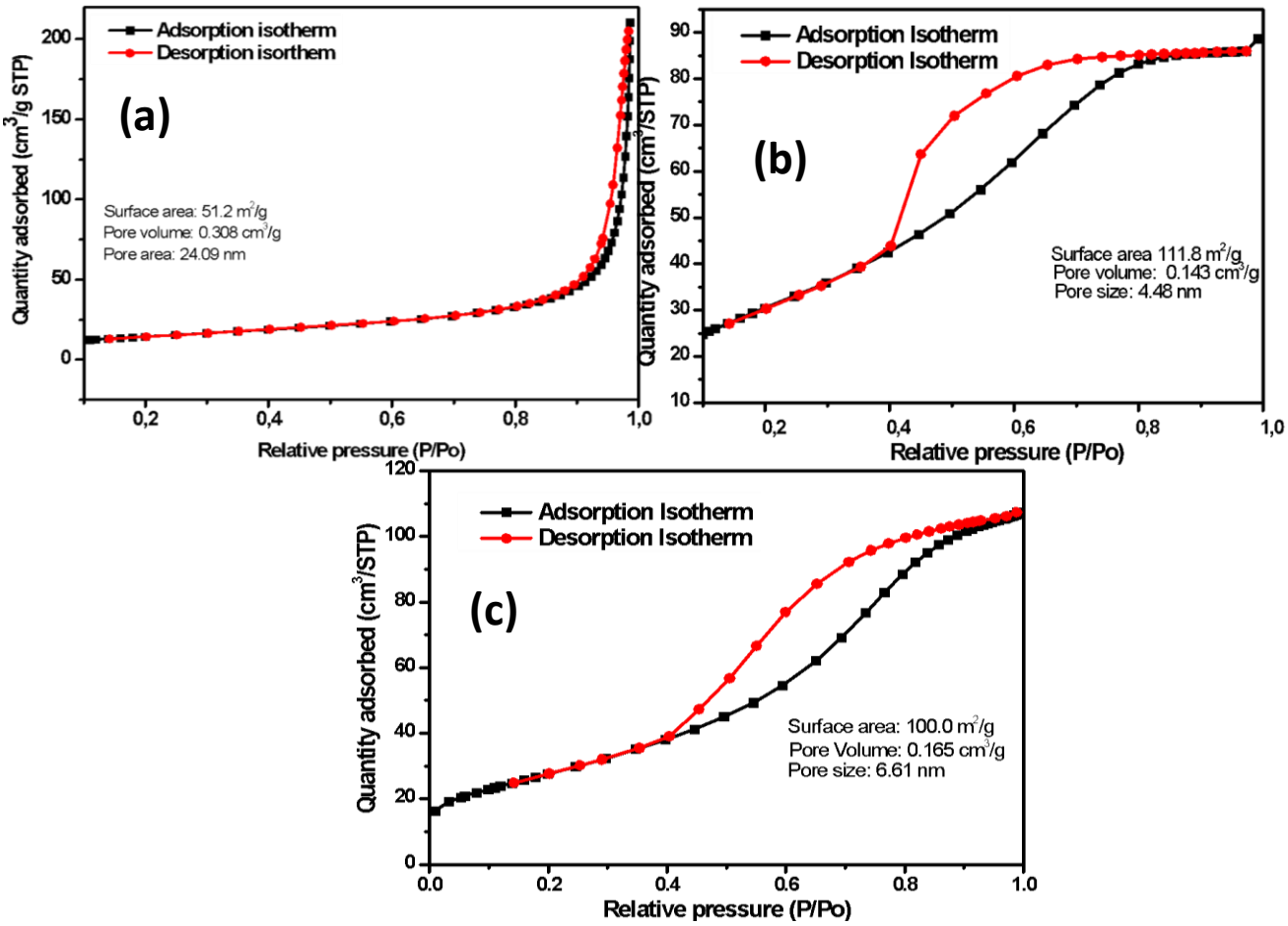

Figure 5.7: N_2 adsorption-desorption at 77 K of (a) TiO_2, (b) TiO_2_NSCS2 @850, and (c) TiO_2_NSCS3 @900 ℃.

5.3.1.6 Laser Raman spectroscopy analysis

In explaining the laser Raman spectroscopy of the incorporated composites, Raman active modes were considered as these play a role in confirming structural properties and thus helping to establish the relationship between TiO_2 and NSCS in terms of vibrational modes. Comparing the composite with NSCS was done to confirm the complete incorporation of NSCSs with TiO_2. It was observed that at wavelengths of 1380 and 1600 cm^{-1} being for D and G bands, respectively. In both spectra of the TiO_2_NSCS composites, carbon peaks are observed with no particular shift observed from that of NSCS alone reported in **Figure 4.11**. Laser Raman spectrum of TiO_2 showed four peaks at 195, 395, 524, and 637 cm^{-1} indexed Eg, B1g, A1g, and Eg respectively. These corresponds to the anatase modes [27]. In the spectra of both the TiO_2_NSCS composites, the four peaks of anatase phase TiO_2 were also observed with a blue-shift in the Eg peak. The blue-shifting in the Eg peak may be due to the presence of defects introduced by incorporation with the NSCS material [27]. Investigation of laser Raman spectra proved to be consistent with SEM, TEM, and PXRD results previously reported.

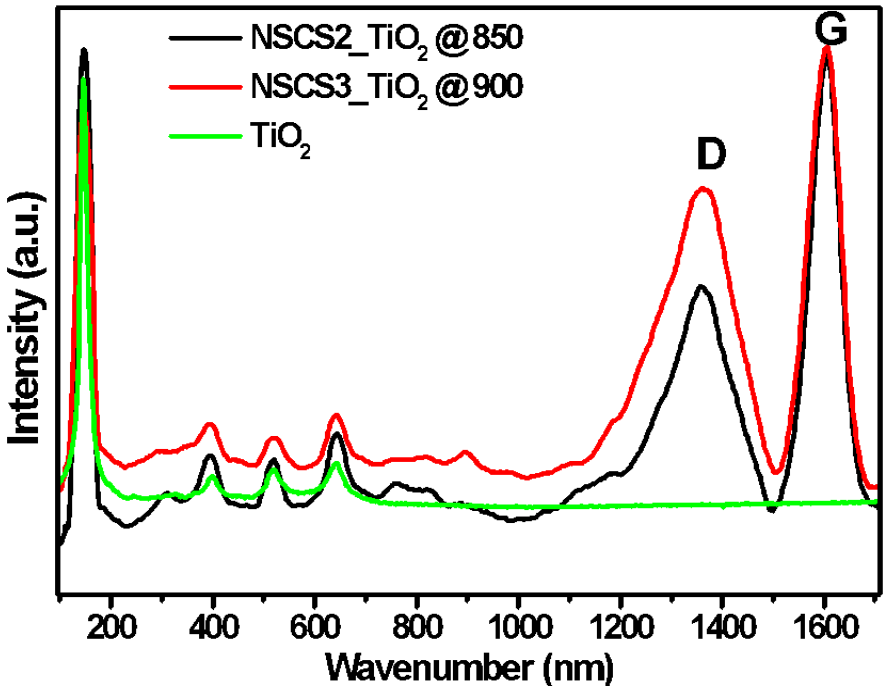

Figure 5.8: Raman spectra of TiO_2 and TiO_2_NSCS composites.

5.3.1.7 XPS elemental analysis

XPS analysis was done to understand the chemical bonding in the surface of the composites. **Figure 5.9** (**a**) reveals a chemical bond between Ti-O-C, where C bonds to one of the oxygen elements of TiO_2 enhancing the activity of TiO_2. Carbonaceous material has good electron-accepting properties, which in turn reduce fast electron-hole recombination [17,18]. Nitrogen, sulfur, and carbon were used in a study conducted by Li et al. [17] where under XPS they found different peaks of N, S chemical bonding with the C material. They concluded that each element bonds differently with TiO_2. Ti-O-N and Ti-N peaks at 400 eV and 397.3 eV, respectively were associated with nitrogen bonding, Ti-O-C peak at 288.8 eV was also obtained at different regions of the XPS spectrum [17,18]. In the XPS spectra **Figure 5.9**, it can be seen that N and S elements are not visible, this can be explained by their low amounts when quantified. It has been previously reported that the presence of nitrogen and sulfur heteroatoms can produce extrinsic defects on the composite thus improving the use of the synthesized composites [18]. **Table 5.3** provides the elemental quantification of the composites with their corresponding peak values. The atomic percentage of the composite equals 100 %, implying a lack of foreign compounds in the material

Table 5.3: XPS elemental analysis and quantification of TiO_2_NSCS.

Name	**Peak BE**	**Atomic %**
O 1s	529.4	47.5
C 1s	284.2	32.1
Ti 2p	458.0	20.4

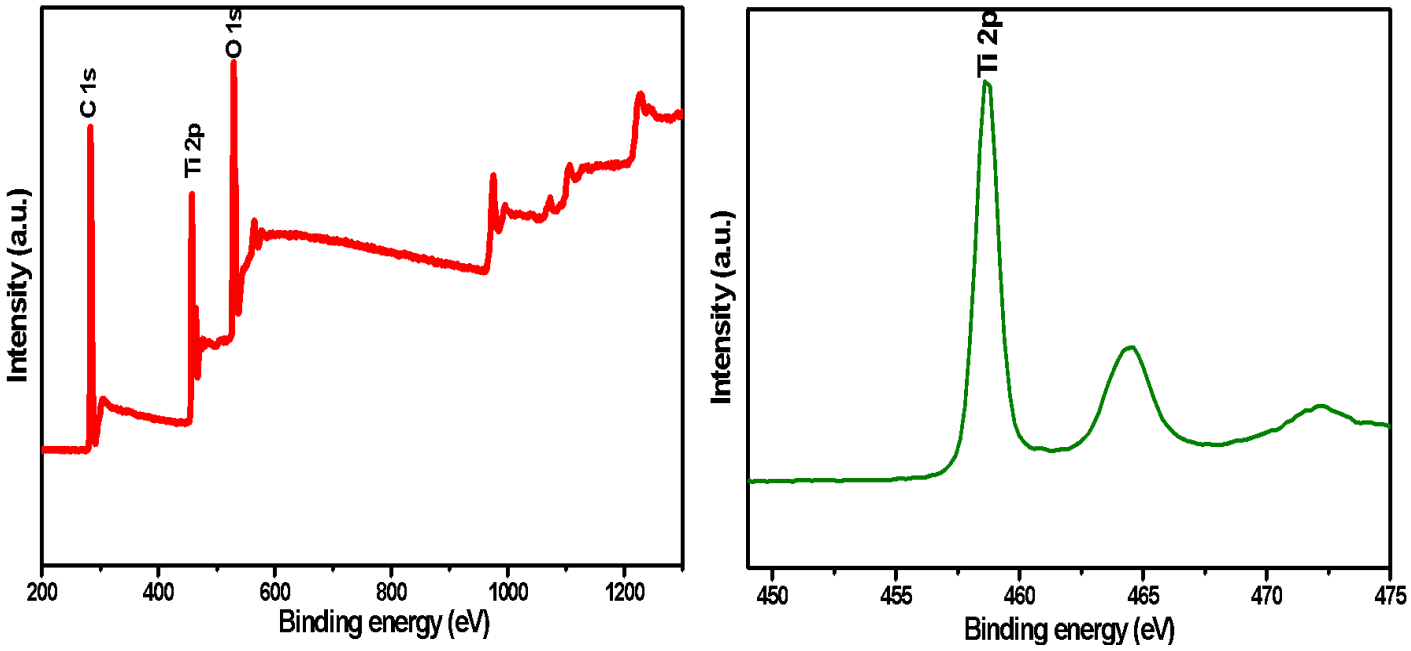

Figure 5.9: XPS of TiO_2_NSCS composites at different temperatures and that of Ti 2p.

5.3.1.8 TGA analysis

The TGA analysis were done to understand the thermal stability of the catalysts. Thermogravimetric analysis of NSCS annealed at different temperatures incorporated on TiO_2 was investigated as shown in **Figure 5.10.** The NSCS material that was used for TiO_2 showed a decrease in the combustion of NSCS as compared to that observed in **Figure 4.15**. The decrease was observed from ~640 ℃ to 417 ℃. This can be attributed to the presence of TiO_2 nanoparticles that catalyzed carbon oxidation. However, the thermal stability of the NSCS material becomes more stable as the synthesis temperature was increased from 850 to 900 ℃ (**Figure 5.10** (**a**)). The TGA profiles were also carried out to understand the amount of NSCS present relative to TiO_2 in the composite. It can be seen that approximately 5 % of NSCS loading was present in the TiO_2_NSCS composites.

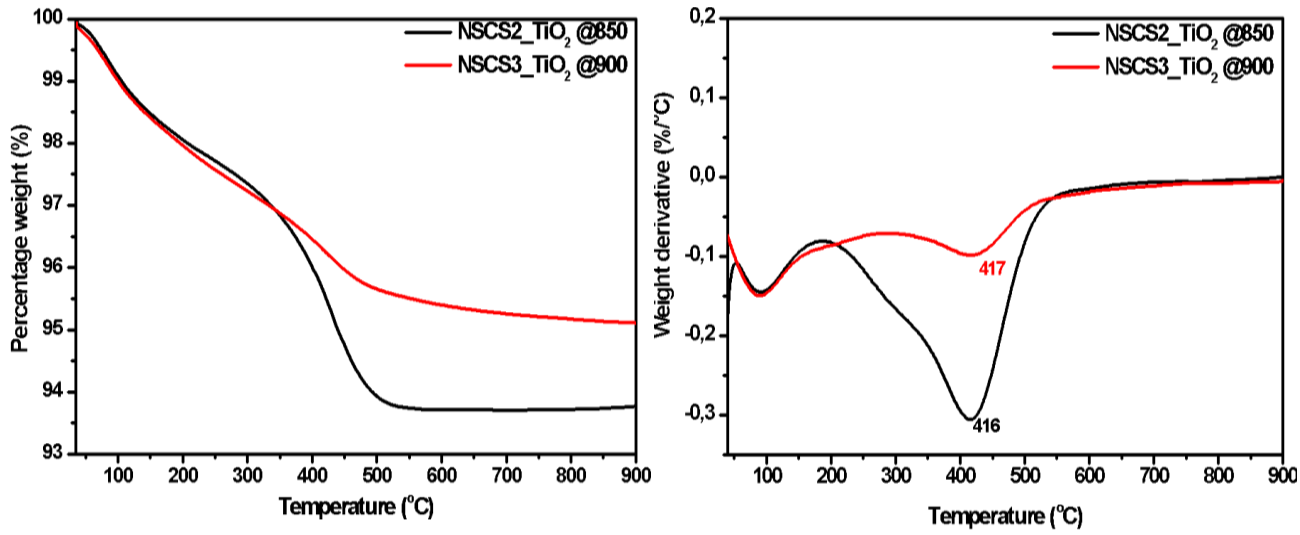

Figure 5.9: TGA of TiO_2_NSCS composites at different temperatures.

5.3.2 Photodegradation studies

$$\%D = \left[\frac{C_0 - C_t}{C_0}\right] \qquad \text{eq.5.1}$$

Where %D is the degradation efficiency, C_0 is the initial concentration at t_0, and C_t is the concentration at irradiation time under solar simulated light was used to calculate degradation efficiency. It is well known that carbon material at neutral pH (~7) adsorbs dye pollutants; however, at acidic and basic media, degradation of the dye pollutants is observed [28,29]. **Figure 5.11** represents photocatalytic degradation of NSCS in both acidic and basic media. In acidic conditions (pH4), the rate of degradation of the dye solution using the NSCS was observed to be slow, reaching 83 % conversion after 150 minutes. Under basic conditions, the degradation occurs at a faster rate with a maximum conversion of 82 % attained after 45 minutes (**Figure 5.11)**. This can be attributed to hydroxyl groups in basic media that are released from the suspension, allowing for better interaction between the NSCS and RhB dye. This observation results in faster reaction rate. However, as the irradiation time proceeded from 0 to 150 minutes some active sites in the NSCS were blocked by the accretion of the photocatalyst, as a result, the degradation of RhB increased slowly. Degradation efficiency was calculated using the equation above.

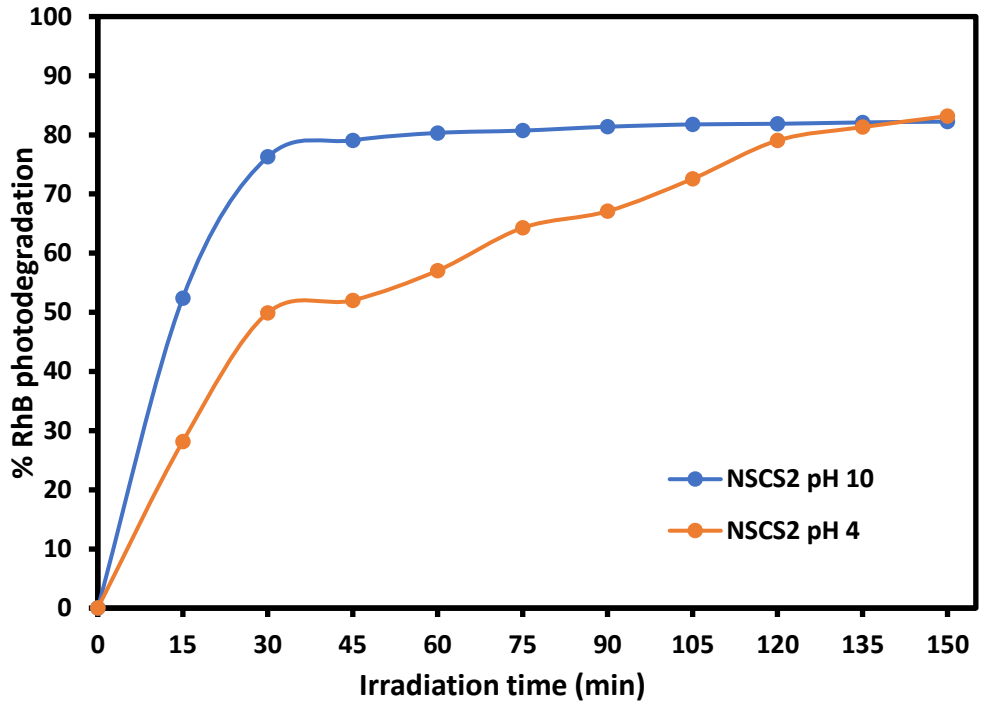

Figure 5.11: Photodegradation of NSCS synthesized at 850 ℃ in acidic and basic media.

This study investigated the use of various dye concentrations (1000, 500, 40, and 20 ppm) at a constant catalyst loading of 100 mg. **Figure 5.12** shows that at a dye concentration of 1000 ppm, the reaction rate is very low with 58% of the dye degraded during the reaction time of 150 mins. The plausible explanation for low degradation efficiency at high dye concentration is that the number of free radicals found in the solution from the catalyst is low, as a result, the high volume of RhB compound is not attacked by the catalyst. Also, at high dye concentration, the amount of light reaching the catalyst surface may be low due to the color intensity of the solution. While at low concentration, high photodegradation efficiency was observed as the photons that are traveling in the solution were increased with decreased dye concentration [23].

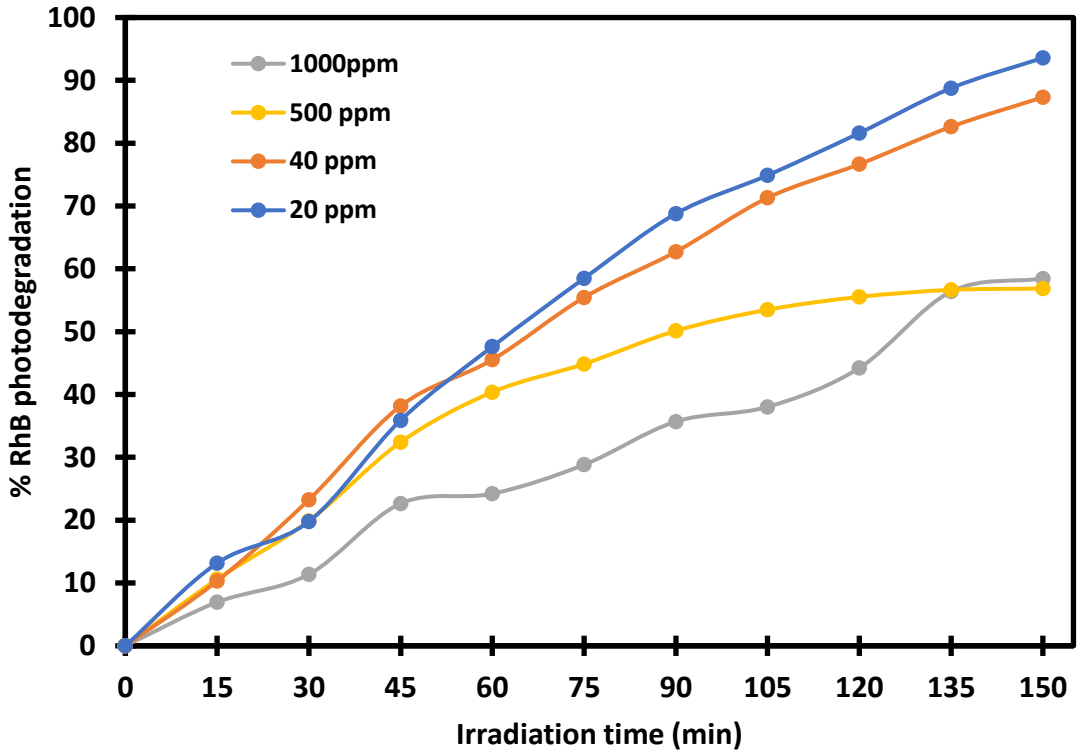

Figure 5.12: Variation of dye RhB concentrations at constant catalyst loading.

The photocatalytic activity of the synthesized composites materials in the degradation of RhB under simulated solar light is shown in **Figure 5.13**. It was observed that the photocatalytic activity of the as-prepared composites performs differently under solar simulator and visible light ($\lambda > 400$ nm). Similar conditions for the photocatalytic degradation of the composites were employed. In this work, NSCS material was varied based on the synthesis temperature employed and the mass ratio of the $ZnCl_2$ activating agent. The synthesized NSCS was then used as a support for TiO_2 and were further used for the degradation of RhB dye. **Table 5.4** shows 50 % catalyst conversions with respect to irradiation time. From this, it can be deduced that the catalysts with both TiO_2_NSCS2 @ 900 ℃, and TiO_2_NSCS2 @ 950 ℃ behaved differently in the RhB dye solution reaching a high irradiation time with low conversion. This implies that a fast photodegradation of these catalysts occurred reaching completion. The catalyst containing TiO_2_NSCS3 @ 900 ℃ showed moderate photocatalytic activity, with consistent irradiation time and conversion of RhB dye being observed. This was attributed to the synthesis temperature and the amount of activating agent affecting the behavior of the TiO_2_NSCS3 @ 900 ℃ catalyst. The following results,

therefore, focuses on the photocatalytic activity of TiO_2_NSCS3 @ 900 ℃ catalyst for further investigation of its photocatalytic properties.

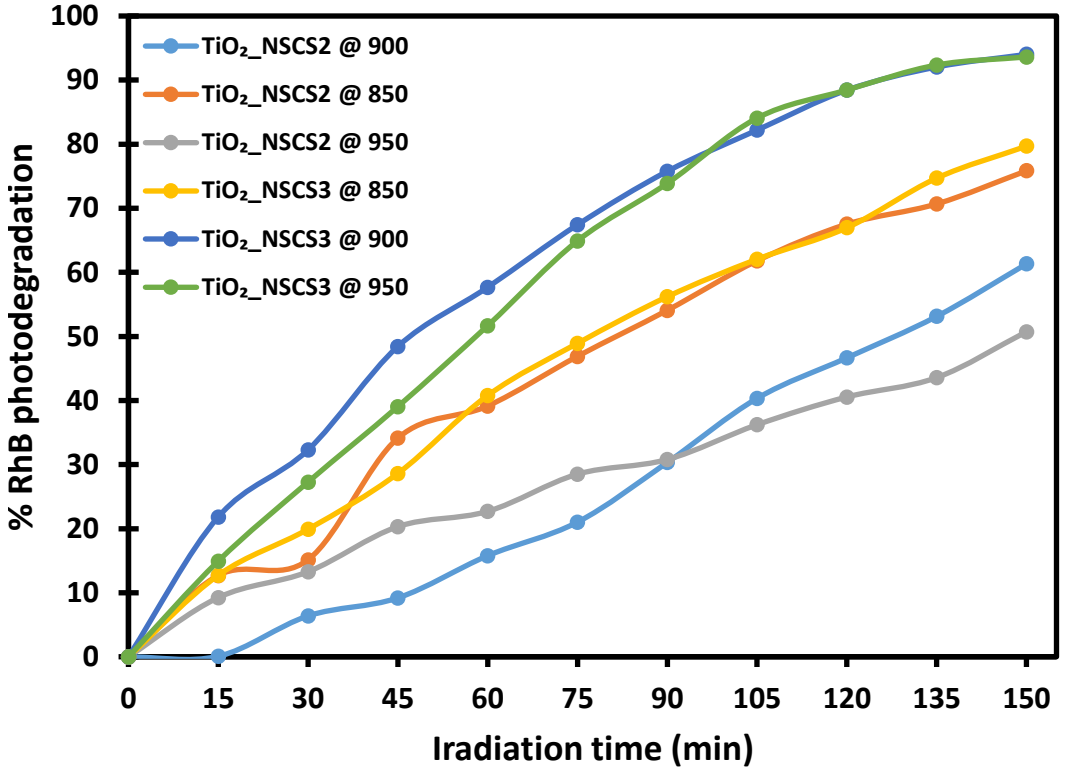

Figure 5.13: RhB degradation using TiO_2_NSCS photocatalyst prepared by sol-gel method in 15 minutes intervals.

Table 5.4: Percentage conversion of TiO_2_NSCS catalysts

Composite	**50 % conversions at various irradiation time (min)**
NSCS2_TiO_2 @ 850	74
NSCS2_TiO_2 @ 900	135
NSCS2_TiO_2 @ 950	130
NSCS3_TiO_2 @ 850	76
NSCS3_TiO_2 @ 900	45

NSCS3_TiO_2 @ 950	58

5.3.2.1 Optical studies: UV-visible Spectroscopy

The UV-Visible spectrum of bare TiO_2 and its composite showed a broad absorption in the region 312-380 nm shown in **Figure 5.14**. This absorption can be attributed to a transition from π bonding to $\pi*$ antibonding in the TiO_2 structure. TiO_2 is known to have an adsorption edge of 370 nm, change from this shows a redshift, confirming a decrease in the final bandgap of the material which was calculated using **eq. 5.4** [29].

$$E=hc/\lambda \qquad \text{eq. 5.2}$$

Where E, h, c, and λ are bandgap energy, Plank's constant, light velocity (ms^{-1}), and absorption wavelength (nm), respectively.

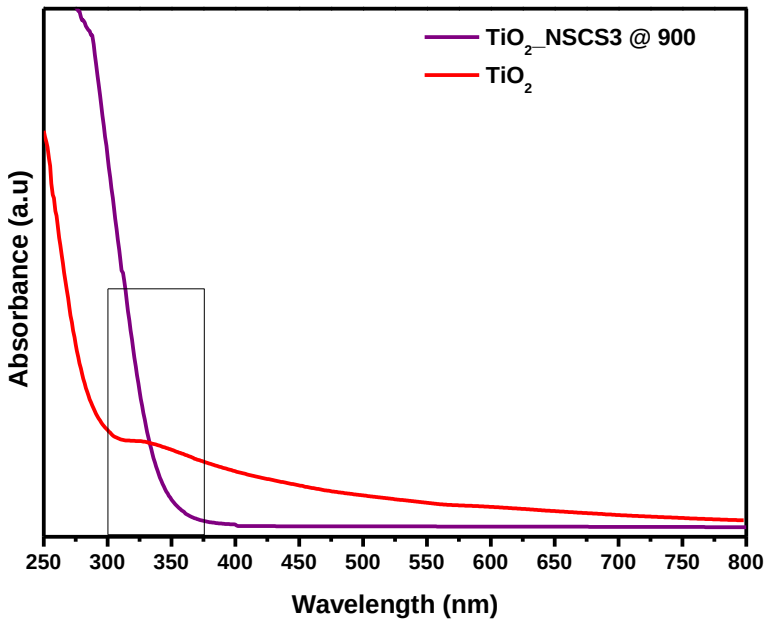

Figure 5.14: UV-visible of TiO_2 and TiO_2_NSCS3 @ 900 ℃.

To assess the effect of modification of TiO_2 with NSCS on its photocatalytic performance, the photocatalytic activities of bare TiO_2 and TiO_2_NSCS catalysts in the photodegradation of RhB solution were measured as shown in **Figure 5.15**. TiO_2 showed higher activity of 98 % with complete degradation of the dye after 60 minutes whilst TiO_2_NSCS reached 94 % conversion

only after 150 minutes. The high photocatalytic activity of TiO_2 can be attributed to the low concentration of bare TiO_2 in the RhB solution whereas TiO_2_NSCS catalyst has a higher concentration in the RhB solution. Additionally, bare TiO_2 can be accessed easily by the free hydroxyl radicals in the solution, while TiO_2 supported on NSCS may result in high number of solids in the solution even though the catalyst loading was the same [19]. TiO_2_NSCS composite synthesized at 900 ℃ achieved 94 % degradation efficiency of which was found to be comparable with TiO_2. In this study, it can be said that the synthesized TiO_2 follows an opposite trend from what has been reported in the literature, as a result, supporting TiO_2 with NSCS blocked some of the active sites decreasing the photocatalytic activity of TiO_2_NSCS catalyst [14, 19]. Some of the reasons that have been reported in literature include; 1) Formation of different structures when TiO_2 is doped with carbon have been explained to affect the electronic structure of the material [15]. 2) Different bonding types can occur during compositing TiO_2 with NSCS, including the substitution of both O and Ti atoms by C atoms, and the interstitial bonding, this was mostly explained by density functional theory (DFT) calculations [30]. The bare TiO_2 structure allows for the expansion of photocatalytic activity to the visible region of the solar spectrum [18]. Bare TiO_2 is transparent explaining its high degradation efficiency; on the other hand, carbon spheres are not as transparent, shielding the absorption light from the solar spectrum and reducing the degradation of the composite. Another reason for the poor efficiency of the composite may be a poor alignment of the carbon spheres with TiO_2 and unaccounted structural defects on the composite [14]. Poor alignment and presence of unaccounted structural defects in TiO_2_NSCS catalyst may result in NSCS material blocking the active sites found in TiO_2 surface, therefore, decreasing the photocatalytic activity of the catalyst.

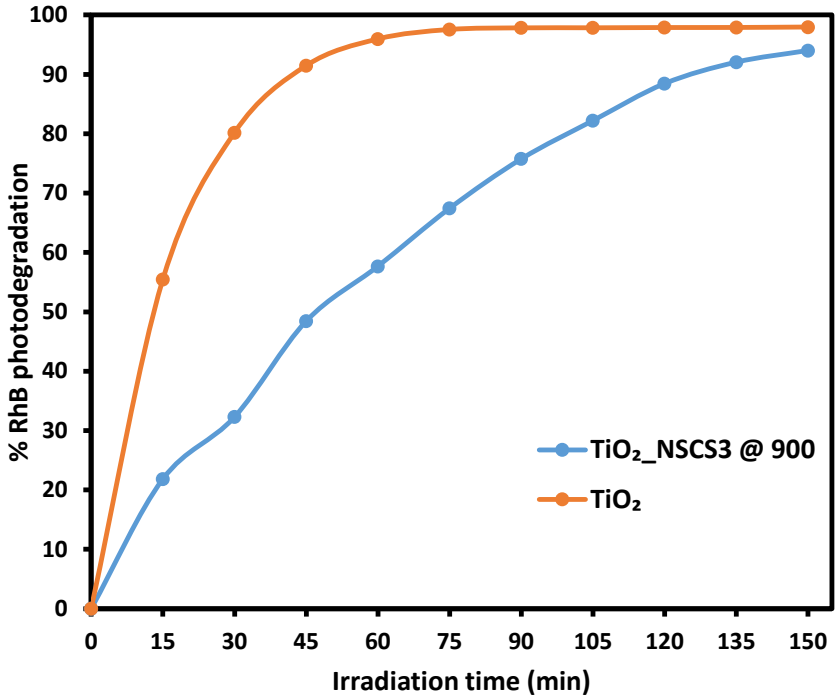

Figure 5.15: Comparison of the photocatalytic activities of TiO_2_NSCS and TiO_2 in the degradation of RhB.

The order of the degradation reaction was investigated by means of plotting a concentration to time graph, following the equation. In the equation, C_0 is the initial concentration, C_t is the concentration in respect to irradiation time, t is the time taken to irradiate, and k is the rate constant in seconds [31]. This gave more information about the rate of the reaction. Improvement of kinetics was a result of the introduced photocatalyst.

$$\ln(C_0/C_t) = kt \qquad \text{eq. 5.3}$$

The calculated correlation constant was found to be R^2 = 0.7981 and 0.9844 for TiO_2 and TiO_2_NSCS3, respectively. Consequently, the rate constant was found to be 7.19×10^{-4} and 2.69×10^{-4} s^{-1} for TiO_2, and TiO_2_NSCS3, respectively. The reaction constant was indicative of the slow reaction for TiO_2 catalyst that took place as the photocatalysts were used for the degradation of RhB dye [31]. It was also found that the degradation of RhB follows pseudo-first-order kinetics.

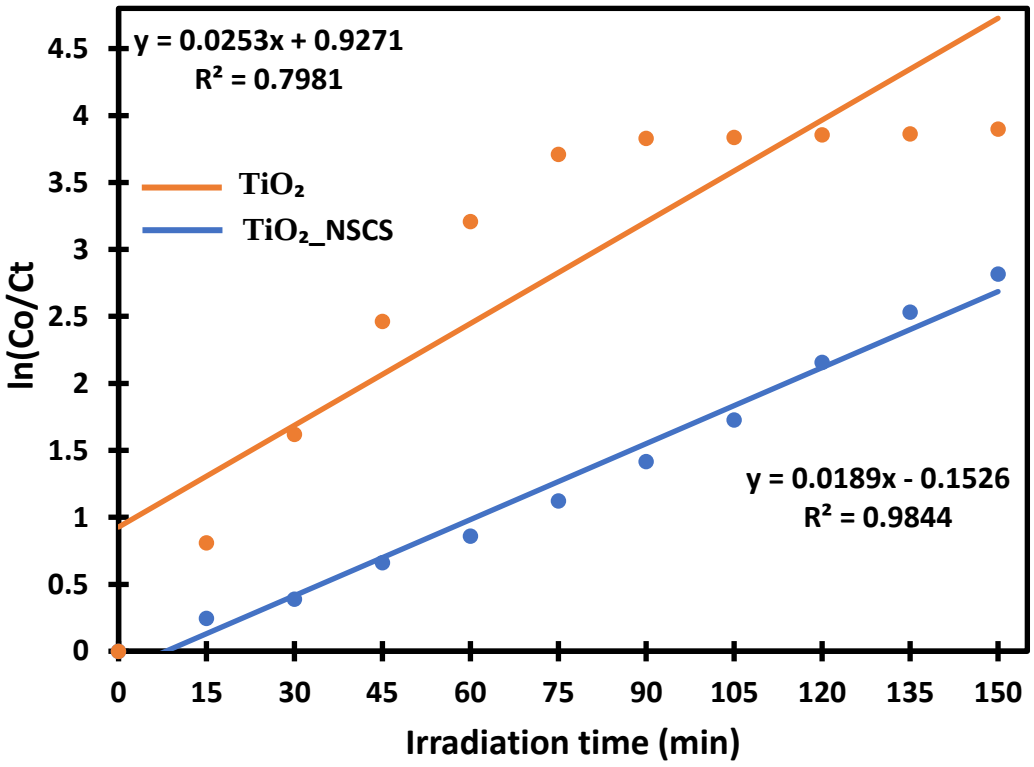

Figure 5.16: Plot of $\ln(C_0/C_T)$ versus irradiation time of TiO_2_NSCS with bare TiO_2.

5.3.2.2 Optimization of photocatalytic conditions

5.3.2.2.1 Catalyst loading effect

The effect of the amount of catalyst used in the reaction was studied to determine the optimum catalyst amount to be used for the reaction. **Figure 5.17** shows the RhB conversion as a function of the mass of catalyst used ranging from 5 to 25 mg for 50 ml of 10 mg/L RhB solution. There is an increase in the RhB conversion rate with an increase in the amount of catalyst from 5 to 10 mg, beyond the conversion rate a decrease is observed. The increase in conversion rate can be attributed to the increase in the number of catalyst active sites as the catalyst amount increases. Correspondingly, there is easy access for RhB molecules to be adsorbed during photodegradation. The decrease in conversion rate is due to the high amount of turbidity in the suspension blocking the active sites of the photocatalyst resulting in low photocatalytic activity [32]. Based on the

reports by previous studies, a plateau is reached as the mass of the catalyst is added to the suspension of the pollutant leading to blockage of light penetration by the particles of the photocatalyst [1,22,32]. Herein, optimum mass loading of the photocatalyst was reached with 10 mg showing the highest degradation rate.

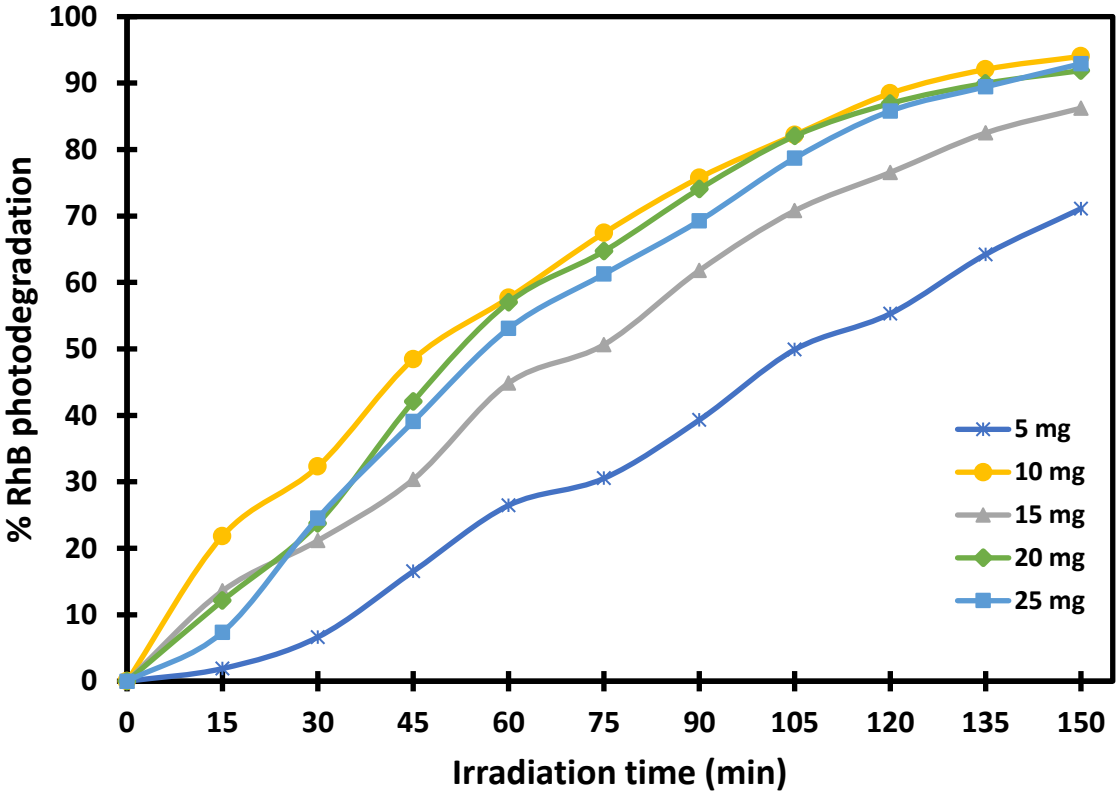

Figure 5.17: The effect of mass loading of the photocatalyst at 10 ppm dye concentration.

5.3.2.2.2 Effect of dye concentration

Variation of initial dye concentration was investigated using 5, 10, 15, 20, 25, and 30 ppm with the pH of 7 and catalyst loading of 10 mg being kept constant (**Figure 5.18**). An inverse relationship of the initial dye concentration with degradation rate was observed; an increase in the amount of RhB concentration leads to a decrease in degradation efficiency of the photocatalyst. With a low initial RhB concentration (5-15 ppm) the trend follows pseudo-first-order kinetics as seen in **Figure 5.16.** Ease access to the active sites of the catalyst allows for the absorption of RhB molecules to the surface of the catalyst. While an increase in initial RhB concentration (20-30 ppm) results in a screening effect where the RhB molecules are adsorbed on the surface of the

composite. This has been inferred to zero-order kinetics as a result of the inverse relationship between the initial RhB concentration and the degradation rate. Similar observations have been reported in the degradation of methyl orange, phenol, and methyl red [1].

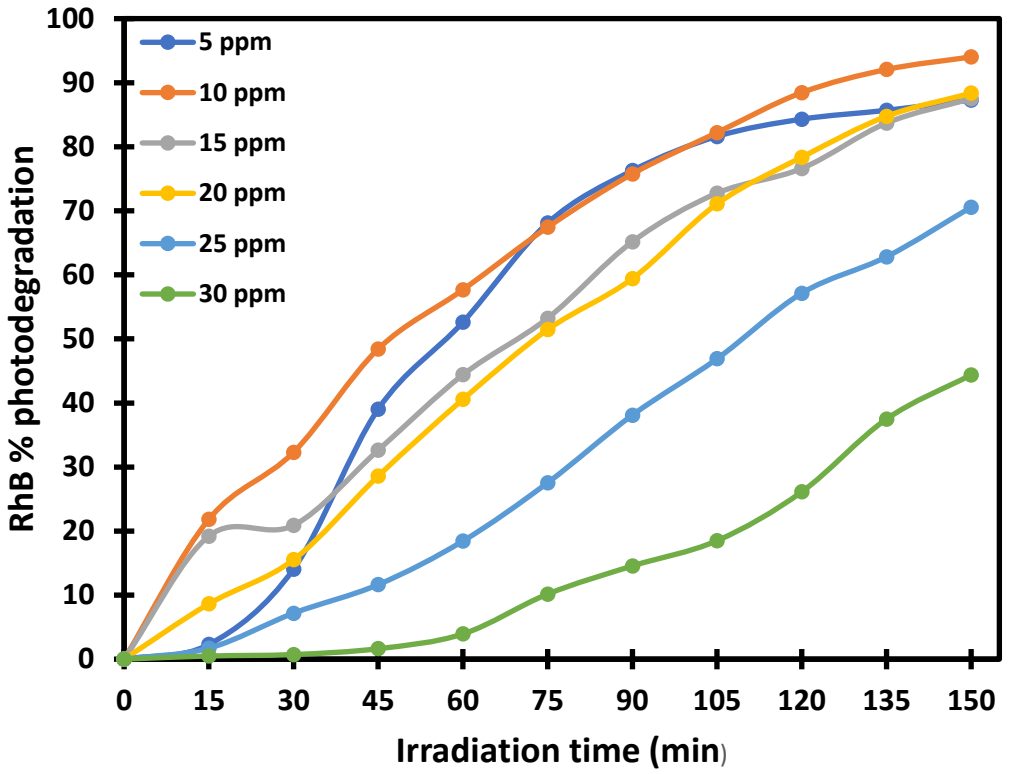

Figure 5.18: The effect of initial RhB concentration at constant pH 7 and catalyst loading of 10 mg.

5.3.2.2.3 Effect of pH

The effluent of wastewater from textile industries can be discharged at different pH, hence the study of the effect of initial pH was conducted in ranges 2-10. **Figure 5.19** shows the effect of pH on the reaction mixture of the rate of degradation of the dye with pH 7 being the optimum pH. At acidic media, it was observed that the catalyst behaves better, however, still lower than pH 7. This is due to more protons (H^+) being absorbed in the suspension by the surface of the photocatalyst. A similar trend is observed at basic media, with pH 8 and 10 performing at lower than pH 7. It has been reported that RhB in water exists in two states, the RhB^+ which is cationic, and the $RhB^{\pm}$ which is a zwitterion. In this case, the initial pH of the suspension was basic, and the final

suspension was neutral (pH 7), implying that protons are consumed in the suspension [33]. Overall, the starting suspension can be observed in both media (acidic or basic), however, the final solution observed was neutral confirming the degradation of RhB when using TiO_2_NSCS catalyst while obtaining more information about the remaining compounds after 15 minutes of degradation. pH7 > pH10 > pH2 trend was observed, this means acidic effluents are difficult to treat under solar simulated light. This was elaborated by observing the initial pH of the acidic solution (2) and the final solution observed was neutral (pH 7).

It has been reported that TiO_2 alone has a point zero charge (pH_{zpc}) of 6.25, as a result at pH below 6, TiO_2 is positively charged whereas above pH 6 it is negatively charged (**eq. 5.7)** [33]. This implies that varying pH will have an impact on the degradation of the photocatalyst, which was the current observation in this study. Likewise, RhB has a pKa value of 4.2. Point zero of TiO_2 is 6.25, from the below equations when degrading RhB in acidic media implying pH below point zero there is not much separation of the photocatalyst, however, in basic media H_2O is separated.

$$pH<Pzc: TiOH^{+} H^{+} = TiOH_2 \quad \text{eq. 5.4}$$

$$pH>Pzc: TiOH^{+} OH^{-} = TiO^{-} + H_2O \quad \text{eq. 5.5}$$

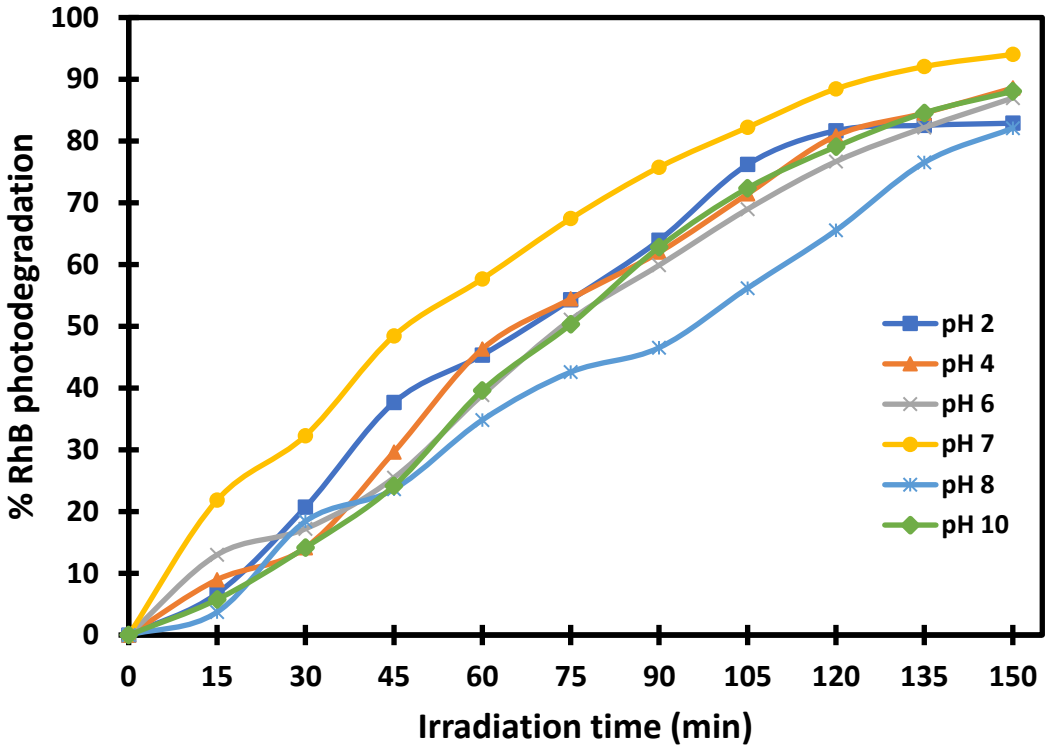

Figure 5.19: Effect of pH on the reaction mixture of the rate of degradation of RhB in 15 minutes intervals.

5.3.3 High performance Liquid Chromatography-Mass Spectrometry (HPLC-MS)

Figure 5.20 the HPLC-MS technique was done post-treating RhB, where analysis of formed intermediate products was investigated. In both **Figures, 5.20** ((**a**) and (**c**)) shows a sharp, intense peak at 443 m/z which was attributed to the RhB compound being dominant at the start of a reaction (T0). This can be elaborated by the abundant RhB concentration in the solution which shows the stability of RhB before exposure to visible light. The degradation of the RhB compound took place after 150 minutes (**Figure 5.20** (**b**) and (**d**))**.** The presence of N-demethylated intermediates has been previously reported to confirm the degradation of RhB compound into less harmful products when exposed to visible light [31,32]. Furthermore, the disappearance of the chromophore in the fragmented products implies the effective degradation of RhB. Chromophores are aromatic groups in the dye compound [33]. The intense peaks were seen in **Figure 5.20** (**a**) and (**c**) were reduced with longer exposure to visible light while various N-demethylated intermediates peaks become more intense. Degradation of RhB dye in the presence of TiO_2 photocatalyst can be explained to occur as the ·OH, radicals become more abundant in the solution,

breaking down the aromatic rings in the RhB compound decolorizing the solution. While with NSCS_ TiO_2, the C=C double bonds from the carbon material assist ·OH, radicals into breaking down the RhB compound, as a result, breaking down the compound to smaller inorganic salts (i.e., $C_2H_6O_2$ – 62 m/z). This peak was observed to be only intense in the HPLC-MS spectra of NSCS_ TiO_2. Additionally, confirming previous reports on supporting TiO_2 with carbonaceous materials were explained to be preferable as they assist on the cleavage of azo bonds in RhB compound under simulator solar light. Muthavel and Swaminathan proposed the mechanism that took place during the mineralization of RhB (**Figure 5.21**) [27].

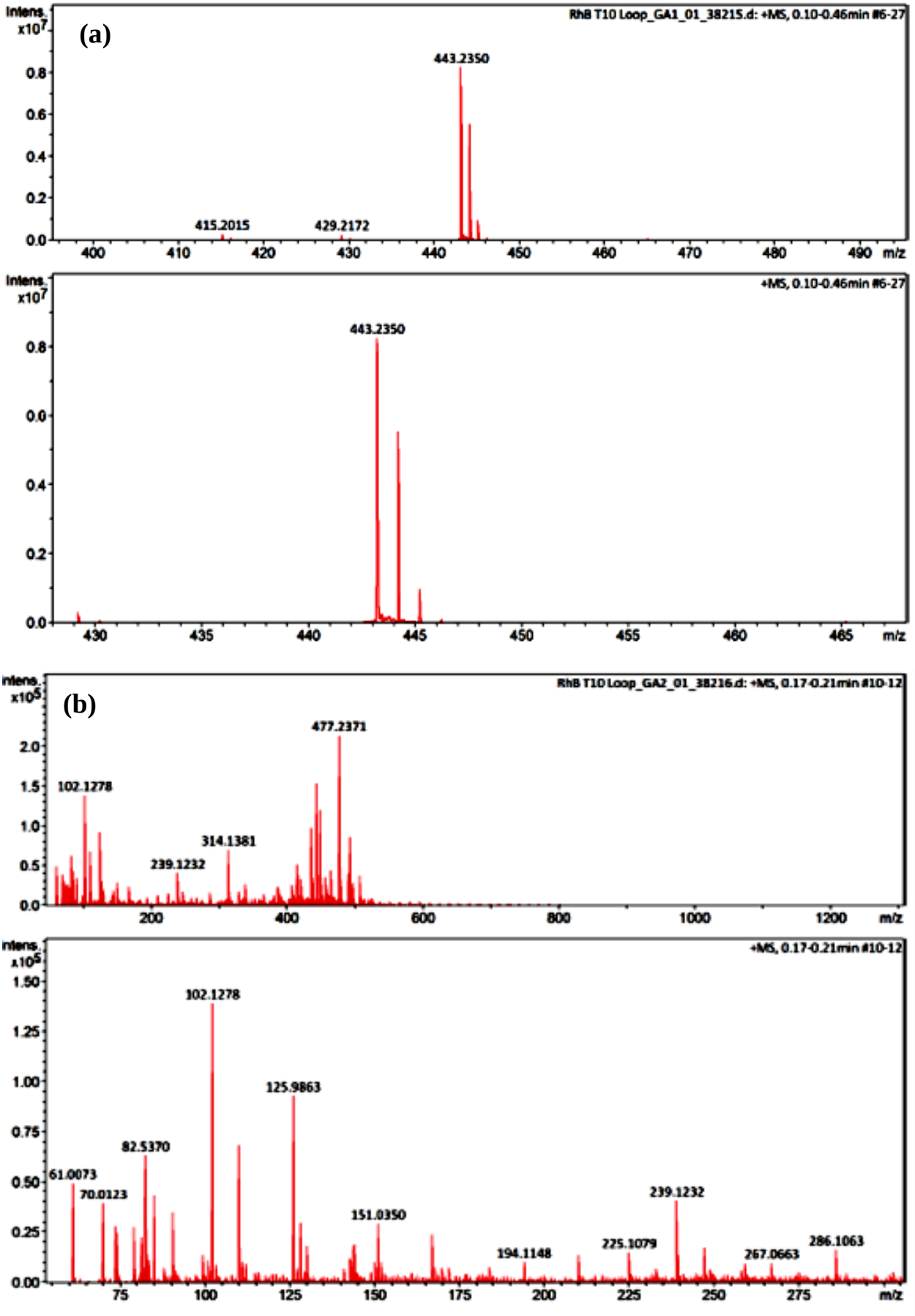
(a)
RhB T10 Loop_GA1_01_38215.d: +MS, 0.10-0.46min #6-27
Intens.
x10^7
443.2350
415.2015
429.2172
m/z
+MS, 0.10-0.46min #6-27
443.2350
(b)
RhB T10 Loop_GA2_01_38216.d: +MS, 0.17-0.21min #10-12
Intens.
x10^5
477.2371
102.1278
314.1381
239.1232
m/z
+MS, 0.17-0.21min #10-12
102.1278
125.9863
82.5370
61.0073
70.0123
151.0350
239.1232
194.1148
225.1079
267.0663
286.1063

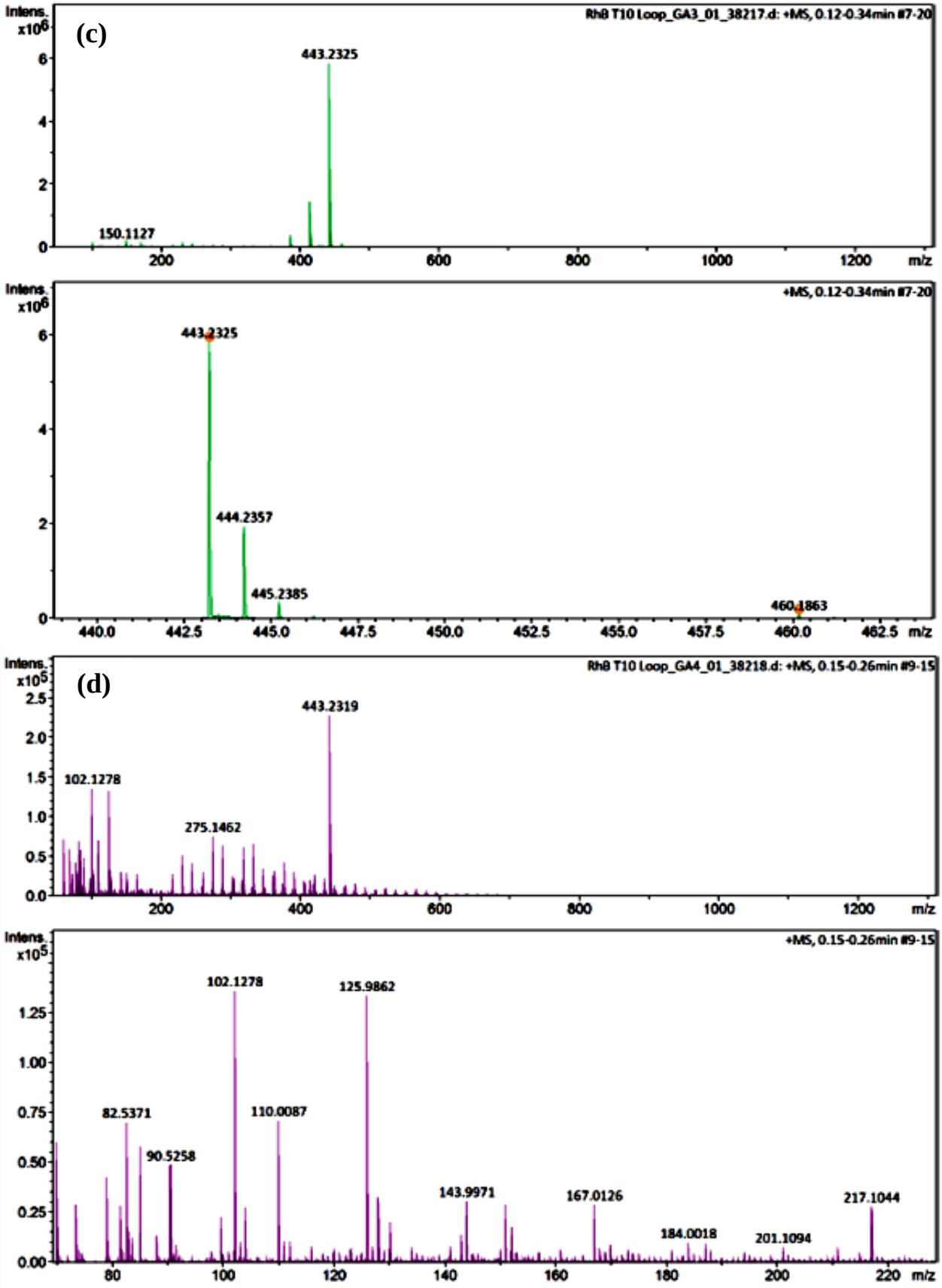

Figure 5.20: a) HPLC-MS of (a and c) TiO_2_NSCS and bare TiO_2 before exposure to visible light and (b and d) TiO_2_NSCS and bare TiO_2 after exposure to visible light for degradation of RhB.

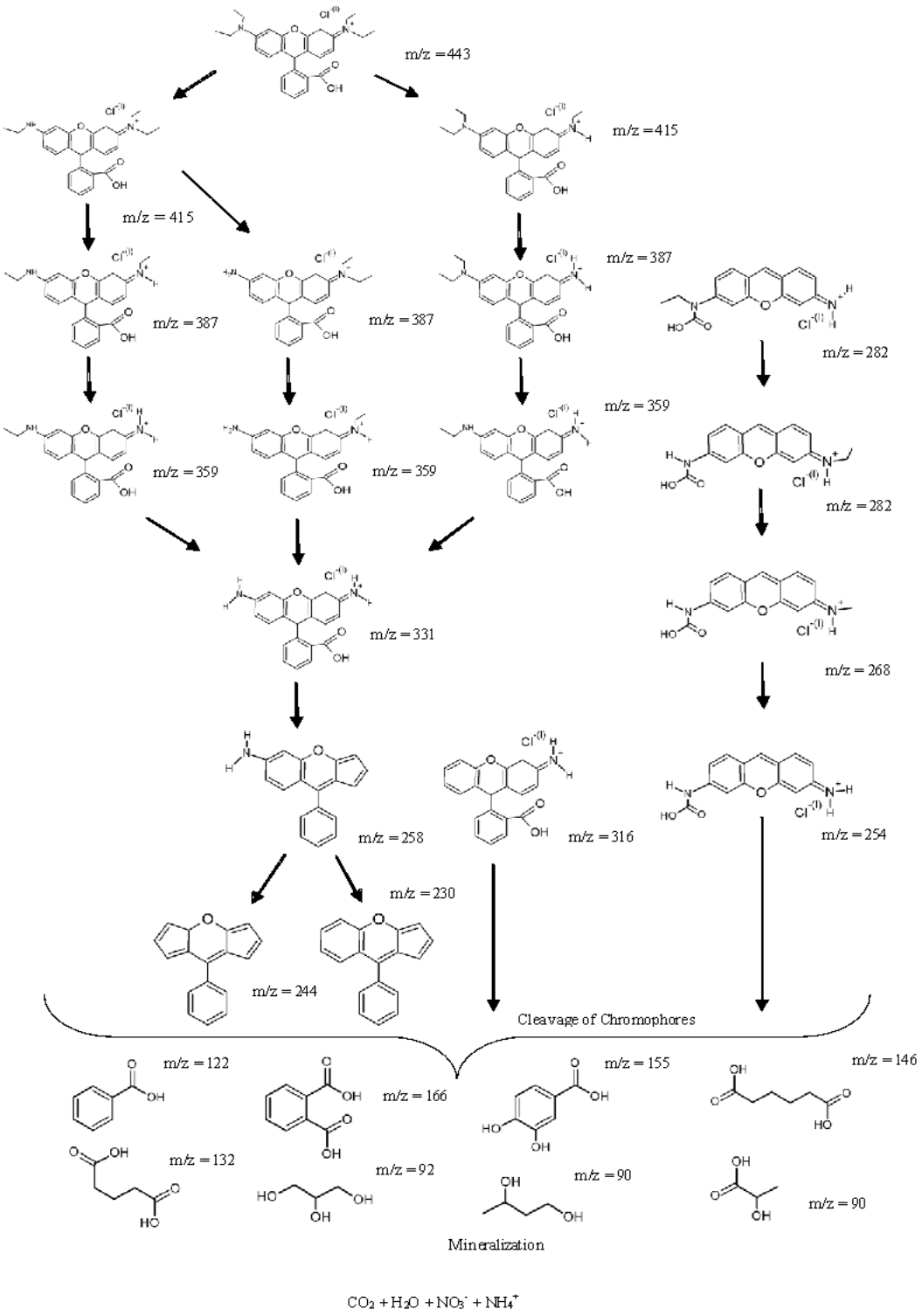

Figure 5.21: Mechanism of the photocatalytic mineralization of RhB [27].

5.4 Proposed mechanism

A possible photodegradation mechanism of TiO_2_NSCS composite under solar light irradiation was reported by Baca et al., for RhB decomposition utilizing CS_TiO_2 composite [8]. **Figure 5.22** represents a modified representation of the possible photodegradation of TiO_2_NSCS composite under simulator solar light**.** It is well-known that the reaction mechanism process starts with free radicals attacking the pollutant dye and thus increasing the rate of reaction. Hence, the fast recombination of electron-hole inhibits the rate of reaction during the degradation. In the proposed mechanism, it was observed that holes found in the valence band were trapped by oxygen species on the surface where some holes diffuse to the oxygen sites [33]. Electron in the conduction band was then transferred to the NSCS support material. The electron-hole pair was hindered from pairing due to the presence of H_2O and NSCS. The synergistic effect of incorporating TiO_2 with NSCS was improved as the color change was observed from pink to colorless. However, the non-toxic by-products that were observed from HPLC-MS as a result of mineralization of RhB provided evidence that change of pink color to colorless implied that decomposition of RhB took place.

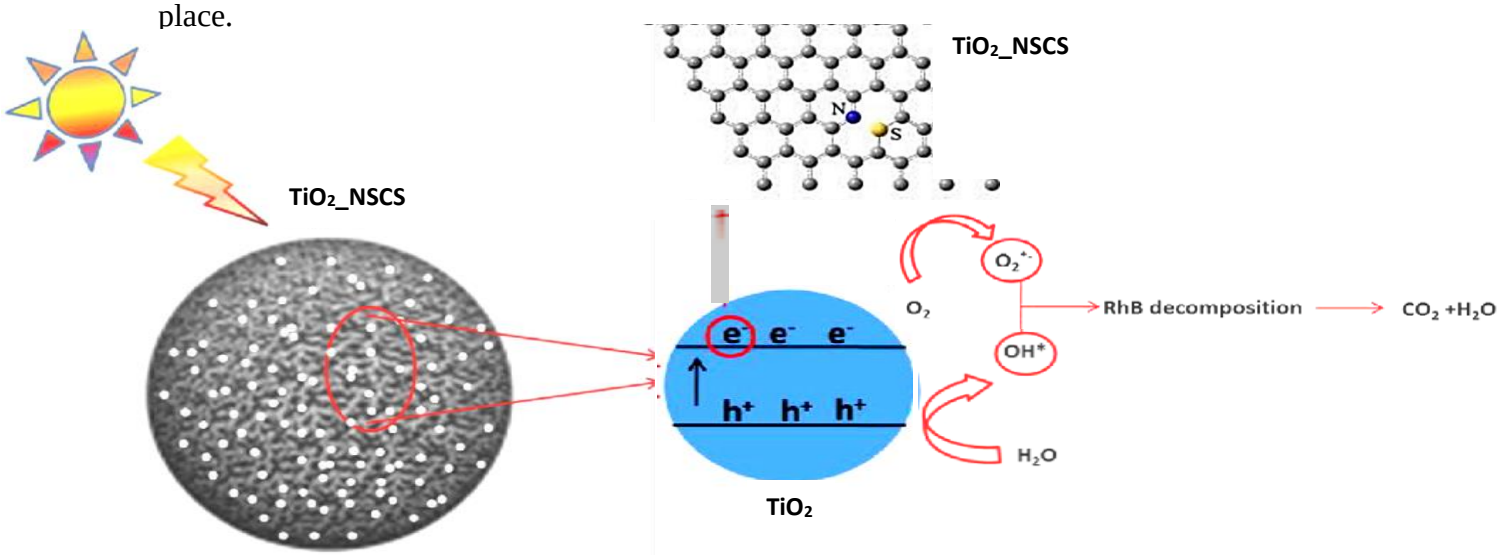

Figure 5.22: Mechanism of the photocatalytıc mıneralization of RhB [8].

5.5 Conclusion

This chapter investigated the effect of modifying TiO_2 with NSCS which was synthesized via the sol-gel method. The interest behind employing NSCS material that was obtained from natural material (onion), was the presence of N, S, and C elements being obtained in one precursor. NSCS study involved the effect of temperature on NSCS nanoparticles. The temperature at which the NSCS was prepared when incorporated with TiO_2 showed no particular trend on its effect on the activity of the resulting catalyst. The amount of NSCS incorporated into the TiO_2 had a major effect of the catalyst performance. The probability of carbon material being optically non-transparent as TiO_2 is incorporated was found to be high. However, incorporating less than one percent of NSCS on TiO_2 allowed for light transparency as applied under the solar simulator. Structural properties of TiO_2 and NSCS_ TiO_2 composite were investigated by PXRD, SEM, TEM, FTIR, Laser Raman spectroscopy, BET, TGA, and XPS. The synthesized NSCS_ TiO_2 composite was observed to consist of a high specific surface area. The incorporation of TiO_2 onto NSCS was observed when the morphology of the composite was investigated. This was consistent with broad peaks and blue-shifting of peaks that were observed in both PXRD and Laser Raman spectroscopy.

Optical properties were investigated using UV-Vis spectroscopy. The obtained results proved to be similar with regards to the synthesized TiO_2_NSCS, even though some active sites of TiO_2 were blocked, hindering 100 % degradation efficiency. It can be concluded that the use of green renewable element precursors has to be further improved and developed before its application in photocatalysis. The interaction of RhB and the photocatalyst was found to be of paramount importance. This can be observed by optimizing the operational parameters of the catalysts that are catalyst loading of 10 mg, dye concentration of 10 ppm, and pH 7. It was observed that above optimum conditions low conversions during photodegradation were obtained. TiO_2_NSCS catalyst contributed little to improving the degradation efficiency of TiO_2 relative to pure TiO_2. HPLC-MS showed improved degradation of RhB in water suspension in the composite as compared to TiO_2. However, there are limited studies that focus on the degradation of the organic dyes in solutions in the presence of carbon materials/TiO_2.

5.6 References

1. Jo W.-K. & Tayade R.J. Recent developments in photocatalytic dye degradation upon irradiation with energy-efficient light-emitting diodes. Chinese Journal of Catalysis. (2014); 35: 1781–1792.
2. Priyaragini S., Veena S., Swetha D., Karthik L., Kumar G. & Bhaskara Rao K.V., et al. Aquatic environment. Environ Sci, (2014); 26: 775.
3. Shaban M., Ashraf A. M. & Abukhadra M.R.TiO_2 Nanoribbons/Carbon Nanotubes Composite with Enhanced Photocatalytic Activity; Fabrication, Characterization, and Application. Scientific reports (2018); 8:781.
4. Chen H., Shen M., Chen R., Dai K. & Peng T. Photocatalytic degradation of commercial methyl parathion in aqueous suspension containing La-doped TiO_2 nanoparticles. Environmental Technology. (2011); 32(13): 1515–1522.
5. Liu Y.J. & Claus R.O. Blue light emitting nanosized TiO_2 colloids. Journal of the American Chemical Society 119 (1997); 119: 5273–5274.
6. Dvoranová D., Brezová V., Mazúr M. & Malati M.A. Investigations of metal-doped titanium dioxide photocatalysts. Appl Catal B Environ. (2002); 37(2):91-105.
7. Das R. Nanohybrid Catalyst based on Carbon Nanotube. Carbon Nanostructures Springer International Publishing AG. (2017).
8. Baca M., Wenelska K., Mijowska E., Kaleńczuk R.J. & Zielińska B. Physicochemical and photocatalytic characterization of mesoporous carbon/titanium dioxide spheres. Diamond & Related Materials. (2020); 101: 107551.
9. Alexander M. & Pandian K. Carbon sphere-assisted preparation of TiO_2 hollow nanospheres and its electrocatalytic reduction of H_2O_2, oxidation of antioxidants and ethanol sensor. J Solid State Electrochem (2013).
10. Srinivasu P., Singh S.P., Islam A. & Han L. Novel Approach for the Synthesis of Nanocrystalline Anatase Titania and Their Photovoltaic Application. (2011); 539382, 5.
11. Shayegan Z., Lee C. & Haghighat F. TiO_2 photocatalyst for removal of volatile organic compounds in gas phase –A review Chemical Engineering Journal. (2018); 334: 2408–2439.

12. Zheng R., Meng X. & Tang F. A general protocol to coat titania shell on carbon-based composite cores using carbon as coupling agent. Journal of Solid-State Chemistry. (2009); 182: 1235–1240.
13. Karkare M.M. Choice of precursor not affecting the size of anatase TiO_2 nanoparticles but affecting morphology under broader view. Int Nano Lett. (2014); 4:111.
14. Sato S. Photocatalytic activity of NOx-doped TiO_2 in the visible light region. Chem Phys Lett. (1986); 123:126-128.
15. Asahi R., Morikawa T., Ohwaki T., Aoki K. & Taga Y. Visible-light photocatalysis in nitrogen-doped titanium dioxide. Science (2001); 293: 269-271.
16. Tseng T.K., Lin Y.S., Chen J.Y. & Chu H. A review of photocatalysts prepared by sol-gel method for VOCs removal, Int. J. Mol. Sci. (2010); 11 (6): 2336.
17. Li D., Haneda H., Hishita S. & Ohashi N. Visible-light-driven nitrogen-doped TiO_2 photocatalysts: effect of nitrogen precursors on their photocatalysis for decomposition of gas-phase organic pollutants, Mater. Sci. Eng. (2005); 117 (1): 67–75.
18. Lei X.F., Xue X.X., Yang H., Chen C., Li X., Niu M.C., Gao X.Y. & Yang Y.T. Effect of calcination temperature on the structure and visible-light photocatalytic activities of (N, S and C) co-doped TiO_2 nano-materials, Appl. Surf. Sci. (2015); 332: 172–180.
19. Velasco L. F., Haro M., Parmentier J., Gadiou R., Vix-Guterl C. & Ania C.O. Tuning the Photocatalytic Activity and Optical Properties of Mesoporous TiO_2 Spheres by a Carbon Scaffold. Journal of Catalysts. (2013); 178512.
20. Kumar K.A., Manonmani J. & Senthilselvan J. Effect on interfacial charge transfer resistance by hybrid co-sensitization in DSSC applications. J Mater Sci: Mater Electron (2014): 25:5296–5301.
21. Klongdeea J., Petchkroh W., Phuempoonsathaporn K., Piyasan Praserthdam P., Vangnai A.S. & Pavarajarn V. Activity of nanosized titania synthesized from thermal decomposition of titanium (IV) n-butoxide for the photocatalytic degradation of diuron. Science and Technology of Advanced Materials. (2005); 6: 290–295.
22. Kwon S., Fan M, Cooper A.T. & Yang H. Photocatalytic Applications of Micro- and Nano-TiO_2 in Environmental Engineering. Critical Reviews in Environmental Science and Technology. (2008); 38:197–226.

23. Fan D., Weirong Z. & Zhongbiao W. Characterization and photocatalytic activities of C, N and S co-doped TiO_2 with 1D nanostructure prepared by the nano-confinement effect, Nanotechnology 19 (36) (2008) 365607.
24. Tayade R.J., Natarajan S.T. & Bajaj H.C. Photocatalytic Degradation of Methylene Blue Dye Using Ultraviolet Light Emitting Diodes. Ind. Eng. Chem. Res. (2009); 48, 10262–10267.
25. Dinh C.T., Nguyen T.D., Kleitz F., & Do T.O. Shape-Controlled Synthesis of Highly Crystalline Titania Nanocrystals. American Chemical Society. (2009); 3 (11): 3737–3743.
26. Hlekelele L. Synthesis and characterization of TiO_2 and TiO_2 based quaternary mixed metal oxides supported on carbon and fly ash based materials. Thesis (University of the Witwatersrand, 2016)
27. Pernas-Garzon M., Gormez-Aviles A., Bedia J., Rodriguez J.J. & Belver C. Effect of activating agent on the properties of TiO_2/activated carbon heterostructures for solar photocatalytic degradation of acetaminophen. (2019); 12, 378.
28. Muthuvel I., & Swaminathan M. Solar Energy Materials and Solar Cells. (2008); 92: 857-863.
29. Hoffmann M.R., Martin S.T., Choi W. & Bahnemann D.W. Chem. Rev. (1995); 95: 69-96.
30. Rasheed T., Bilal M., Iqbal H.M.N., Hu H. & Zhang X. Reaction Mechanism and Degradation Pathway of Rhodamine 6G by Photocatalytic Treatment. Water Air and Soil Pollution. (2017); 228; 291-101.
31. Rasheed T., Bilal M., Iqbal H.M.N., Shah S.Z.H., Hu H., Zhang X. & Zhou Y. TiO_2/UV-assisted rhodamine B degradation: putative pathway and identification of intermediates by UPLC/MS. Environmental technology. (2018); 12: 1533–1543.
32. Di Valentin C., Pacchioni G. & Selloni A. Theory of Carbon Doping of Titanium Dioxide. Chem. Mater. (2005); 17, 6656-6665.
33. Ceragioli1 H.J., Peterlevitz A.C., Quispe J.C.R., Larena A., Pasquetto M.P., Sampaio M.A. & Baranauskas V. Synthesis and characterization of boron-doped carbon nanotubes. Journal of Physics: (2008); 052029.

CHAPTER 6: CONCLUSIONS AND RECOMMENDATIONS.

6.1 Conclusions

The purpose of this study was to demonstrate that natural carbon precursors can be used as heteroatoms carbon precursors. The interest in working with onion material stemmed from reports that onion is a green and renewable material consisting of N, H, S, C, and O elements. The motivation was, therefore, to use onion material to produce N, S co-doped carbon spheres for support of TiO_2 catalyst. The synthesized catalyst was utilized for the photodegradation of organic pollutants (e.g. RhB). The study resulted in the following conclusions:

The NSCS material was synthesized by the hydrothermal method followed by the CVD method where activating agents were added. The activating agents that were used were KOH and $ZnCl_2$, this was done to enhance the shape of spheres. The morphology of the NSCS material was characterized by TEM and SEM techniques. In chapter 4, investigations on the effects of activating agent, functionalization, and annealing temperatures on the synthesis of NSCS were discussed. The produced NSCS material was fully studied utilizing various techniques such as TEM, SEM, PXRD, TGA, XPS, FTIR, laser Raman spectroscopy, and BET. The CHNS elemental analysis confirmed the presence of N, S, C, and H elements in the onion raw material. In this work, the onion raw material with optimized conditions produced NSCS with improved structural properties.

The NSCS material was used as a support for TiO_2 semiconductor. The TiO_2_NSCS catalyst and bare TiO_2 were both successfully synthesized by the sol-gel method. The crystallite size calculated by the Scherer equation was observed; 12, 8.2, and 9.9 nm for TiO_2, TiO_2_NSCS2 @850, and TiO_2_NSCS3 @900 ℃, respectively. It was observed that the TiO_2_NSCS3 @900 ℃ catalyst with a high mass ratio of $ZnCl_2$ and subjected to high synthesis temperature proved to have improved photocatalytic activity. The use of heteroatoms such as nitrogen and sulfur as dopants for carbon spheres was to investigate how their different properties can enhance CSs structural properties, and how their properties will influence the performance towards dye degradation when used as support for TiO_2. The photocatalytic activity was measured, with optimized reaction parameters. The optimized parameters were 10 mg of the catalyst in 10 ppm of dye at a pH of 7 and a reaction time of 150 minutes. The HPLC-MS hyphenated technique gave interesting information about the

catalysts. At T0, that is before light exposure to the suspension RhB molecule was dominant (peak at 443 m/z). After the suspension was exposed to solar simulated light, the presence of N-demethylated intermediates was observed at different lower mass-to-charge ratios. This implied that the RhB compound was broken down into smaller fragments and possible non-toxic products (CO_2, H_2O, and inorganic salts). Higher mineralization was reported for TiO_2_NSCS3 @900 ℃ catalyst compared to the TiO_2 catalyst.

6.2 Recommendations

In this study, it was shown that natural-based carbon precursors can be synthesized to produce nitrogen, sulfur co-doped carbon spheres (NSCS) under optimized conditions. However, it was seen that in the synthesis of NSCS some operational parameters such as the synthesis temperature, flow rate of gases, the procedural setup has to be further modified. Also, the mass ratio of the activating agent can be increased, in order to understand the effect it will have on the synthesized spheres.

It can be said that a transparent material is imperative when modifying TiO_2, thus, further investigation on NSCS as a support material will need to be improved. Studies of NSCS_TiO_2 have to be further investigated, giving more attention to the molecular and atomic levels of the catalysts. This will help with understanding the surface interaction and the mechanism that occurs when the RhB pollutant is mixed with the catalysts in one suspension. To understand the interfacial electronic structures and electronic transfer between the NSCS material and TiO_2, computational studies using density functional theory (DFT) can be done. In addition, kinetic studies for TiO_2 and NSCS_TiO_2 catalysts can be conducted to further understand the enhanced degradation efficiency reported in the literature. The recoverability studies can be conducted to understand the stability of the catalysts. The stability of the catalyst will be determined by the consecutive number of cycles achieved by a catalyst.